Title
Improved Acquisition Methods for Hyperpolarized Carbon-13 Magnetic Resonance Imaging

Permalink
https://escholarship.org/uc/item/9082w9sz

Author
Tang, Shuyu

Publication Date
2019

Peer reviewed|Thesis/dissertation

Improved Acquisition Methods for Hyperpolarized Carbon-13 Magnetic Resonance
Imaging

by
Shuyu Tang

DISSERTATION
Submitted in partial satisfaction of the requirements for degree of
DOCTOR OF PHILOSOPHY

in

Bioengineering

in the

GRADUATE DIVISION

of the

UNIVERSITY OF CALIFORNIA, SAN FRANCISCO
AND
UNIVERSITY OF CALIFORNIA, BERKELEY

Approved:

_____   Peder Larson
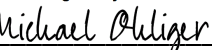   Chair

_____   Daniel Vigneron

Michael Ohliger
_____   Michael Ohliger

_____

_____
                                                              Committee Members

Dedicated to my parents

Qi Wang and Lida Tang

Acknowledgments

First and foremost, I would like to anknowledge Peder Larson, my advisor for my Master's and Ph.D. degrees. I started to learn MRI by taking his class and began to conduct MRI research in his lab after my Master's degree. Thanks to him for offering that valuable research opportunity. He is a fantastic mentor, being visionary about research direction and supportive of students' work. Some projects whose significance I didn't appreciate at the beginning, are actually what other people are trying to catch up with nowadays. He encourages students to pursue their own ideas and also provides abundant resources and insightful advice to make sure projects are meaningful and achieveable. I am supremely grateful for his guidance and support over the past six years.

Daniel Vigneron, John Kurhanewicz and Sarah Nelson have been leaders of hyperpolarized ^{13}C studies in UCSF. I would like to thank them for creating such a collaborative research environment and giving us opportunities to work on interesting and meaningful projects. Daniel Vigneron also has been my other advisor. I am grateful for his introduction to the hyperpolarized ^{13}C field and all his support to my research projects. His sense of humor creates a relaxed and pleasant working place.

Galen Reed, Bill Williams and Juan Santos taught me about how to use RTHawk, the software I've been using in all my dissertation projects. There were more than a hundred of emails between me and them, and most frequent phrases appearing in these emails are 'question' and 'error'. Michael Ohliger and Jane Wang were two clinical physicians that I have worked closely with. They taught me a lot of medical knowledge and the significance of medical imaging in patient management. I also acknowledge Michael's insightful comments on my dissertation. Murat Arcak was gracious to be on my qualifying committee and I am grateful for his valuable advice on my research projects.

Jeremy Gordon, Peng Cao, Wenwen Jiang, Xucheng Zhu and Andrew Leynes have been my labmates for a long time. I enjoyed the time we discussed science and experiments during group meetings, and talked about life and future over the lunch. Jeremy taught me a lot about hyperpolarized ^{13}C MRI and have been a main coordinator of clinical studies shown in this dissertation. I also appreciate his great help on paper revision. Peng's work ethic and enthusiam about research are always inspiring me. He also taught me about spectroscopic

imaging and reconstruction. Wenwen was my first officemate and provided valuable advice on my first projects. She was a gourmet and has recommended many fantastic restaurants. Xucheng was another hard working guy in the lab and a master of image reconstruction. His laugh was contagious and his advice on body building was helpful. Andrew's machine learning skills were stunning and he inspired many coworkers in the lab to apply machine learning in medical imaging.

Thank you everyone!

Abstract

Improved Acquisition Methods for Hyperpolarized ^{13}C Magnetic Resonance Imaging

Shuyu Tang

Magnetic resonance imaging with hyperpolarized ^{13}C-labeled compounds via dynamic nuclear polarization (DNP) has been used to non-invasively study metabolic processes in vivo. This method provides a transient signal enhancement of more than 10,000 fold compared to imaging ^{13}C compounds at thermal equilibrium. However, as soon as the pre-polarized ^{13}C-labeled compound leaves the polarizer, its hyperpolarized state would irreversibly decay to the thermal equilibrium with a decay constant characterized by T1, which is typically less than one minute. The rapid loss of nonrenewable polarization brings challenges in hyperpolarized ^{13}C magnetic resonance imaging. This dissertation presents improved acquisition methods for hyperpolarized ^{13}C imaging with the injection of hyperpolarized [1-^{13}C]pyruvate, which is the most widely studied substrate to date. The improved acquisition methods include a regional bolus tracking sequence for automatic acquisition timing, real-time calibration of frequency and RF power for robust acquisitions, metabolite specific balanced steady state free precession (bSSFP) sequence and metabolite specific fast spin echo sequence for efficient use of polarization in hyperpolarized [1-^{13}C] imaging. The proposed acquisition methods have been demonstrated in various clinical applications on a MR 3T scanner. Bolus tracking and real-time acquisition methods have been used in imaging human brain, heart, kidney and prostate. Metabolite specific bSSFP sequence has been applied in imaging human kidney. Metabolite specific fast spin echo sequence has been demonstrated in imaging human brain.

Contents

Metabolite Specific Multi Spin-Echo Sequences for Hyperpolarized ^{13}C MRI 71

Bibliography **85**

List of Figures

List of Tables

Chapter 1

Introduction

Magnetic resonance imaging (MRI) is a non-invasive and non-radioactive medical imaging modality which can provide a wide range of information, including anatomy, bulk movement, perfusion, diffusion, and metabolism. Currently, most clinical MRI studies acquire signals of hydrogen (^1H), the most abundant atom in the body. Other atoms such as ^{13}C, ^{19}F, ^{23}Na, and ^{31}P can also be imaged. ^{13}C is the only stable isotope of carbon that is detectable by MRI. Since carbon is present in all organic molecules, ^{13}C MRI is capable of detecting a wide range of chemicals in living organisms. However, the low natural abundance of ^{13}C limits the sensitivity of ^{13}C MRI. A process called hyperpolarization[2] was used to enhance the MR signals of ^{13}C-labeled compound in a designated machine termed polarizer. Hyperpolarized ^{13}C MRI refers to imaging the hyperpolarized ^{13}C-labeled compound being injected into the body and its downstream metabolites. Once leaving a polarizer, hyperpolarized ^{13}C-labeled compounds lose their nonrenewable signals rapidly and this poses new challenges in MRI acquisition.

The most widely studied compound to date in hyperpolarized ^{13}C studies is [1-^{13}C]pyruvate due to its favorable polarization properties and its crucial role in a number of significant metabolic pathways. Monitoring metabolic changes using [1-^{13}C]pyruvate has been explored in a number of pathologies, including cancer [8, 38], heart failure [48], inflammatory arthritis[30], traumatic brain injury[18] and diabetes[27]. This dissertation focuses on improving acquisition methods for hyperpolarized ^{13}C imaging with the injection of hyperpolarized [1-^{13}C]pyruvate on a clinical MR 3T scanner.

Chapter 2 introduces the principles of magnetic resonance imaging and outlines the principles, challenges and applications of hyperpolarized ^{13}C magnetic resonance imaging.

Chapter 3 describes a regional bolus tracking and real-time frequency/power calibration methods for hyperpolarized [1-^{13}C]pyruvate imaging. This scheme allows for automatic acquisition timing based on bolus information of a specific region of interest(ROI). Real-time frequency/power calibration improves the calibration accuracy in hyperpolarized [1-^{13}C]pyruvate imaging compared to conventional phantom calibration. Accurate power ensures accurate flip angle, which is crucial for the use of nonrenewable hyperpolarized signal. This method was demonstrated in clinical hyperpolarized [1-^{13}C]pyruvate studies of brain, heart, kidney and prostate.

Chapter 4 and 5 describes multi spin-echo sequences for efficient use of the hyperpolarized signal by repetitively refocusing transverse spins. Chapter 4 presents a metabolite specific 3D stack-of-spiral balanced steady state free precession (bSSFP) sequence. This sequence showed a 2.5-fold signal-to-noise ratio (SNR) improvement on lactate imaging compared to gradient echo sequences as well as improved the spatial coverage compared to Cartesian bSSFP sequence. As with any bSSFP sequence, this sequence was sensitive to B0 inhomogeneity. However, there are some clinical applications such as brain and kidney where B0 is relatively homogenous and it's appropriate to use this sequence. Clinical translation of this sequence was demonstrated on human kidneys.

Chapter 5 presents two metabolite specific fast spin-echo (FSE) sequences. The first sequence used B1-insensitive adiabatic refocusing pulses. This sequence showed a near 2-fold SNR improvement over gradient echo sequences but specific absorption rate (SAR) limits the number of adiabatic pulse used for clinical studies. The second sequence used varied crusher gradients to eliminate stimulated echo pathways and preserve nonrecoverable hyperpolarized magnetization. Compared to constant crusher gradients, varied crusher gradients reduced the signal loss of the longitudinal magnetization. Shinnar-Le Roux (SLR) pulses were used in this sequence for spin refocusing and thus the refocusing performance was sensitive to RF power amplitude. Appropriate application of this sequence was to image regions with homogenous B1, for example, human brain with a birdcage transmit coil, as shown in this chapter.

Chapter 2

Background

This chapter provides the background information of magnetic resonance imaging and hyperpolarized ^{13}C magnetic resonance imaging.

2.1 Fundamentals of Magnetic Resonance Imaging

Magnetic resonance imaging is a nonradiative imaging modality that allows non-invasively acquiring anatomical and physiological information of a subject. This section introduces the basic principles of magnetic resonance imaging from a perspective of classical physics, although some quantum physics descriptions are included when necessary. More detailed description of magnetic resonance imaging can be found in many popular textbooks[39, 3].

2.1.1 Magnetization

Spin angular momentum is an intrinsic property of particles, such as nuclei and electrons. These particles are also referred to as *spins*. Spin angular momentum gives rise to magnetic dipole moment which can be imagined as a vector quantity created by a spinning charged sphere. Magnetic dipole moment is non-zero for nuclei with odd number of protons or/and neutron, such as ^1H and ^{13}C. In the presence of an external magnetic field, spins orient their magnetic dipole moment parallel (n_+)or anti-parallel(n_-) to the magnetic field - this process is called *polarization*. The n_+ population is of lower energy and the tendency to occupy a
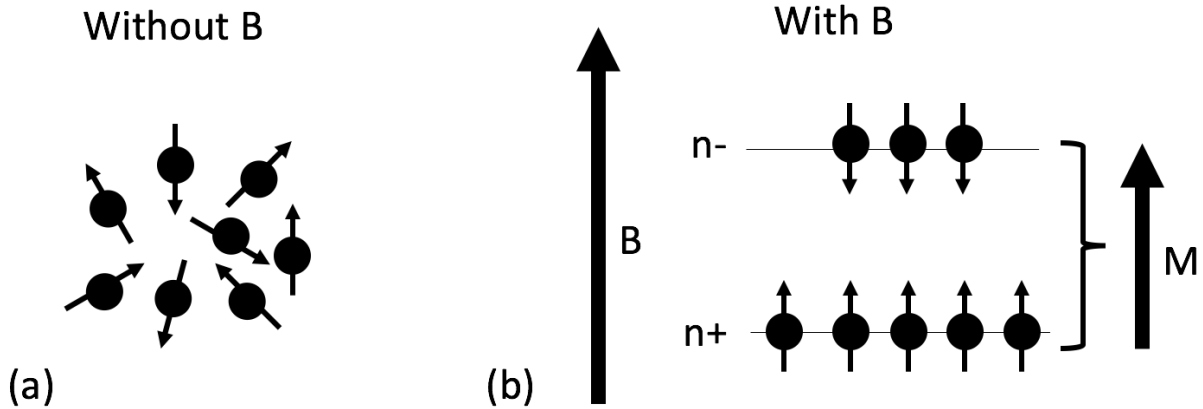
Figure 2.1: Effect of the external magnetic field on spins. The arrows represent the orientation of magnetic dipole moment of each particle. (a) With no external field, spins are randomly oriented. (b) Applying the external field B causes spins to align themselves in parallel (n_+) or anti-parallel(n_-) states. The (n_+) population has a lower energy. The energy difference between two population gives rise to a net magnetization, M.

lower energy state results in a population difference, leading to a net magnetization which we will refer to as the *magnetization M* (Fig. 2.1). The magnetization would reach an equilibrium state proportional to gyromagnetic ratio and the external magnetic field while inversely proportional to the temperature.

2.1.2   Relaxation

When the equilibrium polarization is disturbed, the magnetization returns to it's equilibrium state through a process called *relaxation*, which consists of transverse and longitudinal components(Fig. 2.2).

The longitudinal relaxation, also known as the spin-lattice or T_1 relaxation, describes the restoration of the magnetization parallel to the external field. This process is characterized by the time constant T_1, which depends on the rate of energy exchange between the spin and its surrounding environment such as tissue structure and external field strength. At the higher external field strength, more energy is required to restore the equilibrium magnetization. Hence T_1 values typically lengthen with increasing external magnetic field.
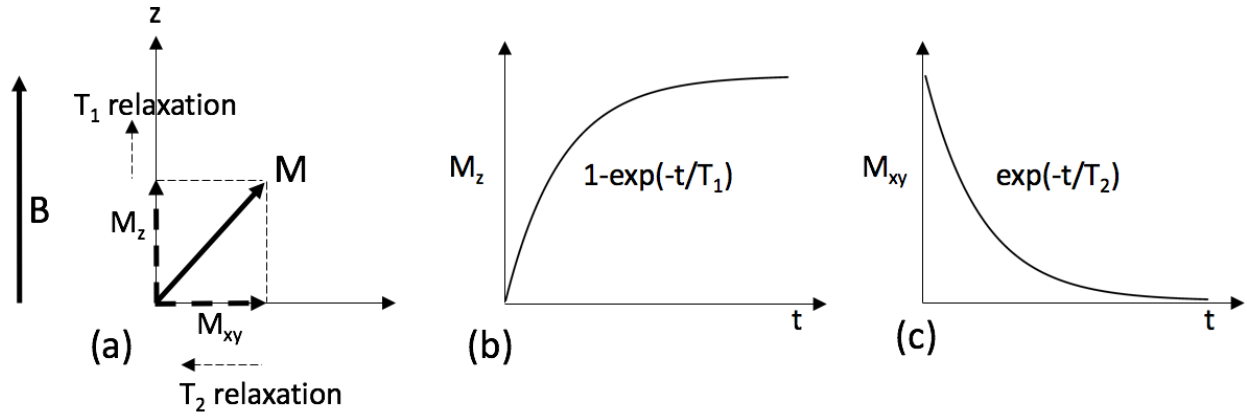
Figure 2.2: The magnetization undergoes relaxation. (b) The longitudinal magnetization returns to the equilibrium by T_1 relaxation. (c) Transverse magnetization decays by T_2 relaxation.

The transverse relaxation, also known as the spin-spin or T_2 relaxation, describes the decay of the magnetization in the plane perpendicular to the external field. This process is characterized by the time constant T_2, which is dominated by the interaction between the magnetic dipole moments of neighboring spins. This interaction, known as dipolar coupling, results in the loss of phase coherence of the transverse magnetization and manifests as transverse decay. If spins are mobile, as in the liquid, they are free to move and will experience a range of local magnetic fields created by magnetic dipole moments of surrounding spins. This averages the effects of dipolar coupling. Hence T_2 values typically increase with increasing mobility of spins. Factors determining T_1 also affect T_2 relaxation, therefore, T_2 is always smaller than T_1.

The effects of T_1 and T_2 relaxation on the magnetization are quantitatively described in the next section.

2.1.3 Bloch Equation

The interaction between magnetization $\mathbf{M}$ and the magnetic field $\mathbf{B}$ is governed by the Bloch equation:

$$\frac{d\mathbf{M}}{dt} = \mathbf{M} \times \gamma \mathbf{B} - \frac{M_x \mathbf{i} + M_y \mathbf{j}}{T_2} - \frac{(M_z - M_0)\mathbf{k}}{T_1} \tag{2.1}$$

5

where $\mathbf{M} = [M_x, M_y, M_z]^T$ is the magnetization vector, $\mathbf{B}$ is the magnetic field vector, t is time, γ is the gyromagnetic ratio which depends on nucleus, M_0 is the equilibrium magnetization, $\mathbf{i}$, $\mathbf{j}$ and $\mathbf{k}$ are unit vectors in x,y,z directions respectively, T_1 and T_2 are longitudinal and transverse relaxation time constant respectively. The cross-product term describes the rotation of the magnetization vector about the magnetic field vector. This rotation process is called *precession* and the rotation frequency is known as the Larmor frequency or resonant frequency.

As discussed in the previous sections, T_1, T_2 and M_0 depend on the external magnetic field $\mathbf{B}$. In magnetic resonance imaging, $\mathbf{B}$ consists of three types of magnetic fields: 1) $\mathbf{B}_0$, the main static field; 2) $\mathbf{B}_1$, radiofrequency fields which are used for excitation (section 2.1.4); 3) $\mathbf{G}$, gradient fields which are essential for spatial encoding (section 2.1.5). Since the amplitudes of $\mathbf{B}_1$ and $\mathbf{G}$ are approximately 1000 times less than that of $\mathbf{B}_0$, only the effect of $\mathbf{B}_0$ on T_1, T_2 and M_0 is considered in the Bloch equation. As $\mathbf{B}_0$ is constant on a MRI scanner, T_1, T_2 and M_0 are treated as constants. The direction of M_0 and T_1 relaxation is parallel to $\mathbf{B}_0$ while that of T_2 relaxation is perpendicular to $\mathbf{B}_0$.

If only the static magnetic field $\mathbf{B}_0$ is present, the longitudinal magnetization M_z is:

$$M_z(t) = M_0 + (M_z(0) - M_0)e^{-\frac{t}{T_1}} \tag{2.2}$$

And the transverse magnetization M_{xy} is:

$$M_{xy}(t) = M_{xy}(0)e^{-\frac{t}{T_2}} \tag{2.3}$$

2.1.4 RF Excitation and Signal Detection

The equilibrium magnetization M_0 aligns with the static magnetic field $\mathbf{B}_0$. To detect the magnetization, another magnetic field $\mathbf{B}_1$ is applied to the transverse plane to tip the magnetization vector away from the $\mathbf{B}_0$ direction. This process is known as *excitation* (Fig. 2.3). The $\mathbf{B}_1$ field is generated by a radiofrequency (RF) coil and applied at the Larmor frequency of the detected spins. The shape and duration of the RF pulse determines its bandwidth. Spins with resonant frequency falling within this bandwidth will be excited.

In the rotating frame of reference at the Larmor frequency, $\mathbf{B}_1$ is static and the magnetization is rotating about the $\mathbf{B}_1$ vector. In the laboratory frame of reference, the magnetization
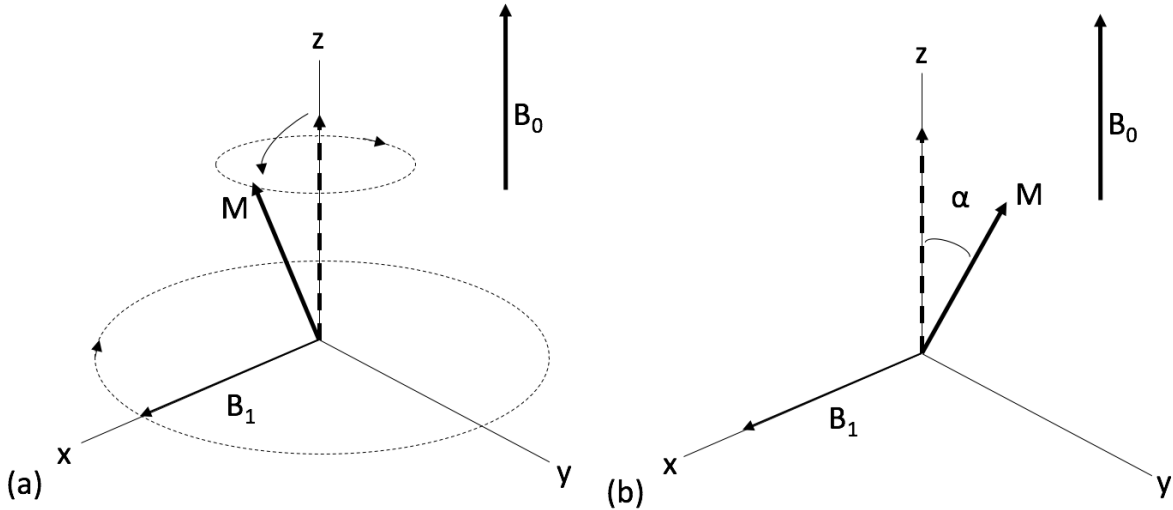
Figure 2.3: Illustration of RF excitation in the laboratory frame (a) and rotating frame (b). $\mathbf{B}_1$ field is applied at the Larmor frequency of the spins. In the rotating frame, $\mathbf{B}_1$ field vector remains stationary, the magnetization vector M is rotating about the $\mathbf{B}_1$. The angle (α) between the magnetization vector before (dashed arrow) and after (solid arrow) experiencing $\mathbf{B}_1$ field is called flip angle. In the laboratory frame, both the $\mathbf{B}_1$ vector and magnetization vector are rotating with the Larmor frequency, and their relative movement are the same as in the rotating frame.

vector is rotating about the $\mathbf{B}_0$ vector and gradually approaching the transverse plane. The angle between the magnetization vectors before and after applying $\mathbf{B}_1$ field is called *flip angle* and is determined by the integral of the $\mathbf{B}_1$ field.

$$\alpha = \int_0^T \gamma B_1(t) dt \qquad (2.4)$$

where T is the duration of the RF pulse.

After excitation, the transverse component of the magnetization vector rotating about $\mathbf{B}_0$ causes a change in magnetic flux and induces an electromotive force (EMF) in an RF receiver coil oriented to the transverse plane. The received signal is called free induction decay (FID), which will be processed to reconstruct an MR image. RF coils are used to both transmit RF pulse for excitation and receive RF signals for image formation.

2.1.5 Spatial Encoding

Spatial encoding of the magnetization is achieved with linear magnetic field gradients in the x, y and z directions. Typical spatial encoding includes slice excitation and acquisition encoding.

Slice excitation requires simultaneously applying an RF pulse of a band-limited frequency response and a linear gradient field. The gradient produces a spatially varying resonant frequency along a direction, and the pulse only excites locations whose frequencies fall within the spectral passband of the RF pulse.

Acquisition encoding occurs after RF excitation and it requires simultaneously applying gradient fields and acquiring signals. K-space ($\mathbf{k}(t)$) is proportional to the integral of the applied gradients ($\mathbf{G}(t)$) over time.

$$\mathbf{k}(t) = \frac{\gamma}{2\pi} \int_0^t G(\tau)d\tau \tag{2.5}$$

In the rotating frame at the Larmor frequency, the acquired signal (neglecting relaxation) is

$$s(\mathbf{k}) = \int_{\mathbf{r}} m(\mathbf{r})e^{-i2\pi\mathbf{k}\mathbf{r}} \tag{2.6}$$

where $\mathbf{r}$ is spatial location and m is the transverse magnetization. Taking the Fourier Transform of the acquired signal recovers the magnetization signal in the image space.

Proper image formation depends on the appropriate coverage in k-space. The field of view (FOV) is the inverse of the spacing of sample points in the k-space, while the spatial resolution (δ) is the inverse of the k-space coverage. These relationships are direction dependent.

$$FOV = \frac{1}{\Delta k} \tag{2.7}$$

$$\delta = \frac{1}{n\Delta k} \tag{2.8}$$

where n is the number of samples along the direction.

Routes to cover k-space region are referred to as trajectories, which are achieved by applying appropriate gradients. There are many different trajectories, such as Cartesian, Echo-Planar Imaging (EPI), Radial and Spiral[3]. Selecting a trajectory involves many considerations, such as acquisition speed, robustness to hardware imperfection, signal-to-noise efficiency, motion sensitivity and off-resonance artifacts.

2.1.6   Image contrast

An MRI experiment requires repetitively applying RF and gradient waveforms. This series of waveforms is known as a pulse sequence. Repetition time (TR) is defined as the time duration between neighboring RF excitations. The amount of T_1 relaxation depends on TR, thus TR is indicative of the T_1 image contrast. Echo time (TE) is defined as the duration from the peak of the RF pulse to the time when gradients traverse the center of k-space. The center of k-space dominates the image intensity and the decay of the transverse magnetization at the center of k-space depends on TE, thus TE is indicative of the T_2 image contrast.

2.2   Introduction to Hyperpolarized ^{13}C Magnetic Resonance Imaging

This chapter provides some background information of hyperpolarized ^{13}C MRI, including an introduction to hyperpolarized ^{13}C MRI, dynamic nulcear polarization hyperpolarization method for ^{13}C, challenges in hyperpolarized ^{13}C MRI acquisition as well as the clinical applications of hyperpolarized [1-^{13}C]pyruvate MRI.

2.2.1   Hyperpolarized ^{13}C Magnetic Resonance Imaging

Conventional magnetic resonance imaging is based on the nucleus of the hydrogen atom (^{1}H), which is the most abundant element in the body. ^{13}C MRI is based on ^{13}C, a non-radioactive isotope of carbon. Since most key metabolic intermediates consist of carbon-containing compounds, imaging based on ^{13}C is a potentially important tool for probing metabolism. Due to low gyromagnetic ratio (1/4 of proton) and low natural abundance (<1%) of ^{13}C, hyperpolarization techniques (Fig. 2.4) are used to increase the ^{13}C MR signal. In hyperpolarized ^{13}C MRI, a ^{13}C labeled compound is hyperpolarized in a polarizer and then transferred to the MR scanner for injection. Once a polarized ^{13}C-labeled compound is taken out of the polarizer, the signal of the hyperpolarized ^{13}C-labled compound will decay irreversibly to its thermal equilibrium with a time constant characterized by T_1 (Fig. 2.5). T_1 of ^{13}C-labled compounds used for these experiments are typically on the order of 1-2 minutes.
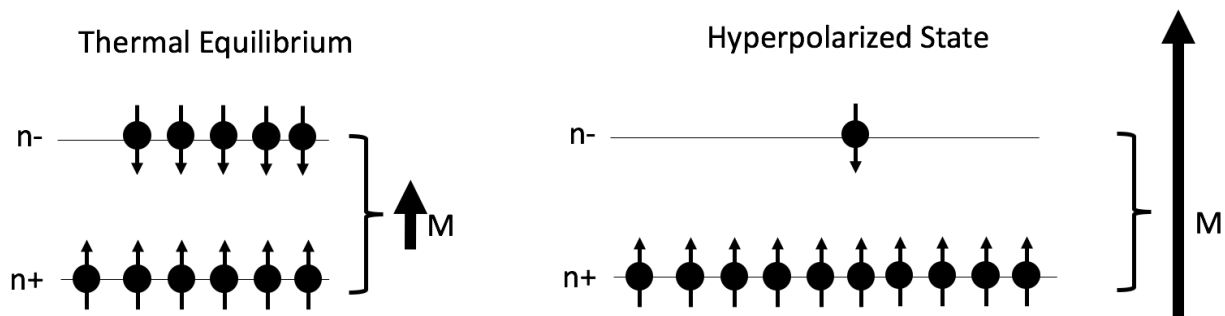
Figure 2.4: Hyperpolarization temporarily enhances magnetization by redistributing spin populations into different energy states. The spin population state(n_+) parallel to the exterinal magnetic field has a lower energy than the one (n_-) anti-parallel to the exterinal magnetic field.

Inside the subject, the injected substrate could participate in in vivo metabolism. [13]C MRI is performed to acquire signals of the injected substrate and its downstream metabolites[21, 22].

2.2.2 Dynamic Nuclear Polarization

As mentioned in section 2.1.1, the magnetization depends on the population difference between spins at different energy states. *Hyperpolarization* is a process to temporarily redistribute the population of energy levels and significantly increase the magnetization (Fig. 2.4).

The most common hyperpolarization technique used for ^{13}C is dynamic nuclear polarization [2] (DNP). DNP is based on the transfer of polarization from the electron spins to nuclear spins. Because the gyromagnetic ratio of an electron is 600 times higher than that of protons, at any magnetic field, unpaired electrons will be more polarized. By placing ^{13}C-labeled compound in close proximity to unpaired electrons and applying microwave irradiation at a proper frequency, the polarization of the unpaired electrons will be transferred to [13]C. The optimal temperature for an efficient polarization transfer is about 1K, where the polarization difference between unpaired electrons and ^{13}C reaches a maximum.
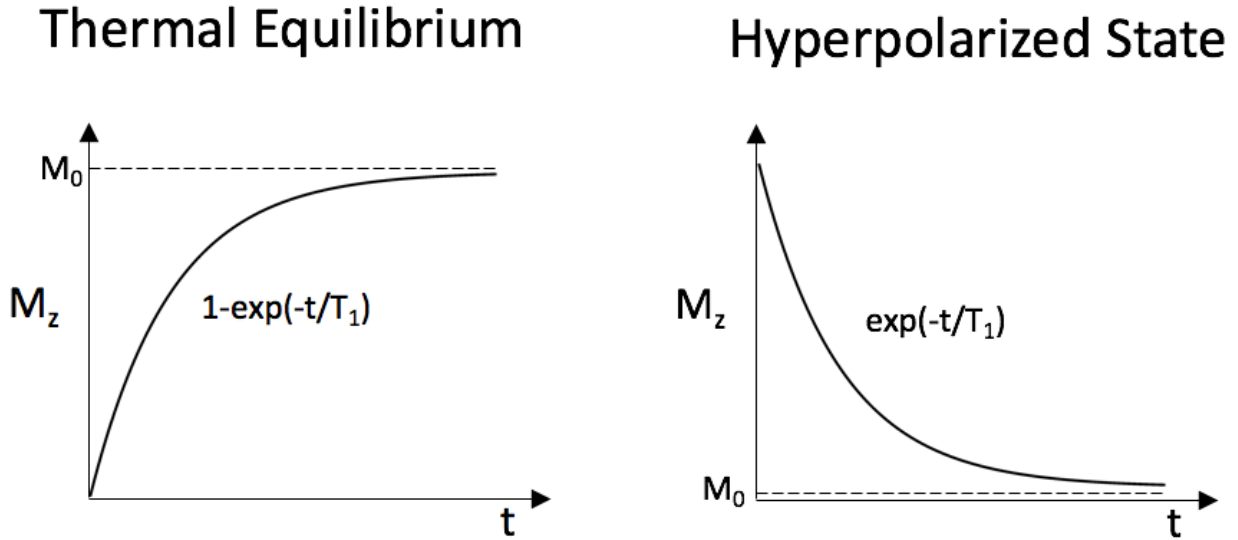
Figure 2.5: Comparison of longitudinal relaxation between thermal equilibrium and hyper-polarized state. At thermal equilibrium, the longitudinal magnetization increases by T1 relaxation to reach the equilibrium. At hyperpolarized state, since its initial longitudinal magnetization is much larger than the equilibrium magnetization, the return of the longitudinal magnetization to the thermal equilibrium is a decay dependent on T1 relaxation.

2.2.3 Challenges in Hyperpolarized ^{13}C MRI Acquisition

Compared with conventional ^{1}H magnetic resonance imaging, many new technical challenges arise in hyperpolarized ^{13}C MRI including ^{13}C probes, polarizer, ^{13}C RF coil and acquisition methods for hyperpolarized ^{13}C MRI. This section focuses on introducing the challenges in the acquisition methods, which is also the focus of this dissertation.

Nonrenewable Polarization

As mentioned in section 2.2.1, the hyperpolarized magnetization is nonrecoverable and decays to thermal equilibrium on the order of 1-2 minutes. Nonrenewable polarization requires efficient use of the polarization. An intuitive solution is to utilize the polarization as soon as possible to minimize the polarization loss due to T_1 decay. This solution is sufficient for acquiring a snapshot of the injected substrate and not imaging its downstream metabolites. However, in hyperpolarized ^{13}C MRI, it is often of interest to monitor dynamic changes of

11

the injected substrate and its downstream metabolites over a period of time (typically $\sim$1 min). Therefore, variable flip angles [61, 37, 64, 31] over metabolites and/or over time points have been proposed to ensure sufficient signal build-up of the downstream metabolites and preserve sufficient polarization at the later time points. Proper calibration of RF power is required to achieve accurate flip angles. In hyperpolarized ^{13}C MRI, lack of endogenous ^{13}C signals make power calibration difficult. One way to address this challenge is to perform real-time power calibration after the injected substrate arrives at the region of interest. However, estimating the arrival time of the injected substrate is challenging for clinical studies due to the inherent physiological difference across subjects. Bolus tracking could be used to monitor the arrival of the injected substrate and trigger the real-time power calibration. This strategy is described in Chapter 3.

Another way to improve the efficient use of the polarization is to utilize the T2 relaxation by repetitively refocusing transverse magnetization. Two common refocusing schemes are fast spin echo (FSE)[63, 58] and balanced steady state free precession (bSSFP)[28, 36, 34, 35, 52]. Fast spin echo uses a train of 180° refocusing pulses with a pair of crusher gradients applied before and after each refocusing pulse. This method is robust to the main magnetic field inhomogeneity but susceptible to spatial power inhomogeneity and likely to saturate nonrenewable polarization on the edge of transmit coil where power is usually largely different from the central region. The bSSFP sequence uses a train of refocusing pulse with zero net gradient area between any two neighboring refocusing pulses. In conventional proton MRI, this method is prone to banding artifacts caused by main magnetic field inhomogeneity. However, since the gyromagnetic ratio of ^{13}C is four times much lower that of ^{1}H, the banding artifacts in ^{13}C bSSFP imaging are less prominent than those in ^{1}H bSSFP imaging. Discussions of applying FSE and bSSFP in hyperpolarized ^{13}C MRI are presented in Chapter 4 and 5.

Fast Dynamic Imaging of Multiple Metabolites

Due to chemical shift phenomenon, which is a small displacement of the resonant frequency due to electron shielding of the main magnetic field, the ^{13}C substrate and its downstream metabolites have different resonance frequencies. If their MR signals are acquired without

applying spatial encoding, the Fourier Transform of these FID signals will produce a frequency spectrum with multiple frequency peaks. During imaging, additional encoding is required to decouple signals along the frequency dimension. Compared with conventional ^1H imaging where a snapshot of anatomical images is usually acquired, hyperpolarized ^{13}C MRI acquires dynamic images of multiple metabolites with fast signal decay. This makes fast imaging techniques indispensable. A spiral trajectory[26] - the fastest trajectory to achieve a given spatial coverage - and its variations are used in most sequences presented in this dissertation. When a moderate matrix size is required or fewer metabolites are acquired, an Echo Planar Imaging (EPI)[7, 15] trajectory or a Cartesian trajectory[23] with proper undersampling strategies could be better options than spiral trajectory due to their better robustness to field inhomogeneity and better tolerance to gradient imperfection.

To decouple multiple metabolites signals along the frequency dimension, frequency information could be encoded using gradients or RF pulse, or a combination of both. Encoding using only gradients[45, 59] is straightforward and is applicable for any frequency spectrum. However, the drawbacks of this approach are long acquisition times and no metabolite specific sequence optimization. Encoding using only RF pulses[7] is the opposite case: requiring complicated RF pulse design and prior knowledge of frequency spectrum, but allowing shorter acquisition time and metabolite specific optimization. The advantages of encoding using RF pulse meet the requirements of hyperpolarized ^{13}C imaging - fast imaging requiring short acquisition time and efficient use of polarization requiring metabolite specific optimization. Therefore, metabolite specific excitation is used in all sequences presented in this dissertation.

2.2.4 Clinical Applications of Hyperpolarized [1-^{13}C]Pyruvate MRI

The most widely studied compound to date in hyperpolarized ^{13}C studies is [1-^{13}C]pyruvate [21, 22, 1] because it is easy to polarize, T_1 is relatively long ($\sim$ 1 min), its safety has been demonstrated in human studies and it plays a crucial role in a number of significant metabolic pathways that convert [1-^{13}C]pyruvate to: [1-^{13}C]lactate via lactate dehydrogenase (LDH), [1-^{13}C]alanine via alanine aminotransferase, and [1-^{13}C]bicarbonate via the pyruvate

dehydrogenase complex. Currently, there are 27 ongoing hyperpolarized $[1\text{-}^{13}C]$ clinical trials registered on clinicaltrials.gov. Most of applications are cancer, in the areas of prostate, brain, breast, ovary and cervix. Other applications include cardiovascular diseases, fatty liver disease and traumatic brain injury.

Chapter 3

A Regional Bolus Tracking and Real-time B0/B1 Calibration Method for Hyperpolarized ^{13}C MRI

3.1 Abstract

Acquisition timing and B_1 calibration are two key factors that affect the quality and accuracy of hyperpolarized ^{13}C MRI. The goal of this project was to develop a new approach using regional bolus tracking to trigger Bloch-Siegert B_1 mapping and perform real-time B_1 calibration based on regional B_1 measurements, followed by dynamic imaging of hyperpolarized ^{13}C metabolites in vivo. The proposed approach was implemented on a system which allows real-time data processing and real-time control on the sequence. Real-time center frequency calibration upon the bolus arrival was also added. The total hyperpolarized signal loss caused by the proposed bolus tracking and real-time frequency/power calibration was calculated based on applied flip angles and expected to be less than 7%. The feasibility of applying the proposed framework for in vivo hyperpolarized [1-^{13}C]pyruvate imaging was tested on a clinical 3T scanner on healthy rats, tumor-bearing mice and human applications including brain, heart, kidney and prostate. Automatic acquisition timing based on either regional bolus peak or bolus arrival was achieved with the proposed framework. Reduced blurring artifacts in real-time reconstructed images were observed with real-time

center frequency calibration. Flip angle correction using B_1 maps results in a more consistent quantification of metabolic activity (i.e, pyruvate-to-lactate conversion, k_{PL}). Experiment recordings are provided to demonstrate the real-time actions during the experiment.

3.2 Introduction

In light of the nonrenewable nature and fast decay of the hyperpolarized magnetization, acquisition timing and transmit power (B_1) calibration are two key factors that affects the quality and accuracy of hyperpolarized ^{13}C imaging.

Bolus tracking for triggering the acquisition has been used in clinical MRI for proton MR angiography [11]. Appropriate acquisition timing for hyperpolarized ^{13}C imaging is useful in several aspects: a) Excitation before the bolus arrival may saturate the nonrecoverable hyperpolarized signal particularly near the coils conductive elements where the B_1 can be elevated. b) Many variable flip schemes [61, 37, 64, 31] that optimize the hyperpolarized MRI signal sampling require knowledge of the bolus arrival. c) It is more straightforward for kinetic modeling to start signal sampling after the bolus maximum [9] to eliminate the need to account for the input function. d) Inconsistent acquisition timing leads to quantification errors when metabolite to substrate ratios are used as a quantitative metric [62, 9]. Currently, in vivo hyperpolarized ^{13}C imaging protocols typically start at a certain fixed delay time after bolus injection. The delay time is determined based on prior knowledge, which can be unreliable due to the inherent physiological variability of each individual. This is particularly problematic in human subjects in which 12 s variations in bolus arrival have been observed in a clinical trial of hyperpolarized ^{13}C prostate study [38]. This variability can be further exacerbated in tumors where the vascularization and perfusion are highly inconsistent over subjects [12]. Recently, a bolus tracking method using a slab FID as tracking signal was demonstrated [9] for automatic acquisition timing. However, this method didn't reflect the signal variation within the imaging slab.

In the context of hyperpolarized ^{13}C MRI, B_1 calibration is crucial for variable flip angle schemes [61, 37, 64, 31] and quantification of metabolic activities [53]. Due to the virtually non-existent endogenous ^{13}C signal, ^{13}C B_1 calibration is typically performed on external phantoms, but this approach does not account for the variability of subject load-

ing. Bloch-Siegert B_1 mapping has been applied to hyperpolarized ^{13}C imaging [25, 50] and is advantageous due to its short acquisition time and efficient use of the hyperpolarization signal. However, real-time power compensation has not yet been accomplished to calibrate the flip angle during the scan.

This chapter presents a new approach using regional bolus tracking to trigger Bloch-Siegert B_1 mapping and real-time RF power compensation based on regional B_1 measurements followed by dynamic imaging of hyperpolarized ^{13}C metabolites. Real-time center frequency calibration upon bolus arrival was also implemented. Thermally polarized ^{13}C phantom experiments were performed to validate Bloch-Siegert B_1 mapping. The feasibility of applying the proposed framework for in vivo hyperpolarized ^{13}C imaging was demonstrated on healthy rats, tumor-bearing mice and human studies including brain, kidney, heart and prostate on a clinical 3T scanner. This proposed method was designed to improve the efficient use of the hyperpolarized signal as well as the accuracy and the robustness of hyperpolarized ^{13}C imaging.

3.3 Methods

3.3.1 Real-time Hyperpolarized ^{13}C MRI

The proposed scheme is illustrated in Fig. 4.1. ROIs for both bolus tracking and B_1 calibration are prescribed according to proton anatomical images before starting ^{13}C sequences. The bolus tracking sequence starts before the hyperpolarized substrate is injected. Real-time center frequency calibration based on the acquired slab frequency spectrum can be triggered upon the bolus arrival. Bloch-Siegert B_1 mapping is either triggered right after frequency calibration or at peak bolus signal. The RF power for all sequences is then calibrated in real time based on the measured ROI B_1. The sequence triggered upon the completion of B_1 calibration in this study is alternating metabolite specific dynamic imaging, which could be replaced by any hyperpolarized ^{13}C sequence for other studies. Our proposed scheme was implemented on a GE Signa MR 3T scanner (GE Healthcare, Waukesha, WI) using commercial software (RTHawk, HeartVista, Los Altos, CA) which allows for real-time reconstruction of acquired data and feedback control of the pulse sequence. The software was installed on a
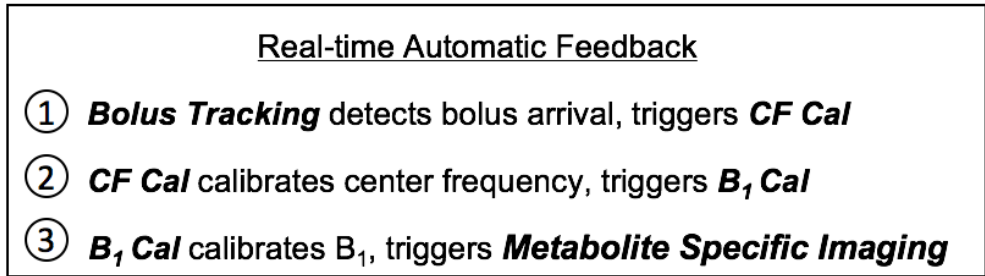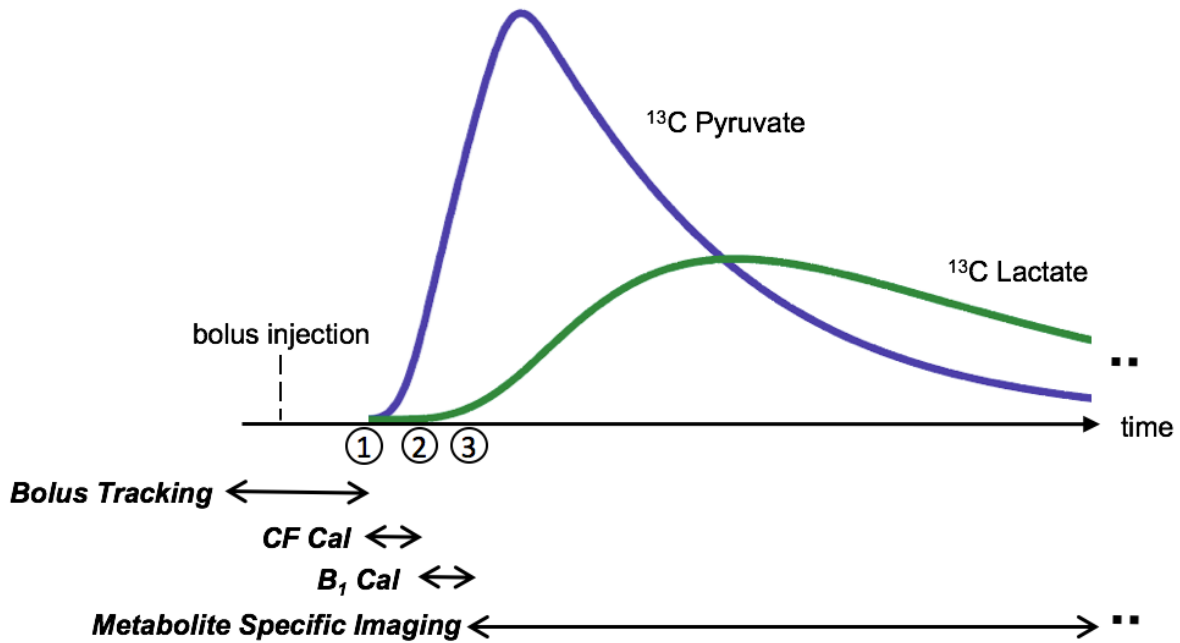
Figure 3.1: Overview of the proposed scheme. Bolus tracking was used to monitor ROI bolus arrival or bolus peak and trigger real-time B0/B1 calibration, followed by metabolite specific imaging. B0 calibration ('CF Cal') is performed based on the frequency spectrum of a prescribed slab. B1 calibration ('B1 Cal') consists of Bloch-Siegert imaging and RF power compensation based on ROI B1. Metabolite specific imaging could be replaced by any hyperpolarized ^{13}C sequence for other studies.

workstation (2.4GHz, 16 proccessors, 64 GB RAM) running the Ubuntu operating system.

The bolus tracking sequence used a singleband spectral-spatial excitation pulse and a single-shot spiral readout, similar to Fig. 3.2 but without the Fermi pulse and associated delay. In these studies, this was used for selective imaging of [1-^{13}C]pyruvate, but could be

adapted for other metabolites (e.g. ^{13}C-urea). The algorithm for tracking the maximum bolus signal was implemented based on prior works [11, 9]. The bolus signal is the mean value of a prescribed ROI placed on the tracking image. Our bolus tracking acquisition consists of two modules, noise calibration and bolus tracking, which can be performed independently. Noise calibration is used to determine the tracking threshold. If the tracking threshold has been previously computed, bolus tracking can be performed without running noise calibration. In the noise calibration module, the tracking threshold S_{thr} is determined as $S_{thr} = c_{thr}\sigma = c_{thr}\frac{m_{noise}}{\sqrt{\frac{\pi}{2}}}$, where σ is the standard deviation of Gaussian noise in the complex image, m_{noise} is the mean value of magnitude images of noise and c_{thr} is a scaling factor. 100 calibration scans (TR = 200 ms) are performed to compute m_{noise} which is converted to σ [17]. Given the noise distribution of the background in magnitude images follows a Rayleigh distribution[17], if a probability P_{thr} that a noise signal is above the tracking threshold is required, the proportional relationship between S_{thr} and σ can be derived using the cumulative distribution function of a Rayleigh distribution. For example, $c_{thr} = 3$ would result in a P_{thr} of 0.001%.

In the bolus tracking module, bolus tracking sequence is used to monitor either ROI bolus arrival or bolus peak. The sequence is resumed automatically if the bolus peak or bolus arrival is not detected. Bolus arrival is determined as ROI signal above the signal threshold. When bolus arrival is detected, a trigger is sent to start other sequences. For bolus peak detection, when a cumulative number n_{cum} of signal increases is detected and all these signals are above the tracking threshold, the program starts to update the peak value. When the bolus signal is lower than u_{peak} fraction of the current peak signal, detection of bolus peak will be reported. In our study, u_{peak} was determined based on estimated hyperpolarization loss due to T_1. For example, under the assumptions of a T_1 of 30s, an excitation flip angle of 5°, no more pyruvate from the bolus coming into the ROI and neglecting metabolic conversion, the hyperpolarization loss over a TR of 1s for the bolus tracking sequence would be 1 - cos(5° × $\pi/180$) = ~0.04, and the remaining hyperpolarization (~0.96) was used as u_{peak}. The use of cumulative increase rather than successive increase as used in the previous work [9] aims to improve the robustness of the tracking algorithm to motion and injection with unstable rates. For some experiments, during the time that bolus signal was below the current signal peak but above u_{peak} threshold, a short repetition time was used to shorten the time interval
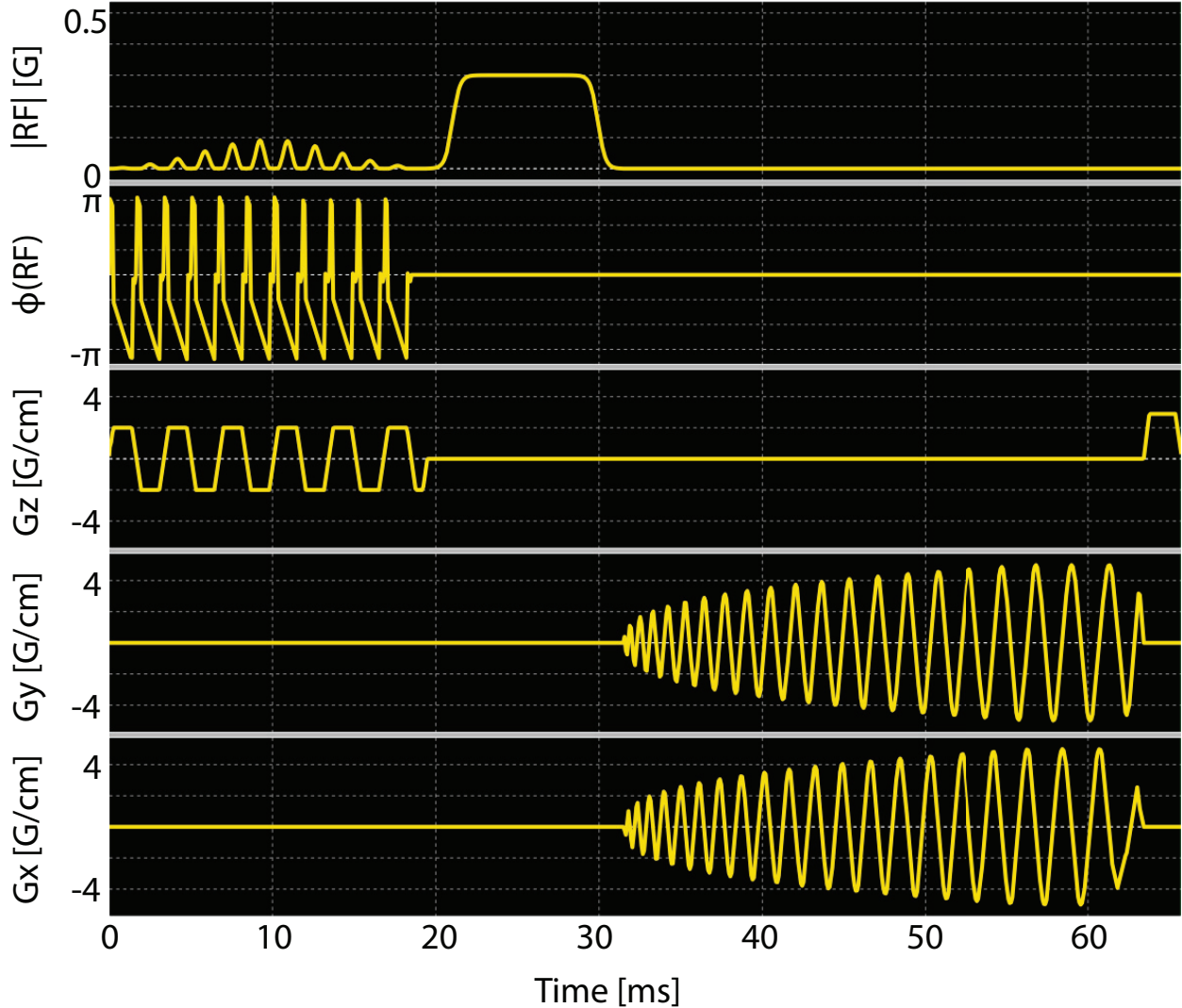
Figure 3.2: Metabolite-specific imaging sequence used in this study, where all instances included a singleband spectral-spatial excitation pulse (passband 120 Hz, stopband 600 Hz) and a single-shot spiral readout. The sequence shown also includes an off-resonance Fermi pulse ($T_{RF} = 12$ ms, $\omega_{RF} = \pm 4.5$ kHz) for Bloch-Siegert B1 mapping, while bolus tracking and metabolite imaging also used this sequence but without Fermi pulse and its associated delay. Other key parameters for bolus tracking were FA 5° (pyruvate), TR 1s; and for Bloch-Siegert B1 mapping were FA 10° (pyruvate), TR 200ms.

between actual bolus peak and detected bolus peak.

The Bloch-Siegert B_1 mapping sequence[47, 25, 50] (Fig. 3.2) shared the similar excitation and readout as bolus tracking, using a singleband spectral-spatial excitation pulse and a single-shot spiral readout, whereas an off-resonance Fermi pulse ($K_{BS} = 6.76 rad/G^2$) was inserted in between. The phase difference between two Bloch-Siegert B_1 mapping sequences with opposite ω_{RF} was used to calculate B_1. Taking the phase difference removes receiver phase and minimizes the influence of B_0 off-resonance frequency [47]. Parameters used in this study were designed to measure a maximum B_1 of 0.48G. The two phase maps were masked based on corresponding magnitude images in order to eliminate noisy phases due to low signal. The threshold was determined as $S_{B_1} = c_{B_1}\sigma$, where c_{B_1} is a scaling factor and noise standard deviation σ was obtained from the bolus tracking sequence. The ratio of the desired B_1 to the measured ROI B_1 was passed to all sequences as a scaling factor to calibrate transmit power in real time.

The center frequency calibration sequence consists of a sinc excitation pulse with slab selection gradient and a 102 ms readout with a 5kHz bandwidth. The acquired spectrum is used to calibrate center frequency for all sequences in real time. Metabolite specific imaging was used to alternately acquire signals of ^{13}C metabolites over time. The metabolite specific imaging sequence shared the same excitation RF pulse and readout as bolus tracking, using a singleband spectral-spatial excitation pulse and a single-shot spiral readout, but with different excitation frequency and different flip angles for imaging different ^{13}C metabolites.

All methods described are available through the HeartVista research collaboration portal (`https://www.heartvista.com/git/shuyu/hv_research_shuyu`).

3.3.2   Phantom and Animal Experiments

Validations of the Bloch-Siegert B_1 mapping sequence were performed on a ^{13}C/^{1}H birdcage coil as well as on a ^{13}C figure-8 transceiver coil. For experiments using the ^{13}C/^{1}H birdcage coil, a cylindrical ethylene glycol phantom with a base of 3.6cm diameter was used. Axial ^{13}C B_1 maps at four transmit powers (50%, 75%, 100% and 150% of the calibrated power) were acquired (FA 90°, slice thickness 10mm, Fermi pulse duration T_{RF} 12ms, frequency offset ω_{RF} $\pm 4.5kHz$, FOV 10cm, in-plane resolution 2.5×2.5mm, TR 2s, NEX 100). For experiments

Table 3.1: ^{13}C sequence parameters for animal experiments.

Sequence	Parameters	Rat/Birdcage	TRAMP	Rat/Surface
Bolus Tracking	Slice thickness (mm)	10	20	10
	Resolution (mm²)	2.5 × 2.5	2.5 × 2.5	2.94 × 2.94
	Shared Parameters	FOV 10cm, FA 5º, TR 1s/0.5s before/after bolus peak, upeak 0.95, c_{thr} 6, n_{cum} 3		
B1 Mapping	Slice thickness (mm)	10	20	10
	Resolution (mm²)	2.5 × 2.5	2.5 × 2.5	2.94 × 2.94
	Shared Parameters	FOV 10cm, FA 10º, TR 200ms, c_{B1} 3, desired B1 0.3G		
Metabolite Specific Dynamic Imaging	FOV (cm)	10	8	10
	Slice thickness (mm)	10	20	10
	Resolution (mm2)	2.5 × 2.5	2.86 × 2.86	2.94 × 2.94
	Shared Parameters	FA 10º for pyruvate, FA 40º for lactate, Temporal resolution 2s		
Frequency Calibration	Slice thickness (mm)	NA	20	10
	Shared Parameters	NA	FA 3º, TR 150ms	

using the ^{13}C figure-8 transceiver coil, a cup (cross-section diameter from 5.5 to 7.5cm, height 7.5cm) filled with oil was placed on top of the coil. An axial ^{13}C magnitude map with a nominal 180° excitation (FA 180°, slice thickness 100mm, FOV 20cm, in-plane resolution 5 × 5mm, TR 1s, NEX 100) and its corresponding B_1 map (FA 60°, slice thickness 100mm, Fermi pulse duration T_{RF} 8ms, frequency offset ω_{RF} $\pm 3kHz$, FOV 20cm, in-plane resolution 5 × 5mm, TR 1s and NEX 200) were acquired. A 2D phase unwrapping algorithm [56] based on minimum spanning tree was implemented to correct phase images of B_1 mapping off line.

Hyperpolarized ^{13}C animal experiments were performed to test our proposed scheme using

normal Sprague-Dawley rats and transgenic adenocarcinoma of mouse prostate (TRAMP) mice with ^{13}C/^{1}H birdcage coils (8cm diameter for rats, 5cm diameter for mice). Two experiments were also performed on a rat with a ^{13}C figure-8 transceiver coil. A total of six rats and two TRAMP mice were used to test the proposed scheme. All animal studies were conducted under protocols approved by the University of California San Francisco Institutional Animal Care and Use Committee (IACUC). Both rats and mice were anesthetized with isoflurane (1-2%) and placed in a supine position on a heated pad throughout the duration of the experiments. [1-^{13}C]pyruvic acid (Sigma Aldrich, St. Louis, MO) mixed with 15mM trityl radical (GE Healthcare, Waukesha, WI) and 1.5mM Gd-DOTA (Guerbet, Roissy, France) was polarized in a HyperSense dissolution DNP system (Oxford Instruments, Abingdon, UK) at 1.35K and 3.35T for $\sim$1h. A 4.5mL volume of 80mM NaOH and 40mM Tris buffer was used as dissolution media, resulting in a 80mM [1-^{13}C]pyruvate solution, with final pH of 6-8. The hyperpolarized [1-^{13}C]pyruvate was injected into the animal via tail vein catheters, $\sim$2.6mL for each rat and $\sim$350μL for the mouse. Each animal received two injections.

All animal experiments were performed using the proposed scheme (Fig. 4.1). ^{13}C sequence parameters for animal experiments are shown in Table 3.1. Some experiments were performed with real-time center frequency calibration. The desired B_1 of the Fermi pulse in B_1 mapping sequence for all experiments was always set to 0.3G (344% of B_1 required for a 90° excitation of the spectral-spatial pulse used in this study). Using the measured transmit B_1 maps, all in vivo results were compensated for spatial B_1 variations and flip angles between sequences. RF power measurements are shown as relative B_1 maps which is the measured B_1 normalized by the desired B_1. For some experiments, data from alternate pyruvate and lactate dynamic imaging was used to quantify pyruvate-to-lactate conversion rate (k_{PL}) based on a two-site exchange model [19] using non-linear least-squares fitting.

For rat experiments using the ^{13}C/^{1}H birdcage coil, an anatomical localizer was acquired using proton 3D bSSFP sequence (FOV 16 $\times$ 8 $\times$ 4.8cm, Matrix size 256 $\times$ 256 $\times$ 76). A total number of five injections were performed on three rats using the proposed scheme with different combinations of injection times (8s, 12s) and transmit gains (100%, 120% of pre-scan power calibration). Real-time center frequency calibration was not performed in these studies. A ^{13}C urea phantom was used for frequency and pre-scan power calibrations. ^{13}C images were acquired on the axial kidney plane. ROIs for bolus tracking and B_1 calibration

were both placed on the left kidney.

For rat experiments using the ^{13}C transceiver coil, an anatomical localizer was acquired using proton T2-weighted fast spin echo sequence (FOV 6 × 6cm, Matrix size 256 × 256) with the scanner body coil. The rat was positioned in a way that right kidney was about 1 cm further than left kidney from the bottom ^{13}C transceiver coil. This set up was designed to produce a distinct B_1 variation between two kidneys. Two injections were performed using the proposed scheme with the same parameters but with different tracking/B_1 calibrating ROIs, one on right kidney and the other on left kidney. A ^{13}C urea phantom embedded on the coil was used for initial pre-scan frequency and power calibration. Real-time center frequency calibration was performed at the bolus arrival. ^{13}C images were acquired on the axial kidney planes with an injection time of 10s and transmit gain set based on pre-scan with the ^{13}C-urea phantom.

For the TRAMP experiment, an anatomical localizer was acquired using proton T2-weighted fast spin echo sequence (FOV 6 × 6cm, Matrix size 256 × 256). Real-time center frequency calibration was performed at the bolus arrival. ^{13}C images were acquired on the axial tumor plane with an injection time of 12s and transmit gain the same as the calibrated power in pre-scan. A ^{13}C urea phantom was used for pre-scan frequency and power calibration. ROIs for bolus tracking and B_1 calibration were both in the tumor.

3.3.3 Human Studies

Human studies were performed to demonstrate the flexibility of the proposed scheme (Fig. 4.1) in various hyperpolarized [1-^{13}C]pyruvate applications. Brain, kidney and heart experiments were performed on healthy volunteers while prostate studies were performed on patients bearing prostate tumors. Subjects were recruited with institutional review board approval and provided with written informed consent for participation in the study. An Investigational New Drug approval was obtained from the U.S. Food and Drug Administration for generating the agent and implementing the clinical protocol. 1.47g of Good Manufacturing Practices (GMP) [1-^{13}C]pyruvate (Sigma Aldrich, St. Louis, MO) mixed with 15mM electron paramagnetic agent (EPA) (AH111501, GE Healthcare, Oslo, Norway) was polarized using a 5T SPINlab polarizer (General Electric, Niskayuna, NY) for 3h before being

Table 3.2: ^{13}C sequence parameters for human studies

Sequence	Parameters	Brain	Heart	Kidney	Prostate
Bolus Tracking	ROI for tracking and B1 calibration	brain tissue near the superior sagittal sinus	right ventricle	right kidney	prostate tumor
	Tracking arrival or peak	Arrival	Arrival	Arrival	Peak
	shared parameters	FA 5°, Slice thickness 30mm, Resolution 1.5 × 1.5 cm^2, FOV 39cm, TR 1s, c_{thr} 3			
B1 Mapping	Nslices	1	1	1	8
	shared parameters	FA 10°, Slice thickness 30mm, Resolution 1.5 × 1.5 cm^2, FOV 39cm, TR 200ms, c_{B1} 2, desired B1 0.3G			
Multi-slice Metabolite Specific Dynamic Imaging	^{13}C metabolite signals acquired	pyruvate/lactate/ bicarbonate	pyruvate/lactate/ bicarbonate	pyruvate/lactate/ bicarbonate/alanine	pyruvate/lactate
	Nslices	8	5	10	16
	shared parameters	FA 20° for pyruvate, FA 30° for other metabolites, Slice thickness 20mm, FOV 39cm, Resolution 1.5 × 1.5 cm^2, Temporal resolution 3s			
Frequency Calibration	shared parameters	FA 3°, Slice thickness 20mm, TR 150ms			

rapidly dissolved with 130°C water and forced through a filter that removed EPA. The solution was then collected in a receiver vessel and neutralized with NaOH and Tris buffer. The receive assembly that accommodates quality-control processes provided rapid measurements of pH, pyruvate and EPA concentrations, polarization, and temperature. In parallel, the hyperpolarized solution was pulled into a syringe (Medrad Inc, Warrendale, PA) through a 0.5μm sterile filter (ZenPure, Manassas, VA) and transported into the scanner for injection. The integrity of this filter was tested in agreement with manufacturer specifications prior to injection. A 0.43mL/kg dose of ∼250mM pyruvate was injected at a rate of 5mL/s via an intra-venous catheter placed in the antecubital vein, followed by a 20mL saline flush.

Brain studies used a birdcage transmit coil and a 32 channel receive coil [33]. Kidney studies used a clamshell transmit coil and a 16 channel receive coil. Prostate studies used the clamshell transmit coil and an endorectal receive coil. Cardiac studies used the clamshell

transmit coil and 8 channel paddle receive coils.

Different from animal experiments, excitation pulses for bolus tracking, B_1 mapping and metabolite-specific dynamic imaging were replaced with a different singleband spectral-spatial RF pulse (130Hz FWHM passband, 870Hz stopband) [16]. B1 mapping and real-time B_1 calibration were triggered right after real-time center frequency calibration. In some studies, more than one B_1 slice were acquired while B_1 calibration was always performed on the central slice. The ROI for both bolus tracking and B_1 calibration was placed on the tissue of interest for different applications accordingly. Following B_1 calibration, multi-slice 2D acquisitions were performed to alternately acquire signals of [1-^{13}C]pyruvate and its downstream [1-^{13}C] metabolite (lactate, bicarbonate and alanine). A ^{13}C urea phantom embedded on the coil was used for pre-scan frequency calibration. Pre-scan power calibration was performed on a ^{13}C ethylene glycol head phantom. Proton anatomical images were acquired with body coil built in the scanner. ^{13}C sequence parameters for all human studies are presented in Table 3.2.

For the online reconstruction, multichannel k-space data were combined using sum of squares. In the offline processing, coil combination was performed by using pyruvate signals as coil sensitivity maps [65].

3.4   Results

3.4.1   Phantom and Animal Results

Axial thermal ^{13}C B_1 maps of the ^{13}C/^{1}H birdcage coil at 50%, 75%, 100% and 150% of the calibrated transmit power are shown in Fig. 4.4a. The mean B_1 value of the phantom region versus the relative transmit power is plotted (Fig. 4.4b) to demonstrate the quadratic relationship between Bloch-Siegert phase difference and transmit power. A comparison between the magnitude image of nominal 180° excitation and its corresponding B_1 map of a thermal ^{13}C phantom on the ^{13}C transceiver coil is shown in Fig. 4.4c and Fig. 4.4d. The B_1 value along the dark band in Fig. 4.4c and its corresponding theoretical excitation flip angle (0.3 G) is plotted in Fig. 4.4e, demonstrating the accuracy of Bloch-Siegert B_1 mapping.

Results of a representative hyperpolarized [1-^{13}C]pyruvate experiment using the proposed

scheme to image the kidneys of a healthy rat with $^{13}C/^1H$ birdcage coil are shown in Fig. 3.4. Real-time center frequency calibration was not performed in this study. Fig. 3.4d displays every other timeframe of the real-time reconstructed data where magnitude images are normalized by the peak value of the corresponding metabolic series. The acquired B_1 map (Fig. 3.4b) was homogenous, as expected for this coil. The initial transmit power was purposely set to 120% of the power calibrated on a thermal ^{13}C phantom and resulted in a nominal B_1 scaling factor of 0.83 (1/1.2), which was in reasonable agreement with the real-time computed B_1 scaling factor of $\sim$0.87. Normalized pyruvate signal curves combining the data of bolus tracking and pyruvate/lactate dynamic imaging are shown in Fig. 3.4c for different ROIs. These pyruvate signal curves demonstrate that the ROI (left kidney) bolus peak was successfully detected, and acquisition timing would be different if the tracking ROI was on the major vessels.

Results of a hyperpolarized [1-^{13}C]pyruvate experiment using the proposed scheme to image the tumor of a TRAMP mouse with $^{13}C/^1H$ birdcage coil is shown in Fig. 4.7. Fig. 4.7e displays every other timeframe of the real-time reconstructed data where magnitude images are normalized by the peak value of the corresponding metabolic series. The frequency spectrum (Fig. 4.7d) acquired from the imaging slab at the bolus arrival shows that the measured pyruvate frequency was 20Hz downfield from the frequency calibrated based on a thermal ^{13}C phantom. Bolus tracking images right before and after real-time center frequency calibration in Fig. 4.7e demonstrate that real-time center frequency calibration reduced blurring caused by off resonance reconstruction in real-time reconstructed images. Fig. 4.7b depicts the normalized B_1 map which is homogenous as expected for the coil. The real-time B_1 scaling factor (Fig. 4.7b) was 1.05, indicating a 5% difference from the power calibrated on a thermal ^{13}C phantom. Tumor k_{PL} (Fig. 4.7c) fitted using pyruvate and lactate signals was ~ 0.09 s^{-1}, agreeing with prior works[4] which showed a k_{PL} range of 0.03 to 0.08 s^{-1} for high grade TRAMP tumor.

Results of two hyperpolarized [1-^{13}C]pyruvate experiments using the proposed scheme to image the kidneys of healthy rats with one-sided ^{13}C surface transceiver coil are shown in Fig. 3.6. Two experiments were performed with the same parameters but with different tracking/calibrating ROIs, one on the right and the other on the left kidney, where the left kidney was closer to the coil. B_1 maps (Fig. 3.6b) acquired in two experiments are consistent

and show that the left kidney experienced a 40% higher B_1 than the right kidney did. This agreed with the real-time B_1 scaling factors, 1.49 and 1.07 for the tracking experiments on the left and right kidney, respectively. k_{PL} maps fitted with and without flip angle correction for the two experiments are shown in Fig. 3.6c, where k_{PL} values of right kidney, left kidney and intestine are labeled. Root mean squared errors of k_{PL} values in the three labeled ROIs between two experiments are 0.0033 with flip angle correction and 0.0045 without flip angle correction, demonstrating that using acquired B_1 maps to correct flip angle results in more consistent k_{PL} estimations.
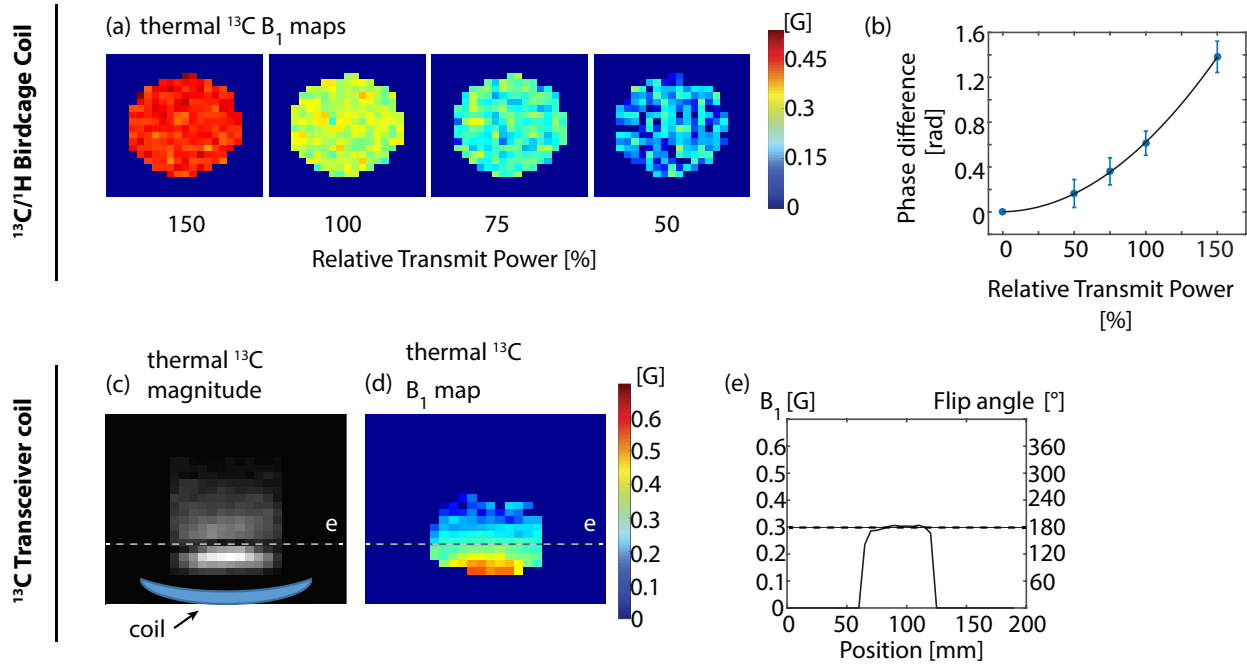
Figure 3.3: Validation of Bloch-Siegert B_1 mapping on the $^{13}C/^1H$ birdcage coil using a cylindrical ethylene glycol phantom (a-b) and on the ^{13}C figure-8 transceiver coil using a cup filled with oil (c-e). For the latter experiment, the oil cup was placed on the top of the ^{13}C coil. In both experiments, the desired B_1 of the Bloch-Siegert pulse was 0.3G, at which the excitation pulse would produce the theoretically accurate flip angle. (a) Axial ^{13}C B_1 maps of birdcage coil with 50%, 75%, 100% and 150% relative to the calibrated transmit power in pre-scan. (b) A plot of Bloch-Siegert phase difference versus relative transmit power. Each data point corresponds to the mean value of the phantom area of each B_1 image in (a). The data point at the relative power of zero is estimated to be zero. The quadratic curve is computed by a least-squares fitting. (c) Axial ^{13}C image of transceiver coil with a nominal 180° flip angle. The dark band in the image corresponds to a 180° signal null. (d) Corresponding axial B_1 map of (c), where the dark band corresponds to $\sim$0.3 G as expected. (e) A plot of B_1 value across the dark band and corresponding flip angles calculated based on the B_1 value.

(a) anatomical

○ vessel
'͡⸴ left kidney
(ROI for tracking and B_1 calibration)

(b) normalized B_1 map

B_1 scaling factor = 1/B_1_ROI = ~0.867

(c) pyruvate signals of bolus tracking (dot) and dynamic imaging (circle) for different ROIs

- tracking/kidney
- tracking/vessel
- tracking/slab
- dynamic/kidney
- dynamic/vessel
- dynamic/slab

signal intensity [a.u.]

time(s)

(d) ^{13}C results displayed by time

bolus tracking

B_1 mapping also see (b)

pyruvate/lactate dynamic imaging

pyruvate

lactate

time

Figure 3.4: Results of a hyperpolarized [1-^{13}C]pyruvate study in a normal rat using the proposed method (Fig. 4.1) with a birdcage coil. Real-time center frequency calibration was not performed in this study. The ROI for both bolus tracking and B_1 calibration was on the left kidney. Injection time was 8 s and initial power was purposely set to 120% of the calibrated power in pre-scan. Sequence parameters are presented in Table 3.1. (a) Proton localizer. (b) Normalized ^{13}C B_1 map. Real-time B_1 scaling factor (~0.87) matched up with the initial transmit power (120%). (c) Normalized pyruvate signal curves in different ROIs. The ROI (left kidney) bolus peak was successfully detected. (d) ^{13}C results displayed in the order of time. Every other timeframe is shown. Experiment recording: https://youtu.be/CN3mIrzmBT8.

(a) anatomical

tumor
(ROI for tracking and B_1 calibration)

(b) normalized B_1 map

B_1 scaling factor
$= 1/B_1\_ROI = {\sim}1.045$
[%]

(c) k_{PL} map with FA correction

ROI k_{PL} ${\sim}0.09$
[s^{-1}]

(d) acquired spectrum

peak frequency
~20Hz

-400 -200 0 200 400
[Hz]

(e) ^{13}C results displayed by time

bolus tracking

cf calibration
also see (d)

bolus tracking

B_1 mapping
also see (b)

pyruvate/lactate
dynamic imaging

pyruvate

lactate

time

cf calibration reduced image blurring caused by off resonance reconstruction
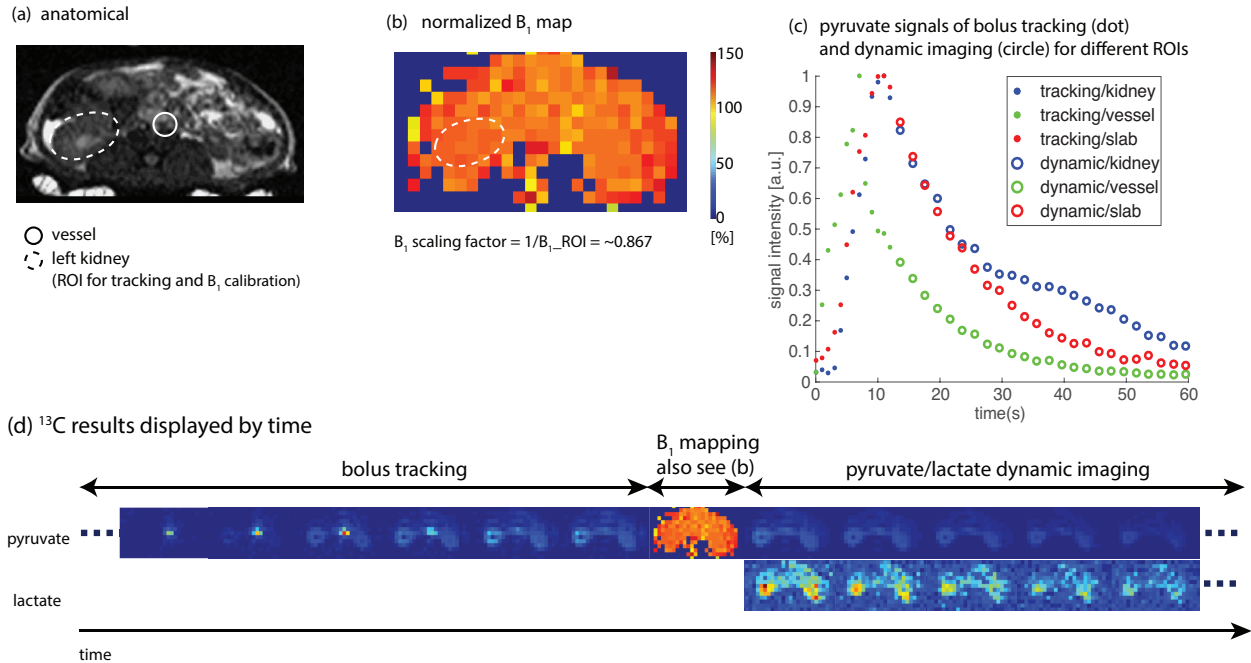
Figure 3.5: Results of a hyperpolarized [1-^{13}C]pyruvate study in a TRAMP mouse using the proposed method (Fig. 4.1) with a birdcage coil. The ROI for both bolus tracking and B_1 calibration was the tumor. Injection time was 12 s and initial power was the same as the calibrated power in pre-scan. Sequence parameters are presented in Table 3.1. (a) Proton localizer. (b) Normalized ^{13}C B_1 map. (c) Pyruvate-to-lactate conversion rate(k_{PL}) map with corrected flip angle. (d) Acquired frequency spectrum for center frequency calibration. "Center frequency" is abbreviated as "cf" in the figure. (e) ^{13}C results displayed in the order of time. Every other timeframe is shown. Bolus tracking images before and after real-time center frequency calibration demonstrate that real-time center frequency calibration reduced off-resonance artifacts in real-time reconstructed images. Experiment recording: https://youtu.be/ViTDb3PzK3U.

(a) anatomical

⋯ right kidney (on the top)

⌐ left kidney (on the bottom)

○ intestine

coil ↗

(b) normalized B_1 map

(c) k_{PL} with FA correction

k_{PL} without FA correction

experiment 1
tracking/calibrate B_1 on right kidney

0.014 0.0094 0.0066

0.0074 0.0049 0.0073

experiment 2
tracking/calibrate B_1 on left kidney

0.012 0.0070 0.0059

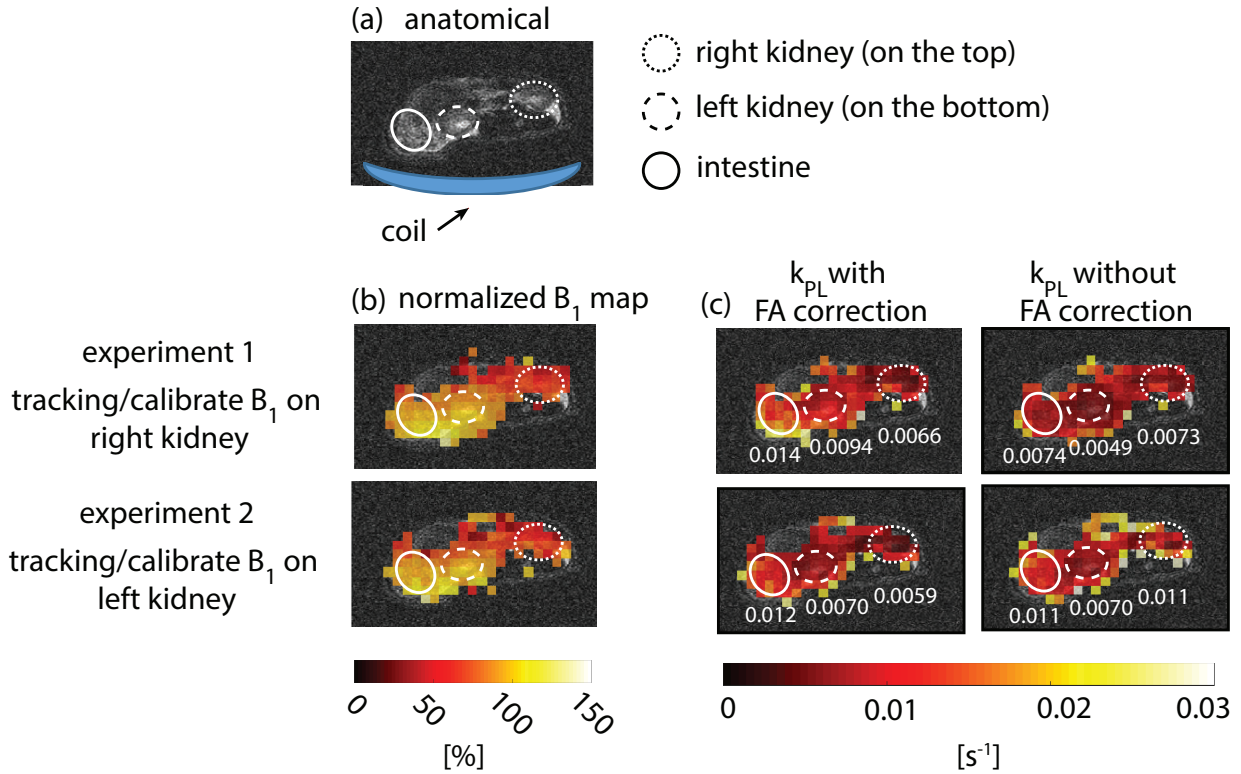0.011 0.0070 0.011

0   50   100   150

[%]

0   0.01   0.02   0.03

[s^{-1}]

Figure 3.6: Results of two hyperpolarized [1-^{13}C]pyruvate studies in a normal rat using the proposed method (Fig. 4.1) with a ^{13}C surface transceiver coil. The two experiments were performed with the same parameters except for different tracking/calibrating ROIs: experiment #1 on right kidney and #2 was on left kidney, where the left kidney is closer to the coil. Injection time was 10 s and initial power was the same as the calibrated power in pre-scan. Sequence parameters are presented in Table 3.1. (a) Proton localizer. (b) Normalized ^{13}C B_1 maps. B_1 maps acquired in two experiments are consistent. (c) Estimated k_{PL} with and without flip angle correction based on measured B_1 map. k_{PL} values for left kidney, right kidney and intestine are labeled in the maps. Using acquired B_1 maps to correct flip angle results in more consistent k_{PL} estimations of those ROIs between the two experiments, demonstrating the importance of flip angle correction for k_{PL} measurements. Experiment recordings: https://youtu.be/Mu3NW7Kog9M, https://youtu.be/fL5gVkPDw2o.

3.4.2 Human Results

Data from the four HP ^{13}C exams are presented in Fig. 3.7 to Fig. 3.10. The bolus arrival and peak were successfully detected in these studies, indicating the selected tracking threshold staying above the noise level. Compared to the frequency calibrated on the phantom, the real-time calibrated frequency had a larger difference in the kidney (-49Hz, Fig. 3.9), heart (-24Hz, Fig. 3.8), and prostate (20Hz, Fig. 3.10) studies than in the brain study (0Hz, Fig. 3.7). This finding is as expected, since large field inhomogeneity was present in the abdominal studies.

Compared to the B1 calibrated on the urea phantom, the real-time calibrated B1 within the body had a larger difference in the kidney (25%, Fig. 3.9), heart (30%, Fig. 3.8), prostate (30%, Fig. 3.10) studies than in the brain study (4%, Fig. 3.7). This finding is as expected, since the transmit coil (birdcage) used in the brain study has a more uniform transmission profile than what was used in other studies (clamshell or surface coil). Non-uniform transmission profile brings more challenges in power calibration. Since B1 mapping is triggered according to ROI bolus signal, sufficient signal is guaranteed at the ROI location but not necessarily in other regions. If B1 map of a large FOV is required, B1 mapping could be triggered manually according to the signal build-up which is also allowed in our real-time framework. Metabolite specific images were successfully acquired in all these studies with no apparent signal reduction, compared to our prior studies which didn't use bolus tracking and real-time B0/B1 calibration. This indicated that the small flip angle used in the tracking and real-time calibration process caused minimal hyperpolarization loss.

Figure 3.7: Results of hyperpolarized ^{13}C studies in the human brain using the acquisition scheme in Fig. 4.1. The metabolite images are from a sum across the dynamic acquisition. A birdcage transmit coil and a 32 channel receive coil are positioned surrounding the brain. The ROI for bolus tracking and B1 calibration was on the brain tissue near the superior sagittal sinus. The real-time measured pyruvate frequency was the same as the frequency calibrated in the pre-scan. The real-time measured ROI B1 was 4% higher than what was calibrated in the pre-scan. The link of the experiment recording is https://youtu.be/Oq36Z7ayQ0g

Figure 3.8: Results of hyperpolarized ^{13}C studies on the human heart using the acquisition scheme in Fig. 4.1. The metabolite images are from a sum across the dynamic acquisition. A clamshell transmit coil was positioned on the anterior and posterior sides of the subject and 8 channel paddle receive coils were positioned on the anterior and left sides of the chest. The ROI for bolus tracking and B1 calibration was placed on the right ventricle. The real-time measured pyruvate frequency was 24Hz downfield from the frequency calibrated in the pre-scan. The real-time measured B1 was 70% of what was calibrated in the pre-scan.
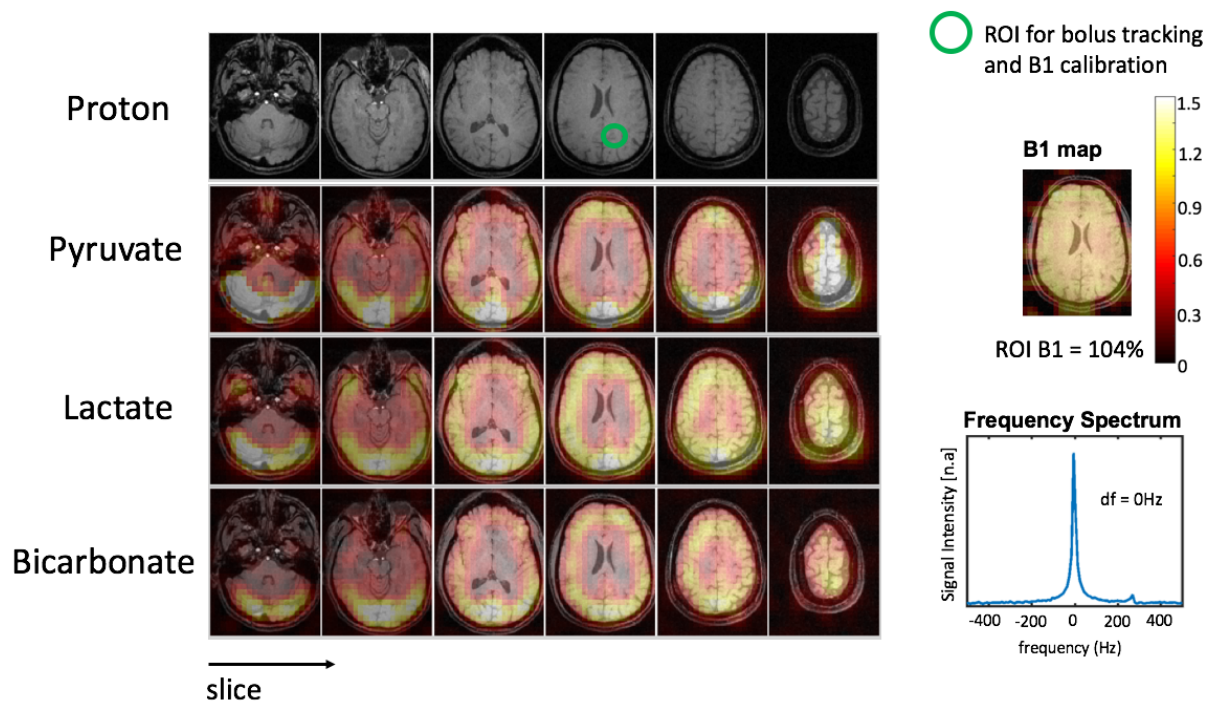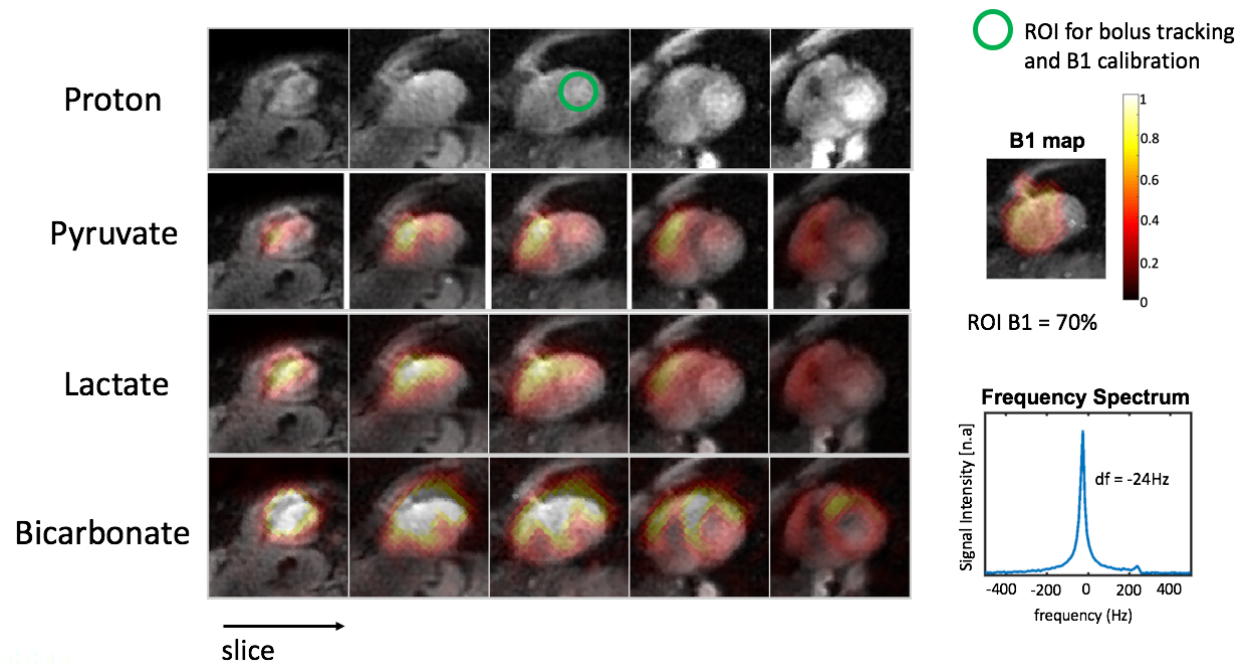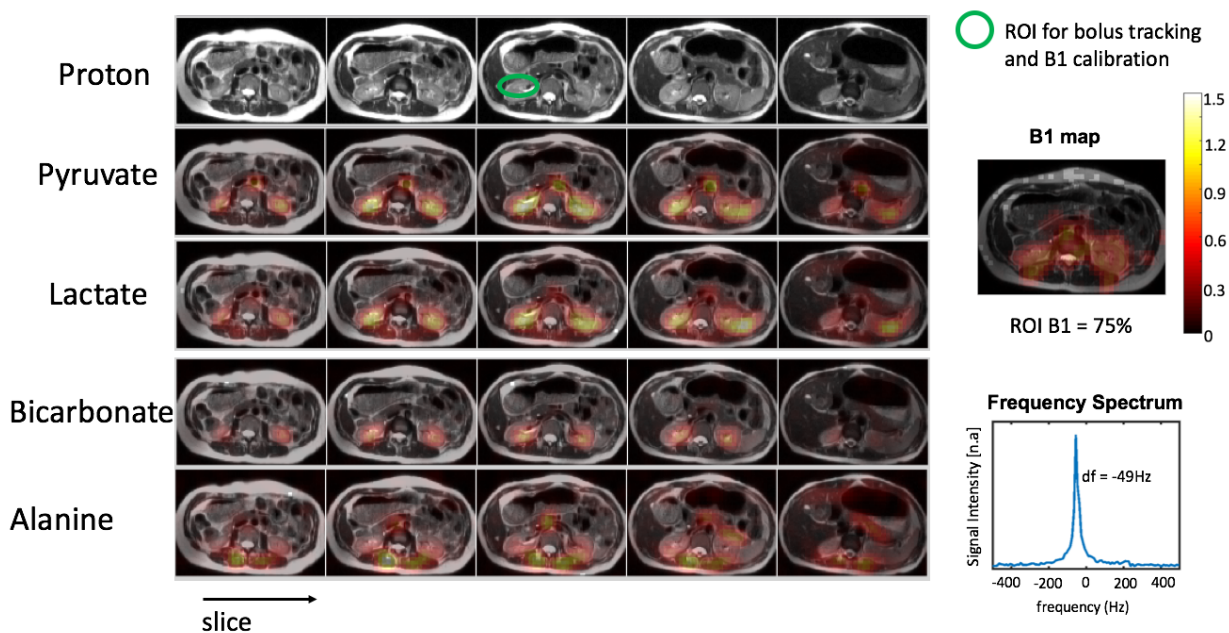
Figure 3.9: Results of hyperpolarized ^{13}C studies on the human kidneys using the acquisition scheme in Fig. 4.1. The metabolite images are from a sum across the dynamic acquisition. A clamshell transmit coil was positioned on the anterior and posterior sides of the subject and a 16 channel receive coil was positioned on the anterior and posterior sides of abdomen. The ROI for bolus tracking and B1 calibration was placed on the right kidney. The real-time measured pyruvate frequency was 49Hz downfield from the frequency calibrated in the pre-scan. B1 difference was observed between the left and right kidneys whose B1 values are 75% and 67% of the B1 value calibrated in the pre-scan. The link of the experiment recording is https://youtu.be/Joc9LABNRbc
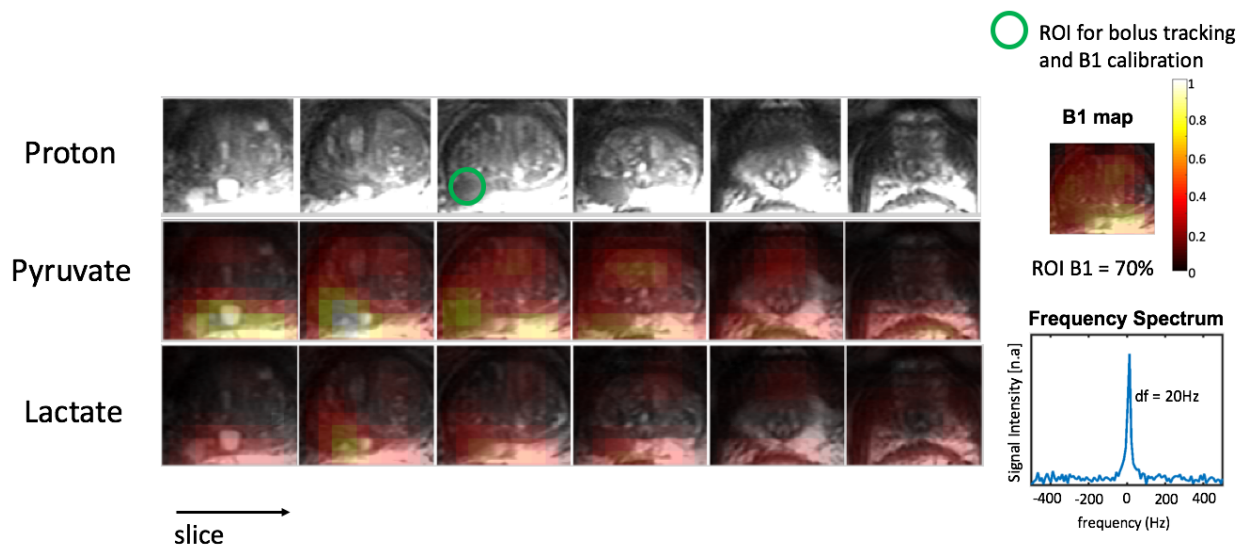
Figure 3.10: Results of hyperpolarized ^{13}C studies on a human prostate tumor using the acquisition scheme in Fig. 4.1. The metabolite images are from a sum across the dynamic acquisition. A clamshell transmit coil was positioned on the anterior and posterior sides of the subject and an endorectal coil was used for receive. The ROI for bolus tracking and B1 calibration was on the tumor. B1 calibration in the experiment is triggered on the bolus peak rather than on the bolus arrival, which would allow a broader perfused region of injected pyruvate and thus lead to a larger coverage of acquired B1 maps. The real-time measured pyruvate frequency was 20Hz upfield from the frequency calibrated in the pre-scan. The real-time measured B1 was 70% of what was calibrated in the pre-scan.

3.5   Discussion

As discussed in the Introduction section, automatic acquisition timing via bolus tracking improves efficient use of hyperpolarization as well as consistency and accuracy of hyperpolarized ^{13}C imaging. Furthermore, accurate timing is critical for some optimal variable flip angle schemes and metabolic quantification [61, 37, 64, 31]. The implementation of regional bolus tracking in this work improves the flexibility and accuracy of acquisition timing, and it would be especially useful for imaging tissue with low perfusion rate where injected metabolites would arrive at the target region later relative to major vessels or other tissues. The resolution of the bolus tracking image should be chosen as coarse as possible to improve image SNR but fine enough to detect the desired tracking region (e.g. major vessels from other tissues). An alternative approach is to use 2D spatially selective excitation pulses, but this approach is less robust to signals from off-resonance metabolites. In this study, bolus tracking triggered its following sequences either upon bolus arrival or following peak detection. This could easily be modified to use other schemes, such as starting metabolic imaging during the bolus or adding an additional delay from the peak. Manually triggering sequences during bolus tracking is also allowed in the designed framework and is useful if the automatic tracking algorithm fails. The bolus tracking used a flip angle of 5° and a TR of 1 s. Assuming an injection time of 10s, the expected total hyperpolarized signal loss due to bolus tracking RF pulses would be less than 4%.

The naturally low-abundance ^{13}C signal requires real-time B_1 mapping for accurate in vivo measurements of RF power in hyperpolarized ^{13}C imaging. The acquired B_1 map is useful for flip angle correction of images and is crucial for quantification of metabolism (e.g. k_{PL}[53]) as demonstrated in in vivo results (Fig. 3.6). Real-time B_1 calibration could achieve accurate flip angle during the scan, which is critical for variable flip angle schemes and large flip angle pulses [49], and avoiding unnecessary use of hyperpolarization. The upper limit of the B_1 measurement depends on the K_{BS} value of the Bloch-Siegert pulse while the lower limit depends on the SNR. 2D phase unwrapping could be implemented in real time to extend the upper limit of B_1 measurement. Real-time masking of the acquired B_1 map based on signal intensity made the real-time B_1 calibration robust when the B_1 calibration ROI contained regions with low hyperpolarized signal. The two TRs required for the B1

mapping sequence used a pyruvate flip angle of 10°, using only 3% of the hyperpolarization magnetization.

Center frequency calibration is crucial for metabolite specific imaging. For singleband spectral-spatial pulses, frequency calibration errors will reduce the flip angle and may also excite undesired resonances. For spiral or echo-planar imaging (EPI) readouts, frequency calibration errors will lead to off-resonance blurring and shift artifacts. Both of these factors can undermine the accuracy of Bloch-Siegert B1 mapping and quantification of metabolism. Frequency calibration based on a thermal ^{13}C phantom, which must be placed external to the subject, doesn't represent frequency within the subject. Although B_0 maps can be obtained via proton imaging, in vivo shimming could still be challenging, particularly in the presence of motion. In this study, real-time center frequency was triggered upon bolus arrival, which improved the quality of all the following real-time reconstructed images (Fig. 4.7e). The 102ms readout duration of the center frequency measurement sequence resulted in a $\sim$10Hz frequency resolution which could be improved with a longer readout duration. A 3° flip angle costs less than 0.2% of the hyperpolarized magnetization.

The transition time between acquisitions is mainly attributed to real-time image reconstruction and loading sequence waveforms. For animal experiments using single-channel acquisition, the transition times of a bolus tracking acquisition, real-time center frequency calibration, real-time B_1 calibration and their following sequences were about 60ms, 60ms and 400ms, respectively. For human experiments, a longer transition time ($\sim$800ms) was observed for real-time B_1 calibration, whereas transition times for bolus tracking acquisition and real-time center frequency calibration remained similar. The longer transition time found in B_1 calibration could be caused by its more complicated reconstruction compared to frequency calibration, and its shorter TR compared to a bolus tracking acquisition which typically used a TR of 1s and allowed real-time reconstruction to be completed during the dead time of a TR.

A ^{13}C-pyruvate and ^{13}C-urea co-polarized injection [60] would benefit substantially from the proposed methods. ^{13}C-urea could be used to perform bolus tracking, real-time center frequency and B_1 calibration. This strategy would fully preserve hyperpolarized signal of pyruvate[9] and provide higher SNR for B_1 mapping by using a larger flip angle. Cardiac and respiratory motion could detrimentally affect bolus tracking and Bloch-Siegert B_1 mapping.

Cardiac gating could be used [25]. In terms of respiratory motion, breathholding is often used in clinical studies. Respiratory gating is not suitable for bolus tracking due to large potential delays but can be applied to perform B_1 mapping at the end of exhalation[25], in which case, a short TR (200ms) as used in this study is recommended. A more challenging but robust approach to handle motion is to perform real-time image registration. To extend the proposed scheme for volumetric calibration, real-time center frequency and B_1 calibration can be integrated with a multislice imaging framework[25].

3.6   Conclusion

This work demonstrated an approach that integrates automatic acquisition timing using the regional bolus signal with real-time center frequency calibration, Bloch-Siegert B_1 mapping and real-time RF power compensation based on regional B_1 measurements as well as dynamic hyperpolarized ^{13}C imaging. This scheme allows for timing the acquisition based on bolus information of a local region within the imaging plane. Real-time center frequency calibration and B_1 calibration, ensures accurate center frequency and flip angles which are used in the following hyperpolarized ^{13}C sequences. The theoretical total hyperpolarized signal loss caused by the proposed bolus tracking and real-time frequency/power calibration is less than 7%. The proposed scheme was successfully demonstrated for animal and human hyperpolarized [1-^{13}C]pyruvate imaging on a clinical 3T scanner. Future work will focus on incorporating pyruvate-urea co-polarized injections, volumetric calibration and motion-compensation methods into the proposed scheme to improve efficiency, accuracy, and robustness of hyperpolarized ^{13}C studies.

Chapter 4

A Metabolite Specific 3D Stack-of-Spiral bSSFP Sequence for Improved Lactate Imaging in Hyperpolarized [1-^{13}C]Pyruvate Studies

4.1 Abstract

The balanced steady-state free precession (bSSFP) sequence has been previously explored to improve the efficient use of non-recoverable hyperpolarized ^{13}C signal, but suffers from poor spectral selectivity and limited matrix size. The purpose of this study was to develop a novel metabolite-specific 3D bSSFP ("MS-3DSSFP") sequence with stack-of-spiral readouts for improved lactate imaging in hyperpolarized [1-^{13}C]pyruvate studies on a clinical 3T scanner. Simulations were performed to evaluate the spectral response of the MS-3DSSFP sequence. Thermal ^{13}C phantom experiments were performed to validate the MS-3DSSFP sequence. In vivo hyperpolarized [1-^{13}C]pyruvate studies were performed in rodents and human to compare the MS-3DSSFP sequence with gradient echo sequences for lactate imag-

ing. Simulations, phantom and in vivo studies demonstrate that the MS-3DSSFP sequence achieved spectrally selective excitation on lactate while minimally perturbing other metabolites. Compared with GRE sequences, the MS-3DSSFP sequence showed approximately a 2.5X SNR improvement for lactate imaging in rat kidneys, prostate tumors in a mouse model and human kidneys. Improved lactate imaging using the MS-3DSSFP sequence in hyperpolarized [1-^{13}C]pyruvate studies was demonstrated in animals and humans. The MS-3DSSFP sequence could be applied for other clinical applications such as in the brain or adapted for imaging other hyperpolarized ^{13}C metabolites such as pyruvate and bicarbonate.

4.2   Introduction

The MR signals of hyperpolarized [1-^{13}C]pyruvate (173 ppm) and its downstream metabolites - [1-^{13}C]lactate (185 ppm), [1-^{13}C]pyruvate hydrate (181 ppm), [1-^{13}C]bicarbonate (163 ppm) and [1-^{13}C]alanine (178 ppm) - are typically acquired using gradient echo ("GRE") sequences (CSI[14], multi-echo IDEAL[45, 59], metabolite specific EPI[7, 15] or spiral[26] acquisition) where the transverse magnetization is spoiled at the end of each repetition time. Compared to GRE acquisitions, the balanced steady state free precession ("bSSFP") [54] sequence can acquire the nonrenewable hyperpolarized magnetization more efficiently by repetitively refocusing transverse spins, which is especially valuable for imaging metabolites with long T2s such as [1-^{13}C]pyruvate or [1-^{13}C]lactate [28, 36, 34, 35, 52].

Our work focuses on improving lactate imaging with hyperpolarized [1-^{13}C]pyruvate injections using a bSSFP framework. Three bSSFP strategies for lactate imaging have been proposed in prior works. The first strategy [28] utilized a broadband pulse to excite all components (i.e. pyruvate, lactate, bicarbonate, alanine, pyruvate-hydrate) in [1-^{13}C]pyruvate studies and decomposed the spectral information using multi-echo readouts. By acquiring all compounds at one time, this strategy limits the acquisition optimization (e.g. flip angle, resolution) for individual compounds and requires longer acquisition times if not all the compounds in the spectrum are of interest.

The second strategy [35] reduced the number of excited compounds - only exciting lactate, pyruvate hydrate and alanine - and applied a saturation pulse to suppress undesired signals from alanine and pyruvate hydrate at the beginning of each bSSFP acquisition. There

are three main drawbacks in this strategy. Since the conversion between pyruvate hydrate and pyruvate maintains an equilibrium in the liquid state [41], the pre-saturated pyruvate hydrate signal may recover fast enough to contaminate lactate acquisitions at later bSSFP echoes. Directly saturating pyruvate hydrate would also accelerate the loss of pyruvate magnetization and thus reduce the signals of downstream metabolites. In addition, the saturation performance may be imperfect in the regions where transmit B1 profile is not homogeneous.

The third strategy [52] excited one metabolite at a time (i.e. metabolite specific excitation) and was applied for imaging [1-^{13}C]urea, [1-^{13}C]pyruvate and [1-^{13}C]lactate with the bSSFP sequence on a 14.1T scanner. To meet the constraint of a short TR required in bSSFP sequences, this strategy designed a multiband RF pulse using a convex optimization approach [51]. Compared with single-band RF pulses, multiband RF pulses could potentially shorten the RF duration by releasing the constraints on frequency ranges of no interest. Our work adapted this strategy to a clinical 3T scanner.

This chapter presents a novel metabolite specific 3D bSSFP sequence ("MS-3DSSFP") with stack-of-spiral readouts for improved dynamic lactate imaging in hyperpolarized [1-^{13}C]pyruvate studies on a clinical 3T scanner. A lactate specific excitation pulse was developed using a previously described approach [51]. Stack-of-spiral readouts were used to accelerate the acquisition. The excitation profile of the newly designed RF pulse at the bSSFP state was simulated to investigate the banding artifacts and to examine the spectral selectivity of the RF pulse. Thermally polarized ^{13}C phantom experiments were performed to validate the MS-3DSSFP sequence. In vivo hyperpolarized [1-^{13}C]pyruvate experiments were performed on healthy rats, prostate cancer mouse model and patients with renal tumors to compare the MS-3DSSFP sequence with metabolite specific GRE ("MS-GRE") sequences, in the aspects of signal-to-noise ratio (SNR), image artifacts and impact on other metabolites.

4.3 Methods

4.3.1 Sequence design and simulation

The MS-3DSSFP sequence (Fig. 4.1) consists of a multiband RF pulse and a center-out 3D uniform-density stack-of-spiral readout. The RF pulse was designed using a prior approach [51] to minimize the pulse duration. This pulse had a duration of 9ms, a maximum B1 of 0.2195G, a 40Hz passband on lactate (0Hz), a 40Hz stopband with 5% ripples on pyruvate hydrate (-128Hz) and 40Hz stopbands with 0.5% ripples on bicarbonate (-717Hz), pyruvate (-395Hz) and alanine (-210Hz). The 3D stack-of-spiral trajectory consists of 16 stacks and each stack consists of four 3.8ms interleaves. All gradients have zero net area over the course of one repetition. A 6 pulse non-linear ramp preparation scheme (i.e. 4°, 16°, 24°, 36°, 48°, 60° for a flip angle of 60°) was used to achieve a stable frequency response while the reverse-ordered pulses were used for tip back. The MS-3DSSFP sequence was implemented on a GE Signa MR 3T scanner (GE Healthcare, Waukesha, WI) using a commercial software (RTHawk, HeartVista, Los Altos, CA).

In the bSSFP sequence, TR determines the frequency locations of banding artifacts, which occur at repetitions of 1/TR. A TR of 15.3ms was used for the MS-3DSSFP sequence to maximize the distance between banding artifacts and metabolite frequencies. The excitation profiles of the RF pulse and its averaged transverse magnetization over all echoes of bSSFP acquisitions were simulated. Simulation parameters were: number of RF pulses = 50, TR = 15.3ms, T1 = 30s, T2 = 1s, 6 non-linear ramp preparation pulses, flip angle = 60°.

The choice of flip angle for the bSSFP sequence in the hyperpolarized study is a tradeoff between banding artifacts and preserving magnetization for dynamic imaging. Prior bSSFP work [43] has shown a favorable use of large flip angle ($>100^o$) to reduce banding artifacts. However, to perform dynamic imaging in hyperpolarized studies, a small flip angle around 30° in MS-GRE acquisitions [37] (equivalent to 60° in the bSSFP sequence) was required to maintain sufficient SNR for multiple time points. In our work, we used a flip angle of 60° to achieve a compromise between the two considerations.
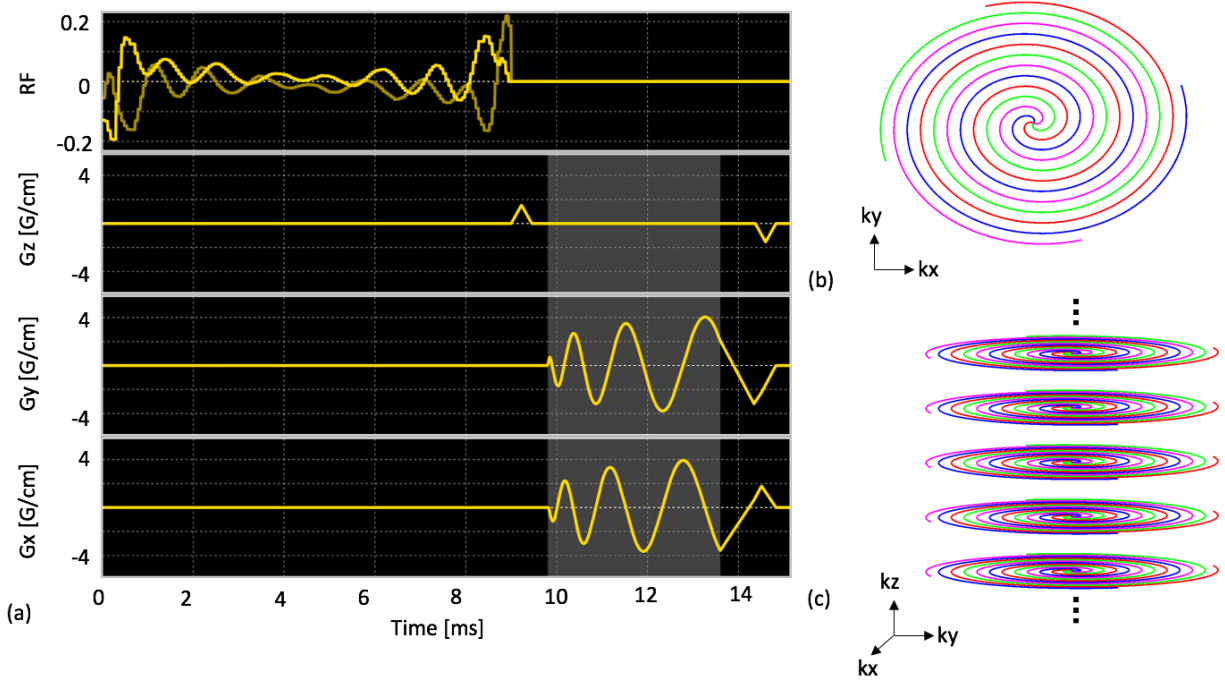
Figure 4.1: Pulse sequence of the proposed MS-3DSSFP sequence (a). It consists of a lactate specific excitation pulse and a 3D center-out stack of spiral readout (c). Each stack (b) consists of four interleaves. The details of the excitation pulse are described in Fig. 4.3.

4.3.2 Phantom and Animal Experiments

To test the MS-3DSSFP sequence, phantom experiments were performed on a ^{13}C-enriched sodium bicarbonate syringe phantom (T1 $\approx$ 26s, T2 $\approx$ 1.5s) with a dual-tuned ^{1}H/^{13}C transceiver birdcage coil. 3D images of the phantom were acquired along with proton images and field maps. To test the excitation profile, ^{13}C images were also acquired at the frequencies of lactate, pyruvate hydrate, alanine, pyruvate and bicarbonate. At the frequency of each metabolite, ^{13}C images were acquired at the frequency offsets from -30 to 30 Hz with a step of 10Hz.

Hyperpolarized [1-^{13}C]pyruvate animal experiments were performed on healthy Sprague-Dawley rats (N = 3) and transgenic adenocarcinoma of mouse prostate (TRAMP) mice (N = 3) to test our MS-3DSSFP sequence in vivo. ^{13}C/^{1}H birdcage coils (8cm diameter for rats, 5cm diameter for mice) were used. All animal studies were conducted under protocols

45

approved by the University of California San Francisco Institutional Animal Care and Use Committee (IACUC). Both rats and mice were anesthetized with isoflurane (1-2%) and placed in a supine position on a heated pad throughout the duration of the experiments. [1-^{13}C]pyruvic acid (Sigma Aldrich, St. Louis, MO) mixed with 15mM trityl radical (GE Healthcare, Waukesha, WI) and 1.5mM Gd-DOTA (Guerbet, Roissy, France) was polarized in a 3.35T SPINlab polarizer (GE Healthcare, Waukesha, WI) at 0.8K for ∼1h, resulting in a 80mM [1-^{13}C]pyruvate solution, with final pH of 6-8. The hyperpolarized [1-^{13}C]pyruvate was injected into the animal via tail vein catheters, ∼3mL for each rat and ∼350μL for the mouse.

Hyperpolarized ^{13}C sequence parameters for animal experiments are shown in Table 4.1. Each animal received two injections of same dose of [1-^{13}C]pyruvate. Lactate signals were acquired using the MS-3DSSFP sequence in one injection ("experiment A") but using a 3D MS-GRE sequence (described below) in the other injection ("experiment B"). Pyruvate and alanine signals were acquired using the same 3D MS-GRE sequence in both injections. This experiment design where different acquisitions were used for lactate while same MS-GRE acquisitions were used for pyruvate and alanine allows comparing the MS-3DSSFP sequence with a MS-GRE sequence for lactate imaging, as well as examining the perturbation of the MS-3DSSFP sequence on pyruvate and alanine signals. Bicarbonate signals were not acquired due to its inherently lower signals which would not provide sufficient signals to compare between the two sequences.

The 3D MS-GRE sequence consists of a single-band spectral-spatial excitation (130Hz FWHM passband, 870Hz stopband) [16] and stack-of-spiral readouts. Each stack was a 22ms single-shot spiral readout. The two injections shared the same spatial resolution, temporal resolution and number of time points. The 3D MS-GRE sequence used 16 excitations for a 3D encoding and each excitation pulse used a flip angle of 7.67^o so that the equivalent flip angle of these 16 excitations was the same as a 60° flip angle used in the MS-3DSSFP sequence. The effective flip angle θ_{eq} of N excitations with a flip angle of θ for each excitation is calculated as arccos(cos($\theta)^N$). Initial pre-scan frequency and power calibration were performed on a ^{13}C urea phantom which was removed before pyruvate injection. All acquisitions were started 6s after the end of pyruvate injection. For each experiment, a ^{13}C frequency spectrum was acquired and real-time ^{13}C B1 calibration [55] was performed right before metabolite

Table 4.1: ^{13}C sequence parameters used in rat, TRAMP and human studies with hyperpolarized [1-^{13}C]pyruvate injection. For the same subject, two experiments (A and B) would be performed back-to-back for comparison. In experiment A, lactate signals were acquired with the metabolite specific 3D SSFP (MS-3DSSFP) sequence while pyruvate and alanine signals were acquired with the metabolite specific GRE (MS-GRE) sequences. In experiment B, all three metabolites were acquired with MS-GRE sequences. In TRAMP mouse studies and one of the human study, experiment B was performed first. In other studies, experiment A was performed first.

Sequence parameters for rat and TRAMP studies

	Experiment A	Experiment B
Pyruvate	3D MS-GRE, FOV 12x12x16cm, res 4x4x10mm, Tread 22ms, temporal resolution 4s, flip angle 3º for pyruvate, flip angle 30º for alanine	
Alanine		
Lactate	MS-3DSSFP, FOV 9.4x9.4x16cm, res 4x4x10mm, Tread 3.8ms, TR 15.29ms, flip angle 60º	Same sequence as pyruvate and alanine except using flip angle 7.67º

Sequence parameters for human studies

	Experiment A	Experiment B
Pyruvate	Multi-slice 2D MS-GRE, FOV 45x45x33.6cm, res 15x15x21mm, Tread 22ms, temporal resolution 3.5s, flip angle 20º for pyruvate, flip angle 90º for alanine	
Alanine		
Lactate	MS-3DSSFP, FOV 69x69x33.6cm, res 15x15x21mm, Tread 3.8ms, TR 15.29ms, flip angle 60º	Same sequence as pyruvate and alanine except using flip angle 30º

acquisition.

For rat experiments, an anatomical localizer was acquired using proton 3D bSSFP sequence (FOV $16 \times 16 \times 17.92$cm, Matrix size $256 \times 256 \times 112$). For the TRAMP mice experiment, an anatomical localizer was acquired using proton T2-weighted fast spin echo sequence (FOV 6×6cm, Matrix size 512×512). For all animal experiments, a B0 map was acquired using IDEAL IQ sequence (FOV 32×32cm, Matrix size 256×256).

4.3.3 Human study

Hyperpolarized [1-^{13}C]pyruvate human studies (N = 2) were performed to demonstrate the feasibility of applying the MS-3DSSFP sequence in a clinical settings (4.1). Patients with renal tumors that required surgical removal were recruited with institutional review board approval and provided with written informed consent for participation in the study. An Investigational New Drug approval was obtained from the U.S. Food and Drug Administration for generating the agent and implementing the clinical protocol. 1.47g of Good Manufacturing Practices (GMP) [1-^{13}C]pyruvate (Sigma Aldrich, St. Louis, MO) mixed with 15mM electron paramagnetic agent (EPA) (AH111501, GE Healthcare, Oslo, Norway) was polarized using a 5T SPINlab polarizer (General Electric, Niskayuna, NY) for 3h before being rapidly dissolved with 130°C water and forced through a filter that removed EPA. The solution was then collected in a receiver vessel and neutralized with NaOH and Tris buffer. The receive assembly that accommodates quality-control processes provided rapid measurements of pH, pyruvate and EPA concentrations, polarization, and temperature. In parallel, the hyperpolarized solution was pulled into a syringe (Medrad Inc, Warrendale, PA) through a 0.2μm sterile filter (ZenPure, Manassas, VA) and transported into the scanner for injection. The integrity of this filter was tested in agreement with manufacturer specifications prior to injection. A 0.43mL/kg dose of $\sim$250mM pyruvate was injected at a rate of 5mL/s via an intra-venous catheter placed in the antecubital vein, followed by a 20mL saline flush.

In human studies, ^{13}C kidney images were acquired with in-house built clamshell transmit coil and 8-channel paddle receive array [57]. ^{13}C sequence parameters for this study are presented in Table 4.1. Similar to the experiment design in animal experiments, the patient received two injections to compare the MS-3DSSFP sequence with MS-GRE sequences. The MS-GRE sequence used in this study was a multi-slice 2D MS-GRE sequence with the same excitation pulse and the same single-shot spiral readout as used in the animal studies. ^{13}C dynamic imaging was started 6s after the bolus arrival in kidney which was monitored by a bolus tracking sequence [55]. Initial pre-scan frequency and power calibration were performed on ^{13}C urea phantom attached outside the receive coil, which was removed before pyruvate injection. Real-time ^{13}C frequency and power calibration [55] were performed on the renal tumor and triggered upon bolus arrival. Proton anatomical reference images were acquired

with a 4 channel paddle receive coil, using a 2D SSFSE sequence with FOV 38 × 38cm, matrix size 512 × 512.

4.3.4   Reconstruction and Data Analysis

For all studies, gridding of k-space data were performed using Kaiser-Bessel gridding method [20] (http://web.stanford.edu/class/ee369c/mfiles/gridkb.m) with an oversampling factor of 1.4 and a kernel width of 4.5. The gridded k-space data is zero-filled by a factor of 2, applied with a 2D fermi filter and inverse Fourier transformed to the reconstructed image. Multi-channel data were combined by using pyruvate signals as coil sensitivity maps [65].

Area-under-the-curve (AUC) images were calculated by summing the complex data through time. Signal-to-noise ratio (SNR) was calculated as signal magnitude divided by the mean of noise magnitude. Lactate-to-pyruvate AUC ratio images were calculated by dividing the SNR of lactate AUC images by the SNR of pyruvate AUC images. To compare AUC of a metabolite between experiment A (pyruvate/alanine: MS-GRE; lactate: MS-3DSSFP) and experiment B (pyruvate/lactate/alanine: MS-GRE) (Table 4.1), SNR of the AUC images was calculated and then divided by the SNR of pyruvate AUC images acquired in the same experiment. To compare dynamic curves of a metabolite between experiment A and experiment B, SNR of each time point was calculated and then divided by the highest SNR of the pyruvate dynamic curve acquired in the same experiment.

Signal levels of undesired metabolites in MS-3DSSFP lactate acquisitions were estimated. First, the concentration ratio between an undesired metabolite and lactate was estimated using the signals acquired from experiment B where all compounds were acquired with MS-GRE sequences. Flip angle was compensated in the concentration ratio. Next, to estimate the signal ratio between an undesired metabolite and lactate in MS-3DSSFP, the concentration ratio was multiplied with MS-3DSSFP point spread function (PSF) amplitude ratio between the undesired metabolite and lactate. The MS-3DSSFP PSF amplitude was calculated by multiplying MS-3DSSFP excitation profile with the simulated PSF amplitude of the MS-3DSSFP readout. The following equation describes the above calculation:

$$p_x = \frac{S_x * sin(\theta_l) * \delta_x * I_x}{S_l * sin(\theta_x)} \tag{4.1}$$

where p is the signal level (%) of an undesired metabolite x in MS-3DSSFP lactate acquisitions, l is lactate, S is the signal measured in experiment B, θ is the flip angle used in experiment B, δ is the stopband amplitude of the excitation RF pulse used in the MS-3DSSFP sequence, I is the central amplitude of the simulated off-resonance PSF of the interleaved spiral readouts used in the MS-3DSSFP sequence. Pyruvate hydrate signals were assumed to be as 8% of pyruvate signals [14]. Stopband amplitudes δ are described in pulse design: 0.5% for alanine, 0.5% for pyruvate and 5% for pyruvate hydrate. The off-resonance PSF amplitudes I of the MS-3DSSFP readouts are obtained from simulations (Fig. 4.2): 0.327 for alanine, 0.191 for pyruvate and 0.701 for pyruvate hydrate.

4.4 Results

Simulated excitation profiles of the MS-3DSSFP sequence and its averaged transverse magnetization over all bSSFP echoes are shown in Fig. 4.3. Frequency bands and stopband ripples of the excitation profiles were as desired. Most banding artifacts fell outside of the desired frequency bands except one banding artifact which was observed 18Hz upfield from the alanine frequency. In the simulation, the amplitude of this banding artifact was about a third of the on-resonance peak, although its actual value in a hyperpolarized ^{13}C pyruvate study depends on the T1 and T2 of alanine as well as the conversion rate between pyruvate and alanine.

Results of validating the MS-3DSSFP sequence on a [^{13}C]bicarbonate syringe phantom (T1 $\sim= 26$s, T2 $\sim= 1.5$s) with a rat birdcage coil are shown in Fig. 4.4. ^{13}C images, proton images and B0 maps scaled to ^{13}C frequency were provided. The dash-line-boxed slice shows a bright proton image but a dark ^{13}C image. This is consistent with the large B0 variation (-50Hz) at that slice corresponding to SSFP banding. Results of validating the excitation profile of the bSSFP sequence on the phantom are presented in Fig. 4.5. Excitation profiles measured from phantom experiments were found to be consistent with the simulation.

Results of representative hyperpolarized [1-^{13}C]pyruvate experiments to compare the MS-3DSSFP sequence with MS-GRE sequences using the experiment parameters in Table 4.1 are presented in Fig. 4.6 (rat), Fig. 4.7 (TRAMP mouse) and Fig. 4.8 (renal tumor patient). Comparing lactate AUC maps of the two experiments, no banding artifacts were
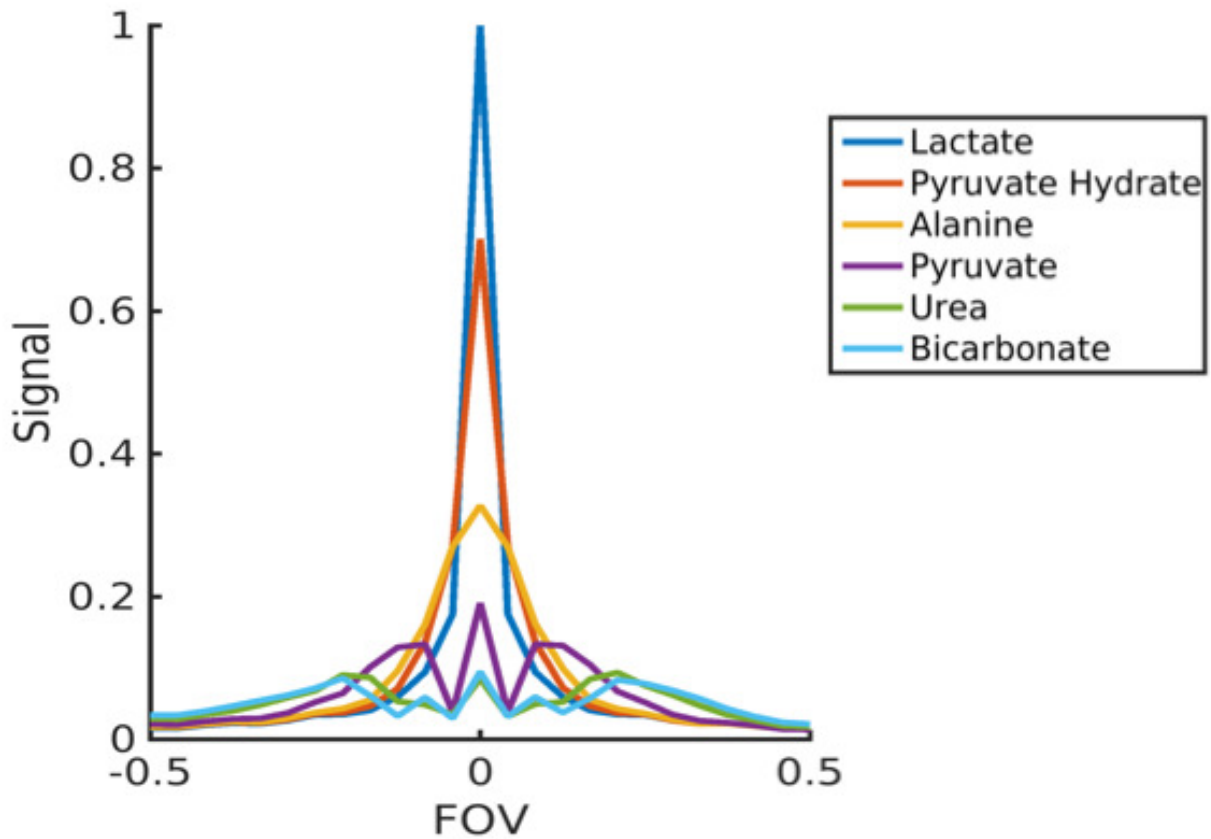
50

Figure 4.2: Simulations of off-resonance PSF of the interleaved spiral readouts (4 inter-leaves, 3.8ms for each interleaf) used in this study. Frequencies of metabolites are Lactate = 0Hz, Pyruvate Hydrate = -128Hz, Alanine = -210Hz, Pyruvate = -395Hz, Urea = -635Hz, Bicarbonate = -717Hz.

observed in the MS-3DSSFP results. This finding agrees with the homogenous B0 maps found in most areas of rat kidneys, TRAMP tumors and human kidneys, although large B0 variations are found near the tissue-air interfaces. In some tumor regions, lactate-to-pyruvate AUC ratio maps reveal different contrasts between the two experiments, as shown in Fig. 4.7 and Fig. 4.8. Compared to results of experiment B (pyruvate: MS-GRE; lactate: MS-GRE), lactate-to-pyruvate AUC ratio map of experiment A (pyruvate: MS-GRE; lactate: MS-3DSSFP) shows better alignment with the underlying T2 weighted proton images. This could be a result of T2 contrast provided by the MS-3DSSFP sequence. Higher values of lactate-to-pyruvate AUC ratio map are found in experiment A compared to experiment B, demonstrating the MS-3DSSFP sequence provides higher SNR over MS-GRE sequences. AUC maps of pyruvate and alanine show consistent contrast between the two experiments, demonstrating minimal perturbation of the newly designed MS-3DSSFP RF pulse on pyruvate and alanine.

Representative dynamic curves of lactate, pyruvate and alanine signals are presented in Fig. 4.9 acquired with experiment parameters described in Table 4.1. Metabolites signal ratios between the two experiments are presented in Fig. 4.13. Compared with MS-GRE sequences, the MS-3DSSFP sequence shows an overall approximately 2.5X SNR improvement and demonstrates higher SNR performance at every time point for lactate imaging in rat kidneys, tumors of TRAMP mice and human kidneys. Comparing AUC between the two experiments, there is almost no difference in pyruvate and a 5% to 20% difference in alanine AUC, which demonstrates the lactate spectral selectivity of the MS-3DSSFP sequence.

Signal levels of undesired metabolites (i.e. pyruvate and alanine) in MS-3DSSFP lactate acquisitions were quantified in three types of ROIs: rat kidneys, tumors of TRAMP mice and human kidneys (Table 4.2). The highest signal contribution from undesired metabolites was found in rat kidneys - 0.05% from alanine, 1.14% from pyruvate and 3.36% from pyruvate hydrate, where 1% means that the ratio between the undesired metabolite and lactate is 0.01.
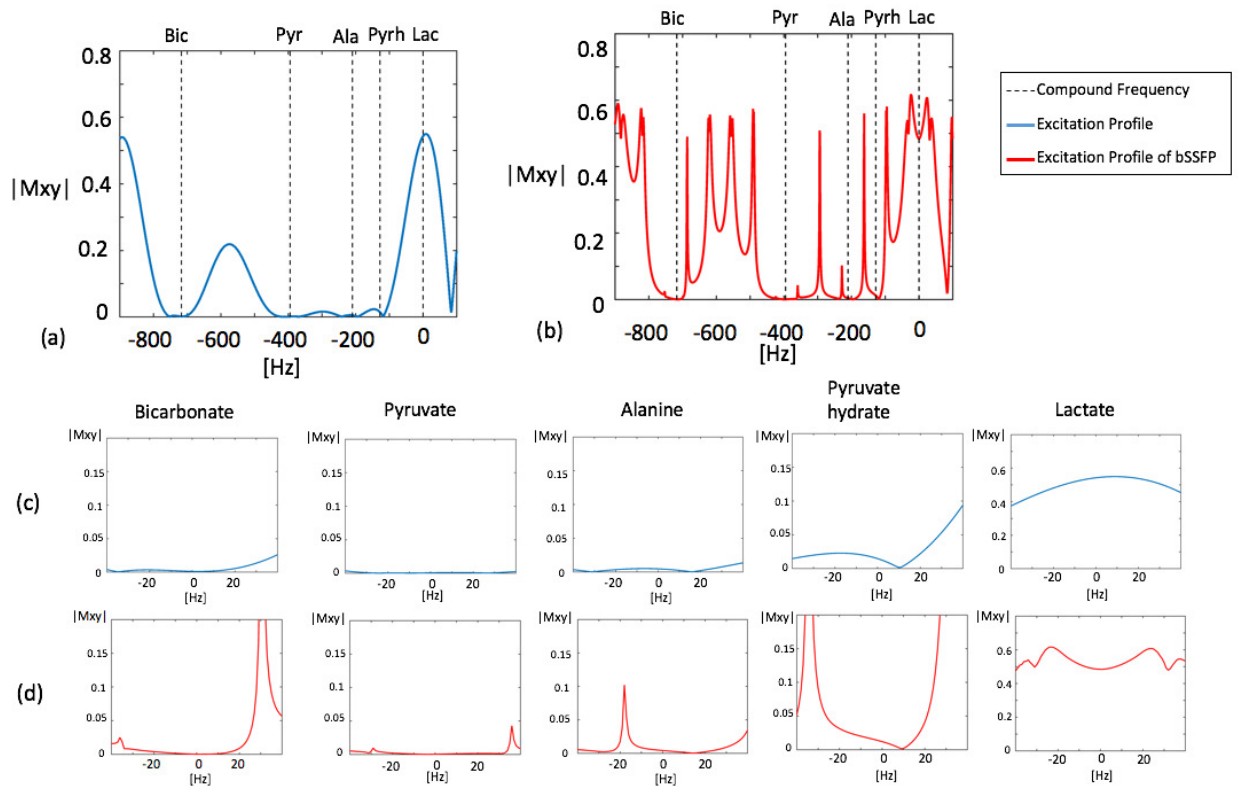
Figure 4.3: Simulated excitation profiles of the excitation pulse alone (blue) and its averaged transverse magnetization over all echoes of a bSSFP acquisition (red). An overall view of the profile is shown in graph (a) and graph (b). Zoomed views (±40Hz) of excitation profiles around each metabolite are shown in graph (c) and graph (d). The excitation pulse has a 40Hz passband on lactate (0Hz), a 40Hz stopband of 5% maximum ripple on pyruvate hydrate (-128Hz) and 40Hz stopbands of 0.5% maximum ripples on bicarbonate (-717Hz), pyruvate (-395Hz) and alanine (-210Hz). Simulation parameters for bSSFP acquisitions include: number of RF pulses = 64, TR = 15.3ms, T1 = 30s, T2 = 1s, 6 non-linear ramp preparation pulses, flip angle = 60°
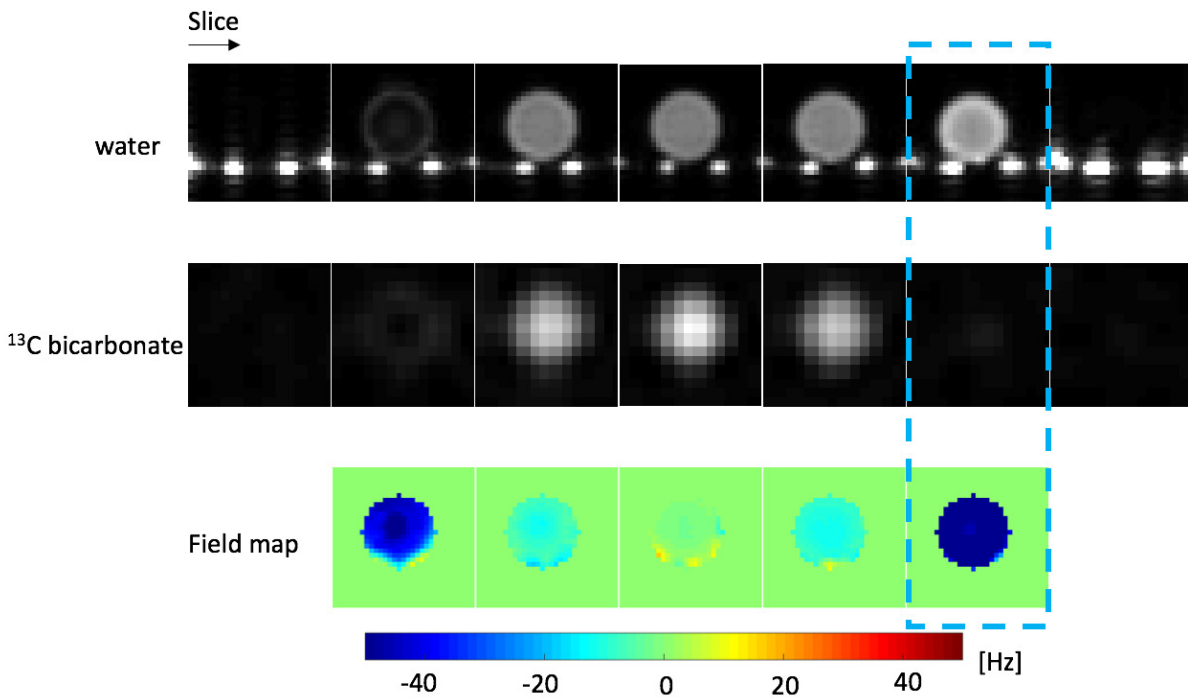
[H]

Figure 4.4: Validation of the MS-3DSSFP sequence on a [^{13}C]bicarbonate syringe phantom (T1 $\sim= 26$s, T2 $\sim= 1.5$s) with a rat birdcage coil. ^{13}C images were acquired at $8 \times 8 \times 20$mm and reconstructed at $4 \times 4 \times 20$mm. Bright spots at the bottom of proton images are the water pad in the coil. B0 maps are shown at ^{13}C frequency. The dash-line-boxed slice shows a bright proton image but a dark ^{13}C image, consistent with the large B0 variation (-50Hz) at that slice.
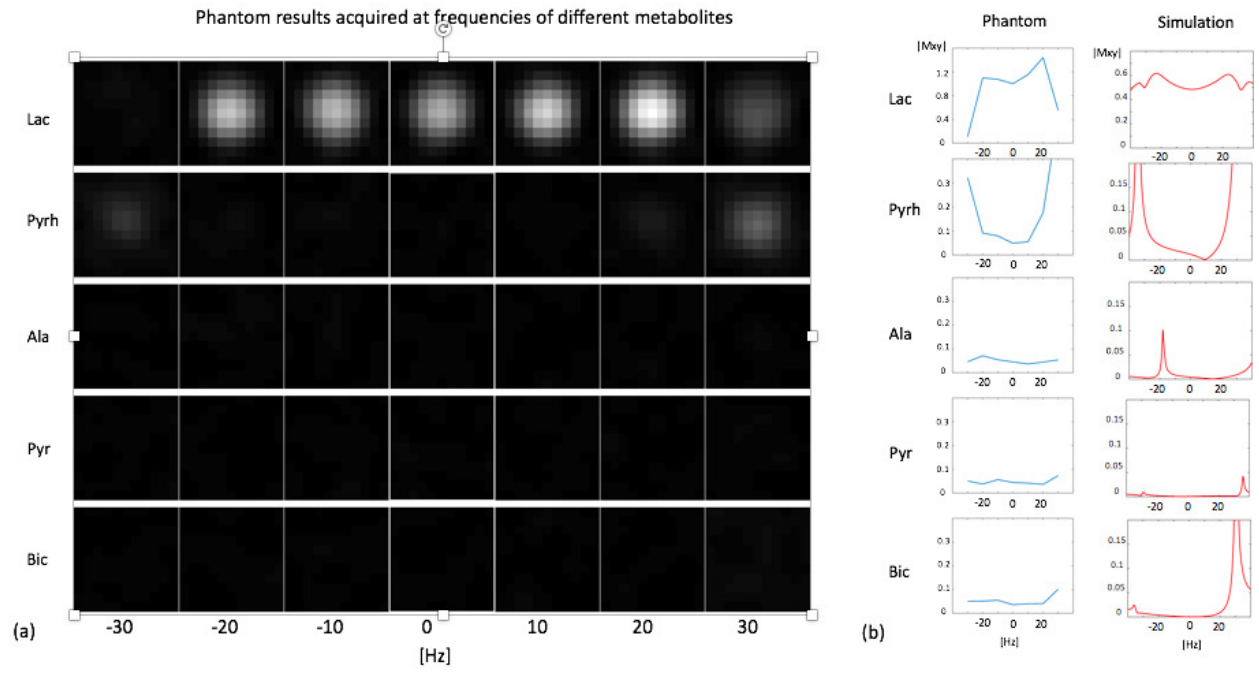
Figure 4.5: Validation of the MS-3DSSFP sequence on a ^{13}C-enriched sodium bicarbonate phantom (T1 = 26s, T2 = 1.5s). ^{13}C images were acquired at the frequencies of lactate ("Lac"), pyruvate hydrate ("Pyrh"), alanine ("Ala"), pyruvate ("Pyr") and bicarbonate ("Bic"). For each metabolite, ^{13}C images were acquired at the frequency offsets from -30 to 30 Hz with a step of 10Hz. All ^{13}C images were acquired at $8 \times 8 \times 20$mm and reconstructed at $4 \times 4 \times 20$mm. The mean value of the phantom area for each image is normalized by the value of the lactate image at zero frequency offset and plotted in graph (b). Simulation results from Fig. 4.3 are also displayed here for comparison.
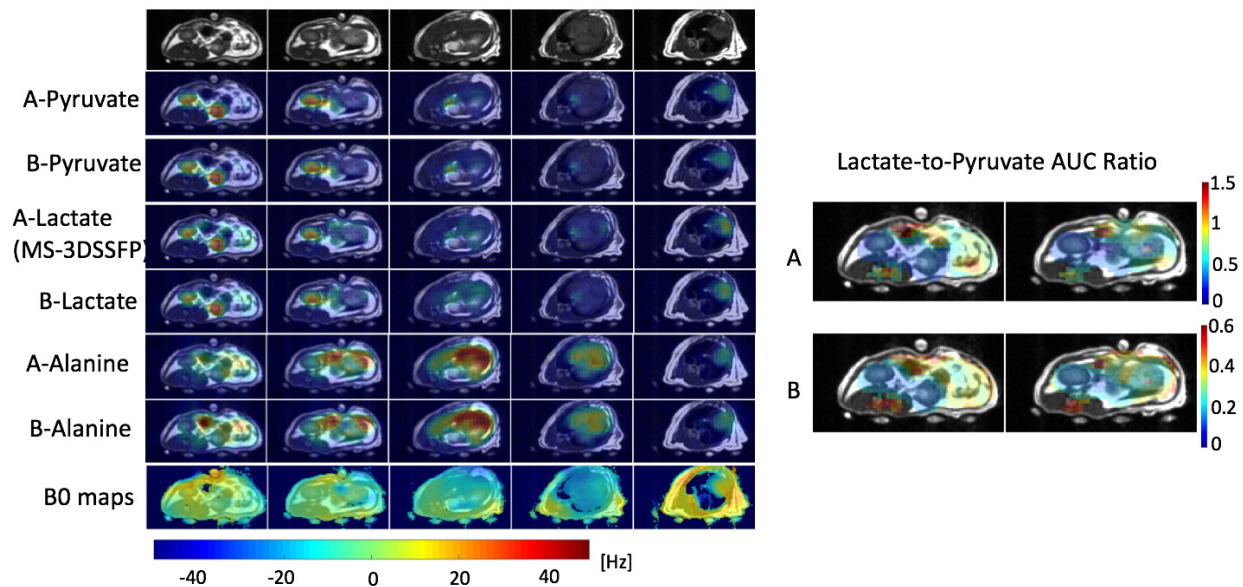
Figure 4.6: Comparison of the MS-3DSSFP sequence with a 3D MS-GRE sequence on a healthy rat with hyperpolarized [1-^{13}C]pyruvate injections using experiment A (pyruvate/alanine: MS-GRE; lactate: MS-3DSSFP) and experiment B (pyruvate/lactate/alanine: MS-GRE). Experiment parameters are described in Table 4.1. AUC maps of each metabolite are displayed windowed to the maximum signal across slices. B0 maps were thresholded using a mask removing the pixels with SNR lower than 3 in the water magnitude images. B0 maps colorbar is displayed at the bottom. Lactate-to-pyruvate AUC ratio maps of the kidney slices are shown and thresholded using a mask removing the pixels with SNR lower than 3 in the lactate or pyruvate magnitude image.
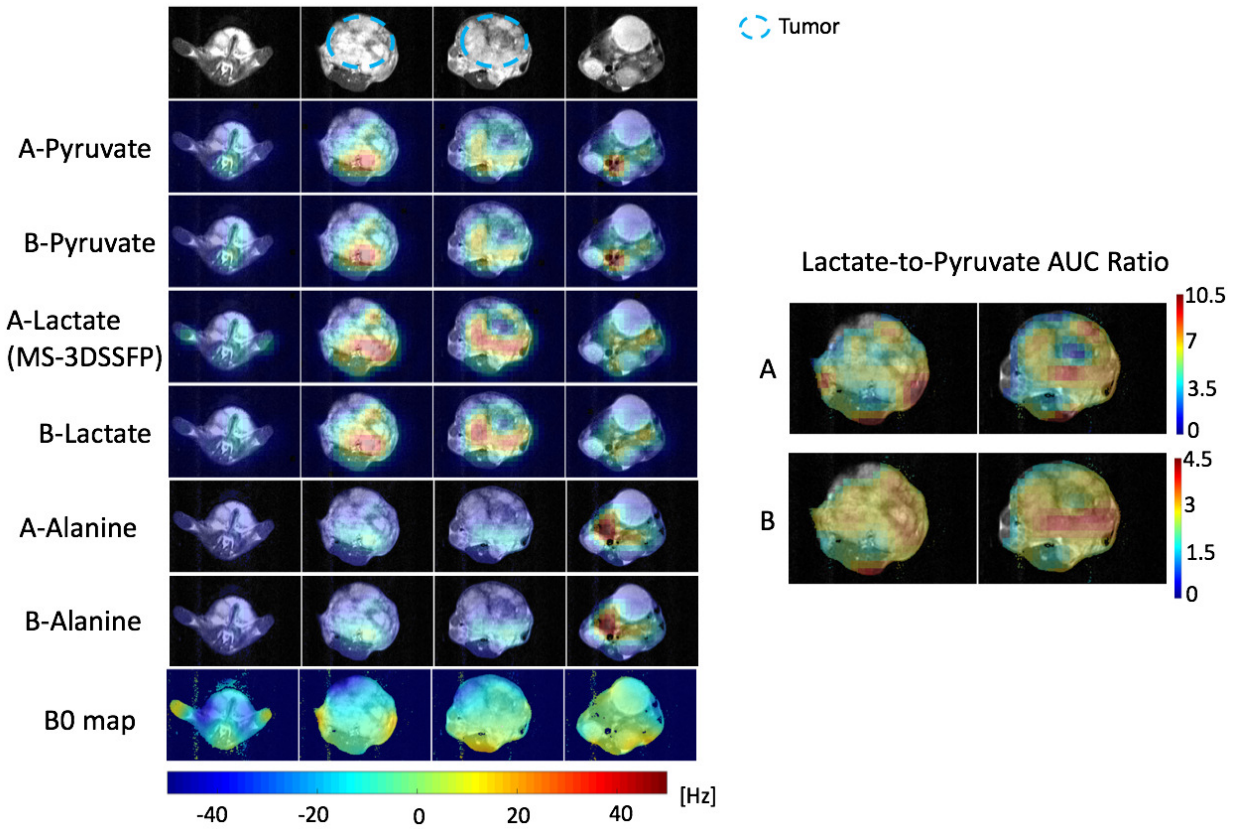
Figure 4.7: Comparison of the MS-3DSSFP sequence with a 3D MS-GRE sequence on a TRAMP mouse prostate tumor with hyperpolarized [1-^{13}C]pyruvate injections using experiment A (pyruvate/alanine: MS-GRE; lactate: MS-3DSSFP) and experiment B (pyruvate/lactate/alanine: MS-GRE). Experiment parameters are described in Table 4.1. AUC images of each metabolite, and lactate-to-pyruvate AUC ratio images and B0 maps are shown. B0 and AUC ratio maps are thresholded the same way as described in Fig. 4.6. B0 maps colorbar is displayed at the bottom.
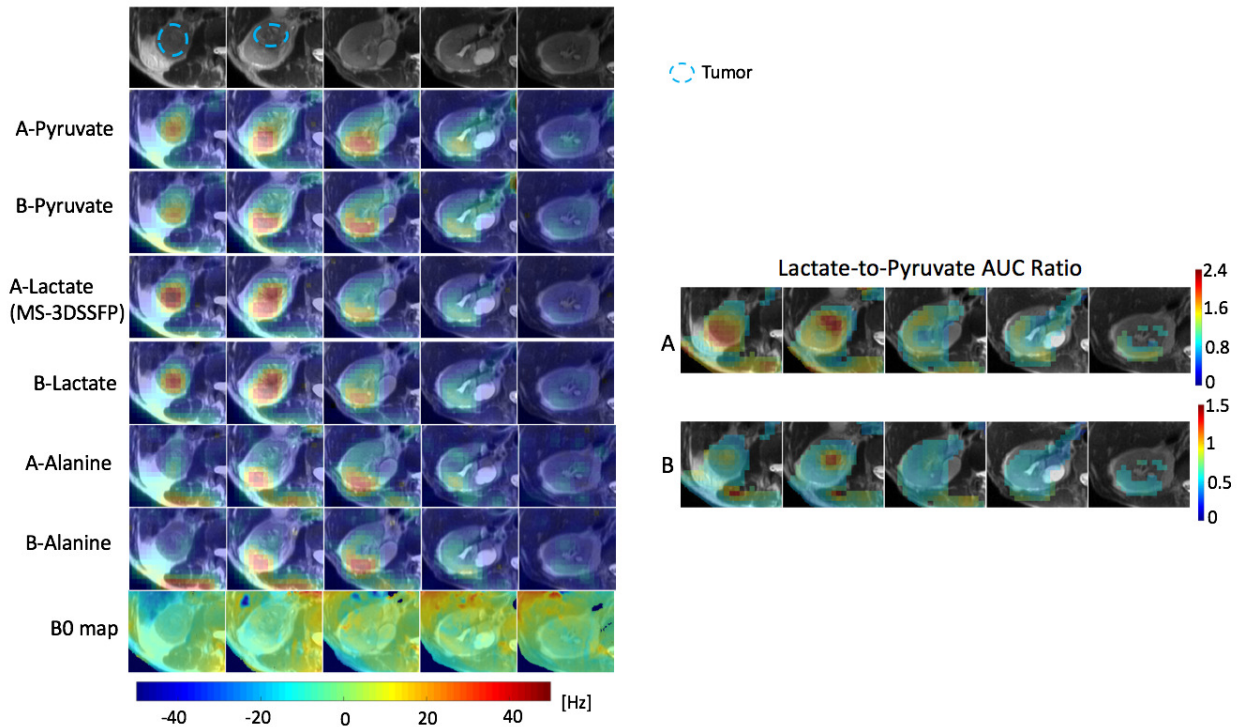
Figure 4.8: Comparison of the MS-3DSSFP sequence with a multi-slice 2D MS-GRE sequence in the kidneys of a patient with a renal tumor with hyperpolarized [1-^{13}C]pyruvate injections using experiment A (pyruvate/alanine: MS-GRE; lactate: MS-3DSSFP) and experiment B (pyruvate/lactate/alanine: MS-GRE). Experiment parameters are described in Table 4.1. AUC images of each metabolite, and lactate-to-pyruvate AUC ratio images and B0 maps are shown. B0 and AUC ratio maps are thresholded the same way as described in Fig. 4.6. B0 maps colorbar is displayed at the bottom.
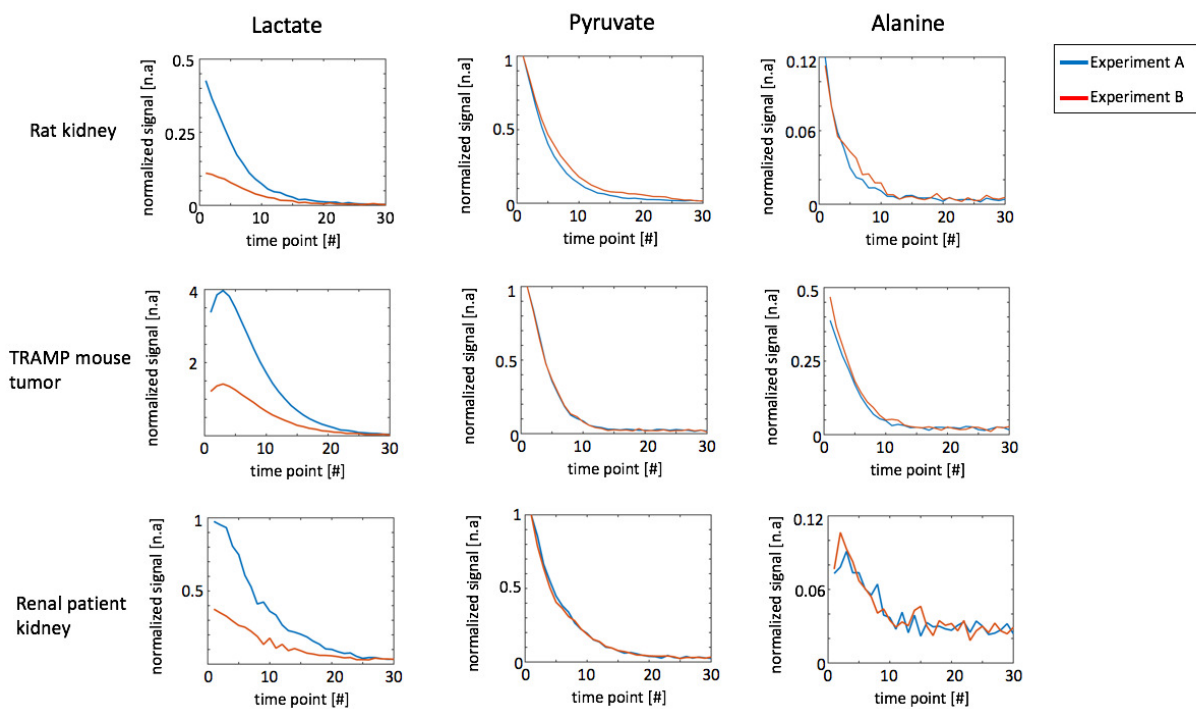
Figure 4.9: Representative dynamic curves of lactate, pyruvate and alanine signals acquired in experiment A (pyruvate/alanine: MS-GRE; lactate: MS-3DSSFP) and experiment B (pyruvate/lactate/alanine: MS-GRE). Experiment parameters are described in Table 4.1. All signals were divided by corresponding noise signals and then divided by the highest value of the pyruvate dynamic curve for normalization. Corresponding dynamic images are shown in Fig. 4.10, Fig. 4.11 and Fig. 4.12.
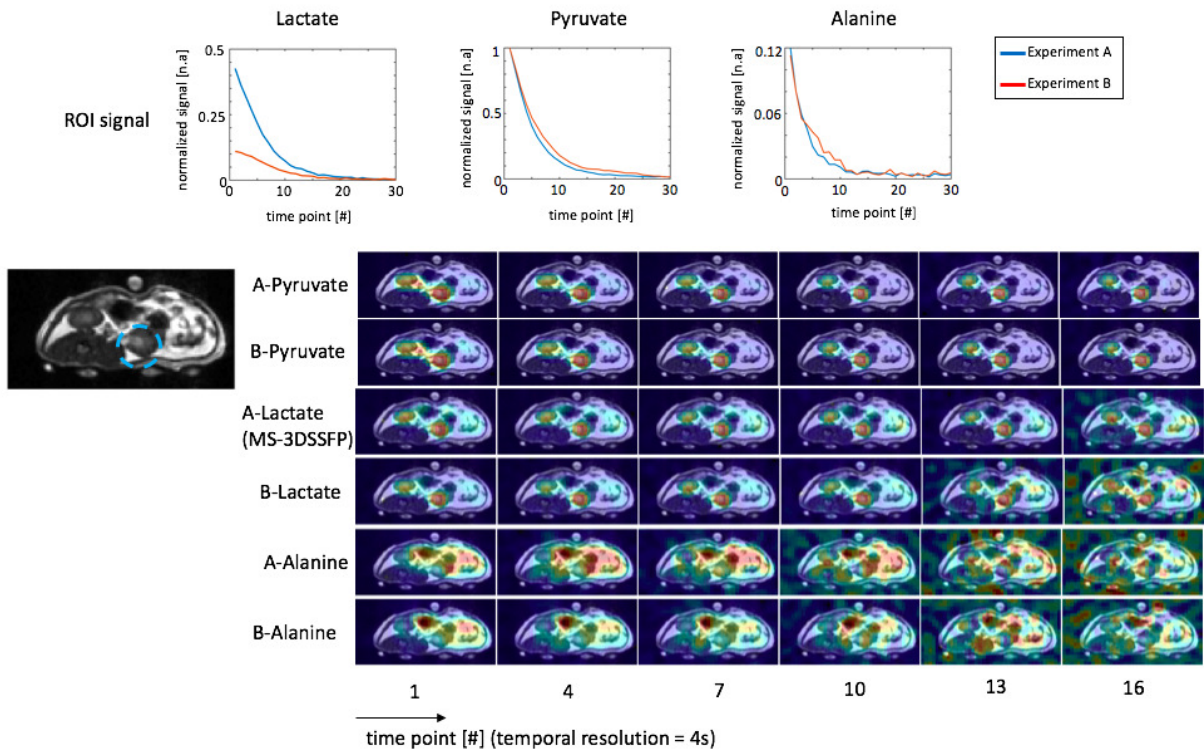
Figure 4.10: Dynamic images and ROI signal curves of a rat kidney slice of the experiments described in Fig. 4.6. Each image is displayed windowed to its own maximum signal to visualize metabolites at all time points. All ROI signals were divided by corresponding noise signals and then divided by the highest value of the pyruvate dynamic curv for normalization.
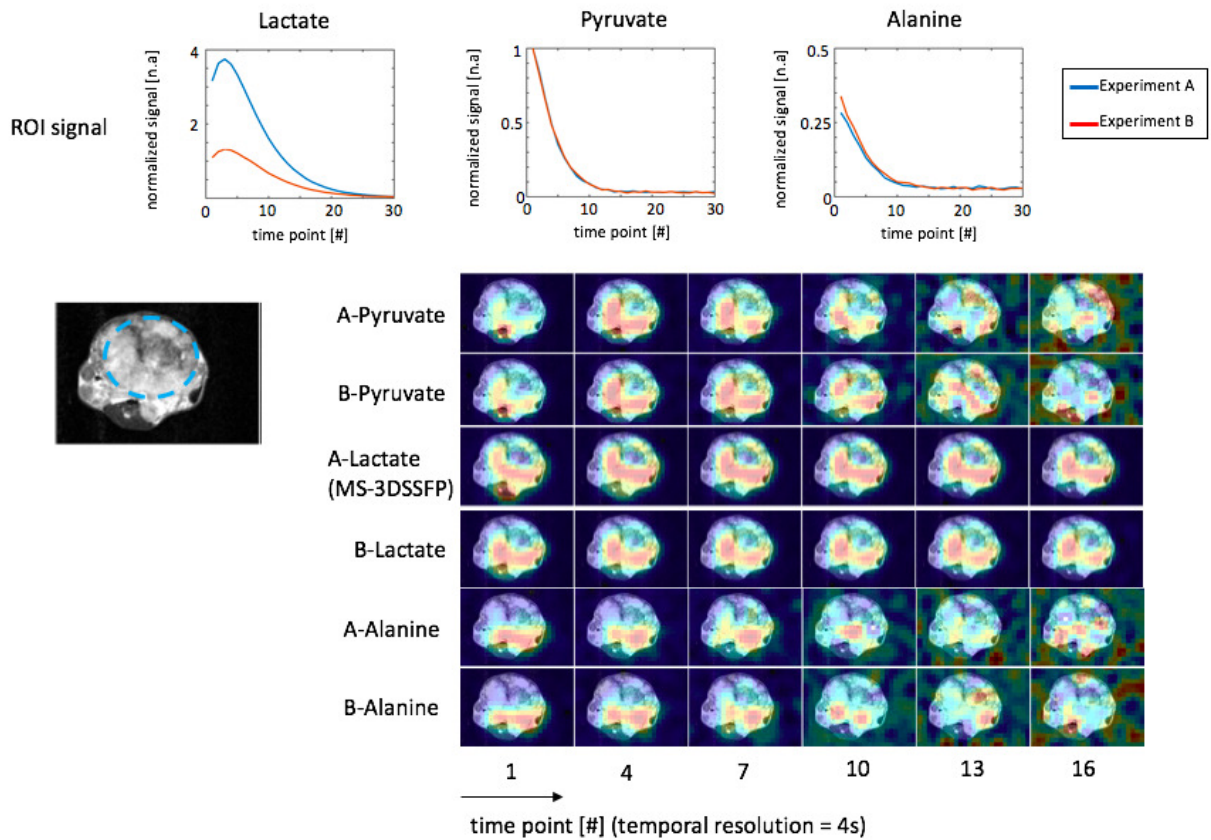
Figure 4.11: Dynamic images and ROI signal curves of a TRAMP mouse tumor slice of the experiments described in Fig. 4.7. Each image is displayed to its own maximum signal to visualize metabolites at all time points. All ROI signals were divided by corresponding noise signals and then divided by the highest value of the pyruvate dynamic curve for normalization.

Figure 4.12: Dynamic images and ROI signal curves of a human renal tumor slice of the experiments described in Fig. 4.8. Each image is displayed to its own maximum signal to visualize metabolites at all time points. All ROI signals were divided by corresponding noise signals and then divided by the highest value of the pyruvate dynamic curve for normalization.
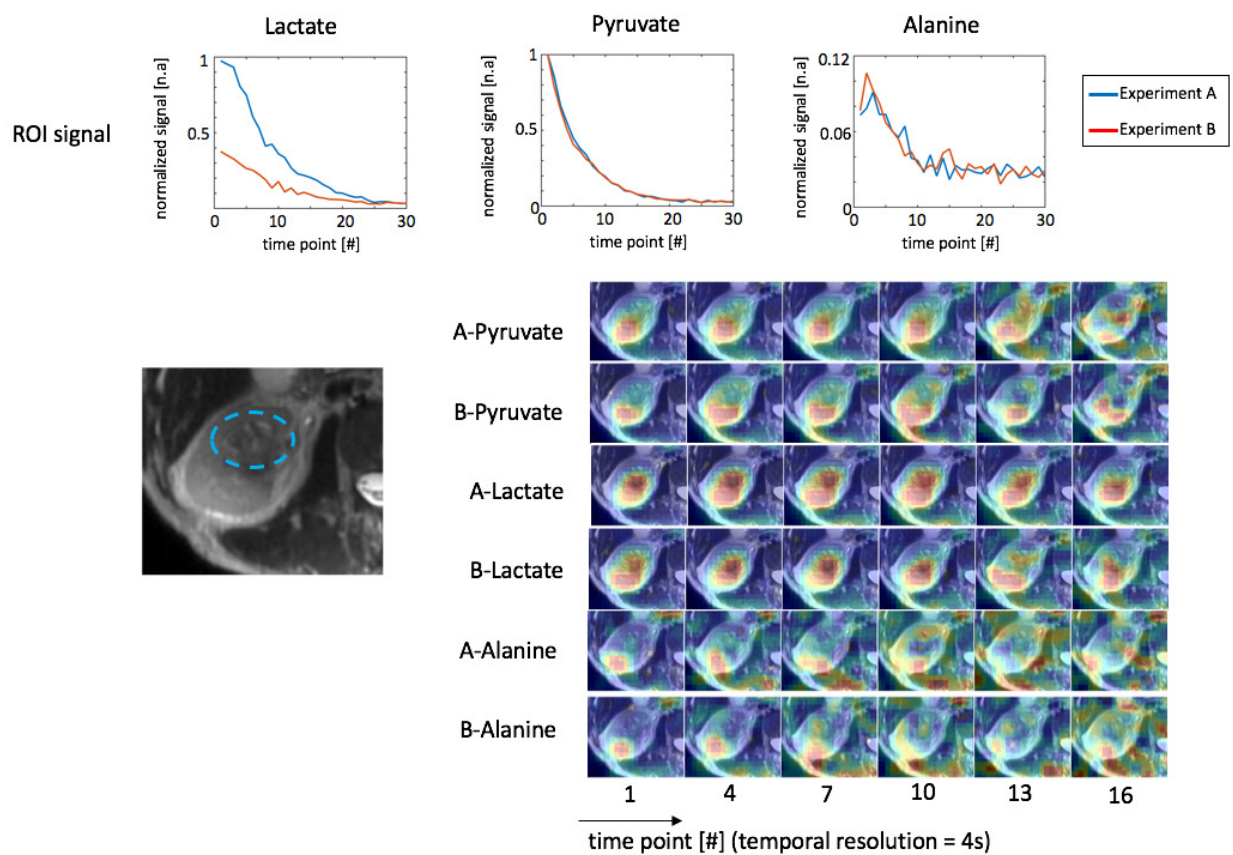
Ratio of metabolite AUC between experiment A and B

	Lactate	Pyruvate	Alanine
Rat kidney	2.54±0.54	0.97±0.10	0.91±0.05
TRAMP Tumor	2.61±0.13	1.00±0.05	0.81±0.09
Human kidney	2.53±0.34	1.01±0.05	1.07±0.09
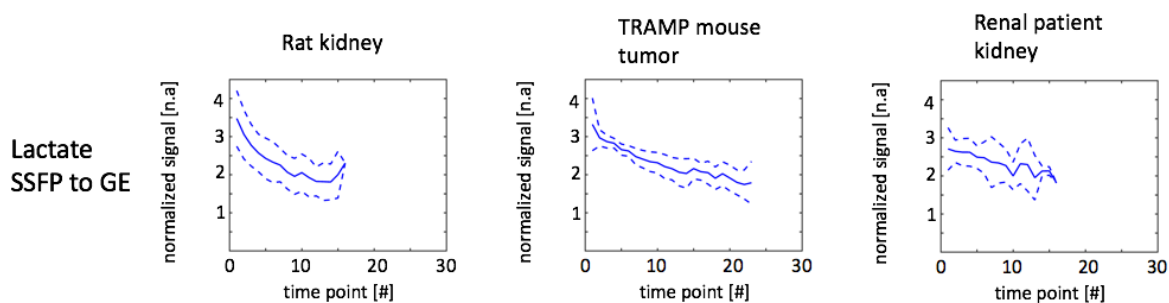
Figure 4.13: Metabolites AUC ratios and lactate ratios of dynamic curves at each time point between experiment A (pyruvate/alanine: MS-GRE; lactate: MS-3DSSFP) and experiment B (pyruvate/lactate/alanine: MS-GRE) at each time point. Experiment parameters are described in Table 4.1. Data from rat kidneys, TRAMP tumors and human kidneys were included in the summary with a criterion of SNR greater than 3. The averaged lactate ratios are shown by the solid lines and ±1 standard deviations are shown by the dashed lines.

Table 4.2: Estimated signal levels of off-resonance metabolites in lactate acquisitions using the MS-3DSSFP sequence. Signal levels are estimated according to Eq. 4.1. A signal level of 1% means that in a MS-3DSSFP lactate acquisition, the ratio between the off-resonance metabolite and lactate is 0.01.

Signal levels of off-resonance metabolites in MS-3DSSFP lactate acquisition

	Alanine (%)	Pyruvate (%)	Pyruvate hydrate (%)
Rat kidney	0.05±0.02	1.14±0.38	3.36±1.11
TRAMP tumor	0.02±0.02	0.08±0.05	0.25±0.15
Human kidney	0.04±0.01	0.52±0.4	1.54±1.18

4.5   Discussion

Metabolite Specific Excitation for bSSFP

We designed a multiband RF pulse (Fig. 4.1) under the constraint of short TR in a bSSFP sequence to achieve spectrally selective excitation on lactate while minimally perturbing other metabolites on a clinical 3T scanner. The 9ms pulse duration was primarily determined by the frequency difference between lactate and pyruvate hydrate (128Hz at 3T) which has the closest frequency to lactate among all compounds in hyperpolarized [1-^{13}C]pyruvate studies. The newly designed RF pulse had a maximum power of 0.2195G and we didn't see specific absorption rates (SAR) issues in our studies.

Our MS-3DSSFP sequence can be easily adapted to image [1-^{13}C]pyruvate or [1-^{13}C]bicarbonate. Because these two metabolites have larger frequency differences from other compounds compared to the frequency difference of lactate to pyruvate hydrate, it is guaranteed to find a solution of metabolite specific excitation pulse for [1-^{13}C]pyruvate or [1-^{13}C]bicarbonate while meeting the TR requirement in our studies. In contrast, it is challenging to design a metabolite specific excitation pulse for imaging alanine, which has a frequency difference of 82Hz (at 3T) to pyruvate hydrate, much closer than the frequency difference between lactate to pyruvate hydrate.

Spiral bSSFP vs Cartesian bSSFP

Spiral readouts were used in the MS-3DSSFP to accelerate the acquisition. All prior HP ^{13}C bSSFP work used Cartesian readouts, which brought challenges to acquire enough data for multiple metabolites in dynamic imaging. For example, whole human brain HP ^{13}C imaging typically uses a matrix size of $16 \times 16 \times 16$ and a FOV of $24 \times 24 \times 24$ cm. Assuming a TR of 15ms, 3D Cartesian readouts need $16 \times 16 \times 15\text{ms} = 3.84\text{s}$ to cover a volume for one metabolite, which would result in insufficient temporal resolution when more than one metabolite needs to be acquired. Given the relatively small matrix size, undersampling strategies will only achieve limited acceleration, therefore fast imaging readouts are preferred[10]. Under the same requirement of matrix size and FOV, stack-of-spiral readouts using two interleaves per stack could achieve an acquisition time of $2 \times 16 \times 15\text{ms} = 0.48\text{ms}$

and an even larger matrix size (24 x 24 x 24), assuming a 3.8ms readout time for each spiral interleaf (same as what we used in this study), a 5 G/cm maximum gradient and a 20 G/cm/ms maximum slew rate.

The center k-space of the spiral readout is not at the center of the TR, which may cause a slight SNR loss compared to Cartesian readouts. Assuming a spiral readout duration of 3.8 ms as used in our studies and a $T2^*$ of 50 ms, the SNR loss of missing the center of the TR will be $1-\exp(-1.9/50) = 4\%$.

MS-3DSSFP vs MS-GRE

By comparing the results of two experiments whose experiment parameters are shown in Table 4.1 (experiment A: MS-3DSSFP for lactate, MS-GRE for pyruvate/alanine; experiment B: MS-GRE for lactate/pyruvate/alanine.), we assessed the performance of the MS-3DSSFP sequence in the aspects of SNR, contrast, banding artifacts, artifacts by exciting undesired metabolites and impact on acquisition of other metabolites. These issues will be discussed in the following paragraphs.

To fairly compare SNR between the MS-3DSSFP sequence and MS-GRE sequences, we used the same spatial resolution, starting time of acquisition, temporal resolution and number of time points. The effective flip angle (see definition in Methods) of the MS-GRE sequence was the same as the flip angle used in the MS-3DSSFP sequence. Readout durations of the two sequences were not matched since $T2^*$ limits the readout duration of a MS-GRE sequence. Compared with MS-GRE sequences, our MS-3DSSFP sequence has shown an overall 2.5-fold SNR improvement (Fig. 4.9 and Fig. 4.13) for dynamic lactate imaging in hyperpolarized [1-^{13}C]pyruvate studies. The SNR improvement ratio would increase with increasing T2 (Fig. 4.14). Besides utilizing T2, other features of the MS-3DSSFP sequence could also contribute to the SNR improvement, including the shorter echo time due to shorter RF pulse and shorter spiral readout time which results in less signal reduction caused by B0 inhomogeneity.

Compared with MS-GRE sequences, the MS-3DSSFP sequence can also provide T2 contrast for tissue characterization. In our studies, such contrast differences are observed in some tumor regions in lactate-to-pyruvate AUC ratio maps as shown in Fig. 4.7 and Fig.
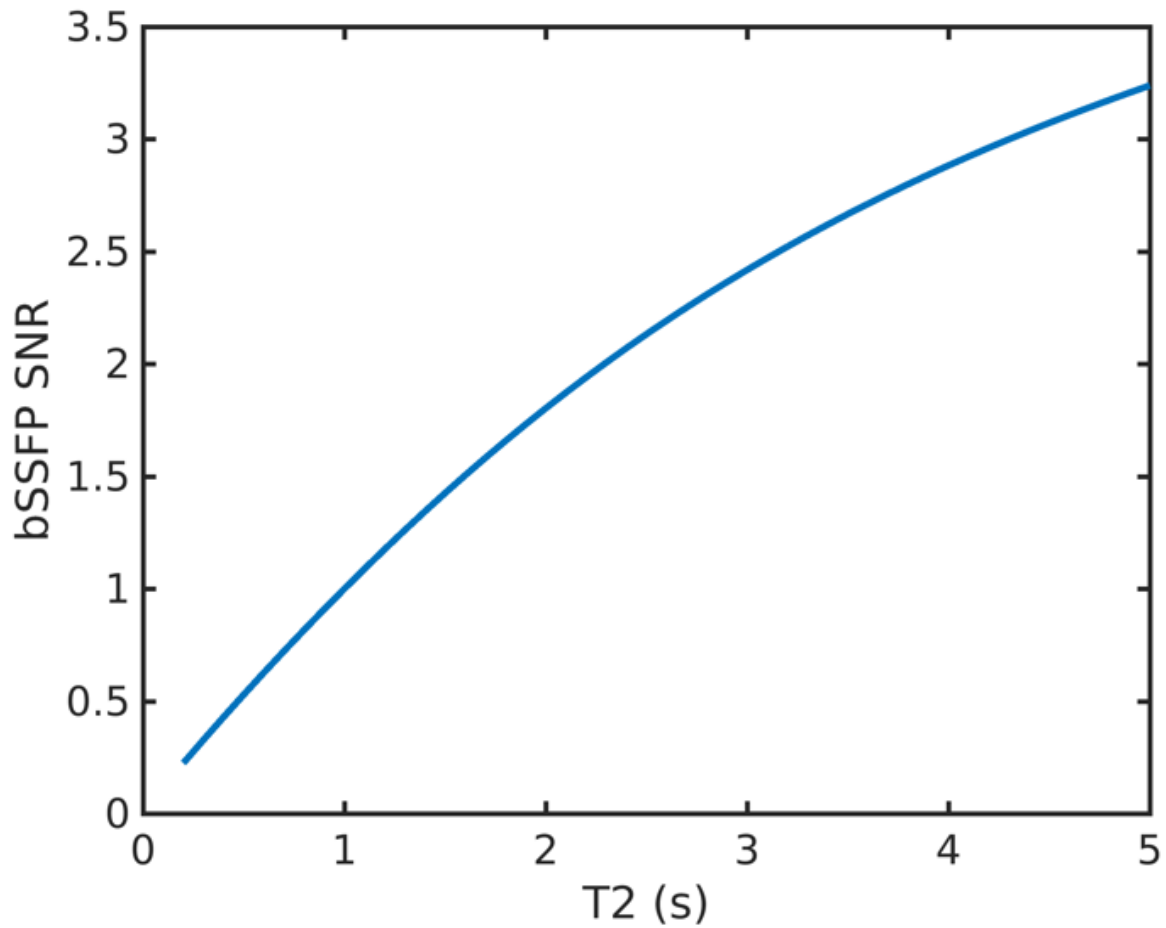
Figure 4.14: Simulation of bSSFP SNR as a function of T2, assuming SNR is 1 when T2 is 1s. Simulation parameters include T1 = 30s, TR 15.3ms, # of time points 30, # of RF pulses 64.

4.8.Parameters of the MS-3DSSFP sequence (e.g. flip angle, TR) could be explored to enable jointly estimating lactate T2 and pyruvate-to-lactate conversion rate.

Excitation profiles of a bSSFP sequence are determined by both the excitation profile of the RF pulse and banding artifacts governed by the chosen TR. Two types of image artifacts could be a result of excitation profiles of a bSSFP sequence: the null-signal banding artifacts of metabolites of interest (in frequency ranges with high flip angles) and artifacts by exciting undesired metabolites (in frequency ranges with low flip angles). Comparing in vivo lactate AUC results (Fig. 4.6, Fig. 4.7, Fig. 4.8) of MS-GRE and MS-3DSSFP, no null-signal banding artifacts are found in the MS-3DSSFP results. In some peripheral regions of TRAMP tumors (Fig. 4.7) where large B0 variations are noted, both MS-GRE and MS-3DSSFP sequences shows hypointense signals in AUC maps of pyruvate and lactate but show hyperintense signals in pyruvate-to-lactate AUC ratio maps. This indicates that both MS-GRE and MS-3DSSFP sequences are sensitive to B0 inhomogeneity although reasons could be different.For MS-3DSSFP, the reason is reduced excitation due to a narrow excitation bandwidth (40Hz). For MS-GRE, reduced excitation could also be a reason although this is expected to be not as bad as MS-3DSSFP, and another reason could be reduced signal due to long spiral readouts (22ms), which can be improved by using proper off-resonance correction [40, 32].

Exciting undesired metabolites would cause both artificially elevated lactate signals and ring-shaped artifacts. Simulation (Fig. 4.2) shows that for the interleaved spiral readouts used in our studies, artifacts from pyruvate hydrate and alanine mostly stay in the center of the point spread function while artifacts from pyruvate, urea and bicarbonate are spread out, which will cause ring-shaped artifacts. No ring-shaped artifacts were observed in the MS-3DSSFP images. Signal levels of undesired metabolites (i.e. pyruvate and alanine) in MS-3DSSFP lactate acquisitions were summarized in Table 4.2. These signal levels could be higher if acquisition starts early when pyruvate and pyruvate hydrate signals are high while lactate signals have yet to build up.

Exciting undesired metabolites would also sacrifice their magnetization and reduce their signals. Comparing AUC results between the two experiments (Fig. 4.13), there is almost no difference in pyruvate and a 5% to 20% difference in alanine AUC. The cost in alanine signals is consistent with the simulation (Fig. 4.3) and phantom (Fig. 4.5) results where

a banding artifact is identified 18Hz upfield from alanine frequency. Therefore, it is more robust to apply our MS-3DSSFP sequence for imaging ROIs with low alanine production such as most tumors, kidney or brain.

Interleaving Different Sequences In One Injection

In hyperpolarized ^{13}C studies, signals of different metabolites are usually acquired using the same sequence so that results reveal the contrast of metabolite concentration. In our studies, we developed a method of imaging different metabolites using different sequences in one injection, i.e., imaging lactate using MS-3DSSFP while imaging pyruvate and alanine using MS-GRE. This method is achieved by using commercial software (RTHawk, HeartVista, Los Altos, CA) where interleaving different sequences are allowed. It could potentially provide multiple contrasts for multiple metabolites in a single injection, whereas the same purpose could possibly be achieved by using a MR-Fingerprinting type of acquisition[29].

Precautions of Performing MS-3DSSFP Experiments

To run the MS-3DSSFP sequence, several issues need to be carefully handled. As discussed before, the RF pulse used in the MS-3DSSFP sequence has a narrow bandwidth (40Hz) and real-time frequency calibration [55] is crucial to the robustness of this sequence. Furthermore, the multiband RF pulse used in this study does not avoid exciting urea, therefore, it is suggested to remove urea phantom which was typically used in pre-scan frequency and power calibration, otherwise there could be spiral off-resonance artifacts from urea signals. Finally, the multiband RF pulse was not slice-selective, therefore the field of view along the slice direction needs to be as large as the extent of ^{13}C receive coils.

4.6   Conclusion

This work described a novel 3D bSSFP sequence that integrates a lactate specific excitation pulse and stack-of-spiral readouts for improved lactate dynamic imaging in hyperpolarized [1-^{13}C]pyruvate studies on a clinical 3T scanner. Compared with MS-GRE sequences, the MS-3DSSFP sequence showed an overall 2.5X SNR improvement for lactate imaging in rat

kidneys, tumors of TRAMP mice and human kidneys. Future work will include exploring joint estimation of lactate T2 and pyruvate-to-lactate conversion rate, extending the applications of the proposed sequence for imaging regions with acceptable B0 homogeneity such as human brain, as well as imaging other metabolites (e.g. pyruvate, bicarbonate) in hyperpolarized [1-^{13}C]pyruvate studies.

Chapter 5

Metabolite Specific Multi Spin-Echo Sequences for Hyperpolarized ^{13}C MRI

5.1   Introduction

The long T2 relaxation time of ^{13}C-labeled metabolites at clinical field strengths (e.g. lactate T2 $\sim$0.5s-2s at 3T[63, 44, 34]) allows for efficient use of hyperpolarized signal by sampling data at repetitively refocused spin echoes. Besides bSSFP sequences as discussed in the previous chapter, sequences with fast spin echo (FSE) type of acquisitions[58] have been also explored to improve the efficient use of hyperpolarized signal. Different from bSSFP sequences where refocusing pulses could use arbitrary flip angle and net gradient areas are always zero between two neighboring refocusing pulses, FSE sequences use a pair of identical crusher gradients applied before and after each refocusing pulse typically with a flip angle of 180°. Compared with bSSFP sequences, FSE sequences are substantially less sensitive to B0 inhomogeneity, and have no constraint of short TR which allows a longer RF excitation pulse to achieve a better metabolite specific excitation. Refocusing pulses of FSE sequences can be either a Shinnar-Le Roux (SLR) pulse or an adiabatic inversion pulse. Compared with SLR pulses, adiabatic refocusing pulses are B1 insensitive above the adiabatic threshold, which is crucial for hyperpolarized ^{13}C studies since any unnecessary excitation would cause loss

of nonrenewable hyperpolarization. The disadvantages of adiabatic refocusing pulse are the requirement of high RF power which is more likely to hit the specific absorption rate (SAR) limit.

This chapter presents two metabolite specific multi spin-echo sequences where adiabatic refocusing pulse and Shinnar-Le Roux (SLR) refocusing pulses were used respectively. In the work using SLR refocusing pulses, varied crusher gradients were used to reduce the loss of longitudinal hyperpolarized ^{13}C magnetization.

5.2 A Metabolite Specific Multi Spin-Echo 2D Sequence with Adiabatic Refocusing Pulse for Hyperpolarized ^{13}C MRI

This work presents a metabolite specific multi spin-echo sequence using adiabatic refocusing pulse for improved SNR in hyperpolarized ^{13}C imaging.

5.2.1 Methods

The proposed sequence (Fig. 5.1) consists of a single-band spectral-spatial (SPSP) pulse, a spiral readout right after the excitation, and spiral in/out readouts at each spin echo formed by a single adiabatic pulse.

The SPSP RF pulse[16] used in this study was designed to excite [1-^{13}C]pyruvate and [1-^{13}C]lactate alternatively at 3T, with a passband of 120Hz and a stopband of 600Hz. The design of adiabatic pulses (Fig. 5.2) was the same as the prior work[6], with stopband ripples of <0.2% and a refocused bandwidth of ∼1.4kHz to refocus all metabolites in [1-^{13}C]pyruvate studies. At each spin echo, spiral-in and out readouts were used to improve the TR efficiency. Spiral readouts are used to maximize spatial coverage. The spiral-in gradient waveform was obtained by time reversing and negating the spiral-out waveforms [13]. Both gradient echoes and spin echoes are acquired in the same excitation to maximize the use of transverse magnetization and also allow direct comparison between gradient echo acquisitions and multi spin-echo acquisitions.
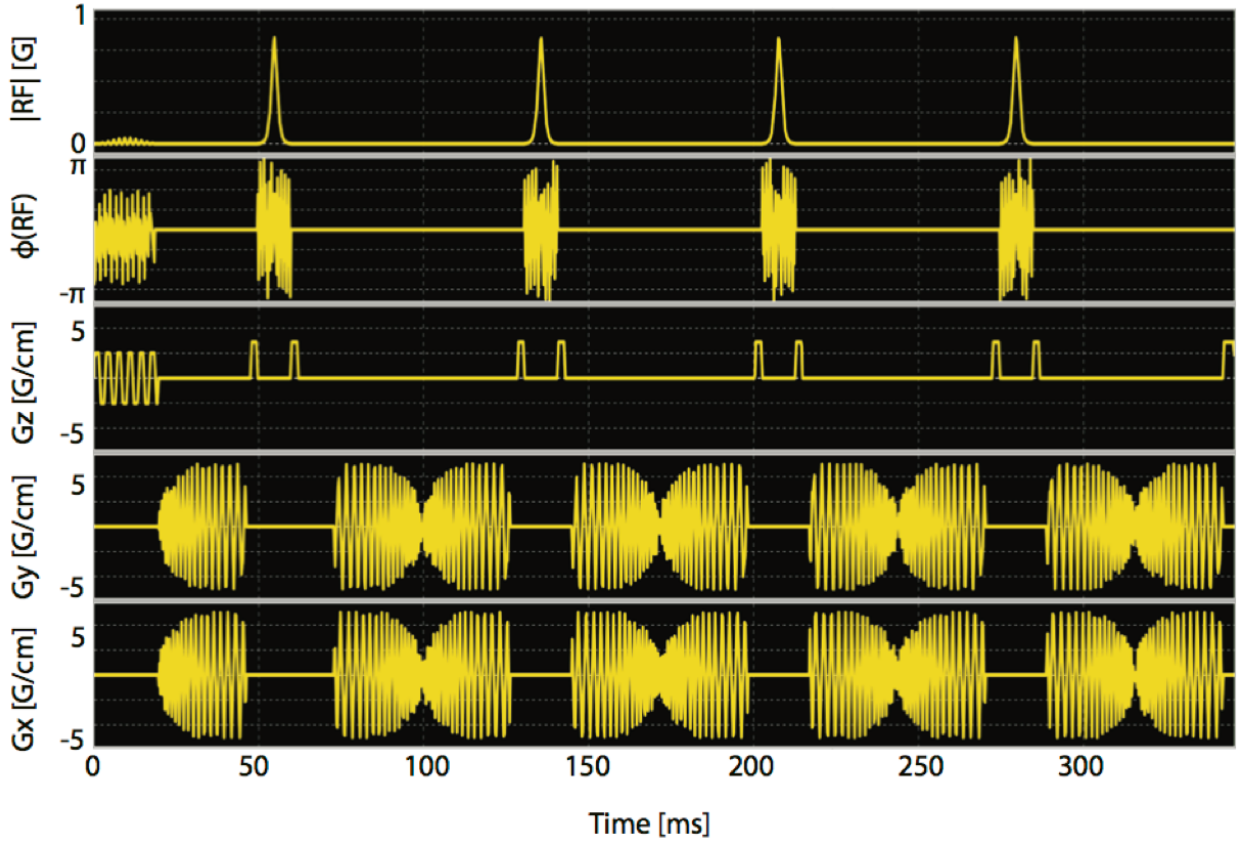
Figure 5.1: Overview of the proposed sequence which includes a single-band spectral-spatial excitation pulse (passband FWHM 120Hz), a spiral readout (25ms) and spiral in/out readouts at each spin echo formed by a single adiabatic pulse (see Fig. 5.2). Four spin echoes are used in this study.

In prior spin-echo ^{13}C sequences, adiabatic pulses[6, 24] were always played out in pairs to refocus the quadratic phase[5]. In this work, we analyzed the phase of refocusing using an adiabatic pulse in response to frequency and RF power. We noticed that over a short range of frequencies (Fig. 5.3a) and RF power (Fig. 5.3b), the variation of Mxy phase is small enough to preserve sufficient signals. For example, reduction of Mxy amplitude is negligible when averaged over a frequency range of $\pm$10Hz and about 17% averaged over a RF power range of $\pm$5%. Within a spatial resolution ($\sim$ 1cm) for ^{13}C imaging, variations of frequency and RF power are typically smaller than 10Hz and 5% respectively, thus sufficient signals should be preserved at the spin echoes formed by a single adiabatic pulse.
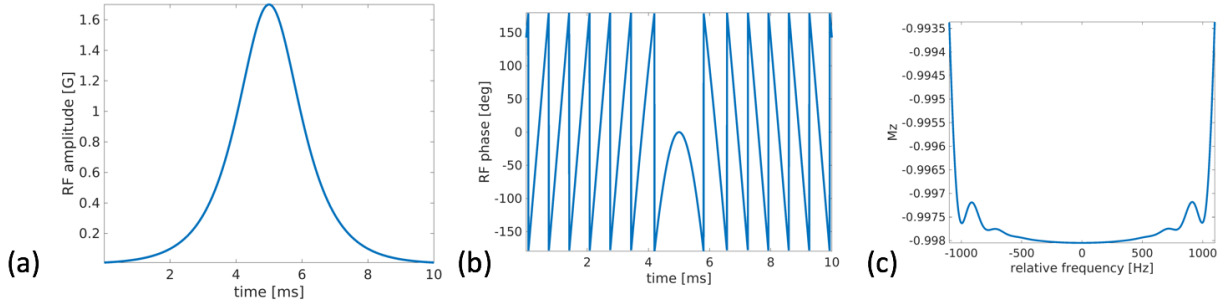
Figure 5.2: Amplitude (a) and phase (b) of adiabatic pulse used in this study (10ms, peak B1 1.7G, refocusing bandwidth ∼1.4kHz, stopband ripple <0.2%). Inversion profile of this adiabatic pulse is simulated in graph (c).

The proposed sequence for dynamic hyperpolarized ^{13}C imaging was tested in vivo using normal Sprague-Dawley rats with $^{13}C/^1H$ birdcage coils on a clinical GE 3T scanner. DNP experiments used a HyperSense polarizer and 80mM [1-^{13}C] pyruvate was injected. Two experiments were performed with dynamic pyruvate and lactate imaging on rat kidneys, where the first experiment acquired lactate data using the proposed sequence with one gradient echo (GE) and four spin-echoes (SE) (nominal TE 80ms, 152ms, 244ms and 316ms) and the second experiment only used the first spiral readout without any adiabatic pulses or spin echo readouts. For both experiments, pyruvate signals were acquired using a single gradient-echo spiral readout. Other experiment parameters included injection time 10s, FA$_{pyr}$ 10, FA$_{lac}$ 40, TR$_{pyr}$ 2s, TR$_{lac}$ 2s, slice thickness 2cm, FOV 8 × 8cm, in-plane resolution 2.5 × 2.5 mm, 30 time frames for each metabolites. Bolus tracking and real-time B1 calibration [55] using pyruvate signals from the left kidney were added prior to this acquisition to trigger the sequence upon the bolus peak and achieve accurate center frequency and B1 power in real time.

5.2.2   Results

Fig. 5.4 shows the results of two hyperpolarized [1-^{13}C]pyruvate experiments on rat kidneys (experiment 1: pyruvate GE, lactate GE + SE; experiment 2: pyruvate GE, lactate GE).
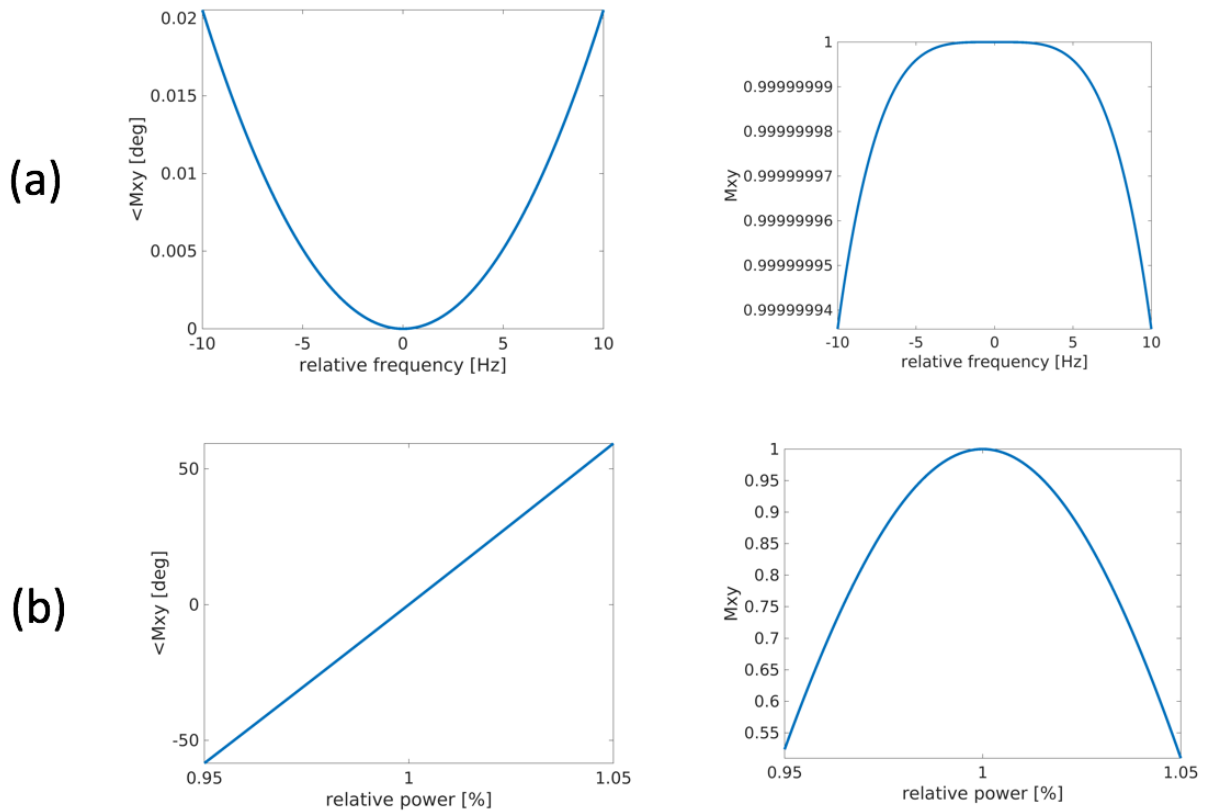
Figure 5.3: Simulation of phase and corresponding transverse amplitude generated by a single adiabatic pulse over a range of frequency (a) and power (b)with initial magnetizations pointing to positive x axis. The mean magnetization amplitude over a range of 20Hz is about 1. Mean amplitude over a range of $\pm 5\%$ is about 0.83.

The results are magnitude images normalized by the noise standard deviation. Images of experiment 2 were then rescaled to compensate for any polarization differences by equalizing the peak pyruvate SNR of the left kidney to that in experiment 1.

As shown in Fig. 5.4a, a reasonable amount of SNR ($\sim 50\%$ as the gradient echo) was left at the fourth spin-echo (nominal TE 316ms). Combined lactate images (Fig. 5.4a-b, Fig. 5.4e) were found to achieve higher SNR compared to GE-only images, with an improvement as much as 2 fold at a single time frame. The combination of one GE and four SE images had greater SNR than one GE for 30 s (15 acquisitions with a 2s temporal resolution).
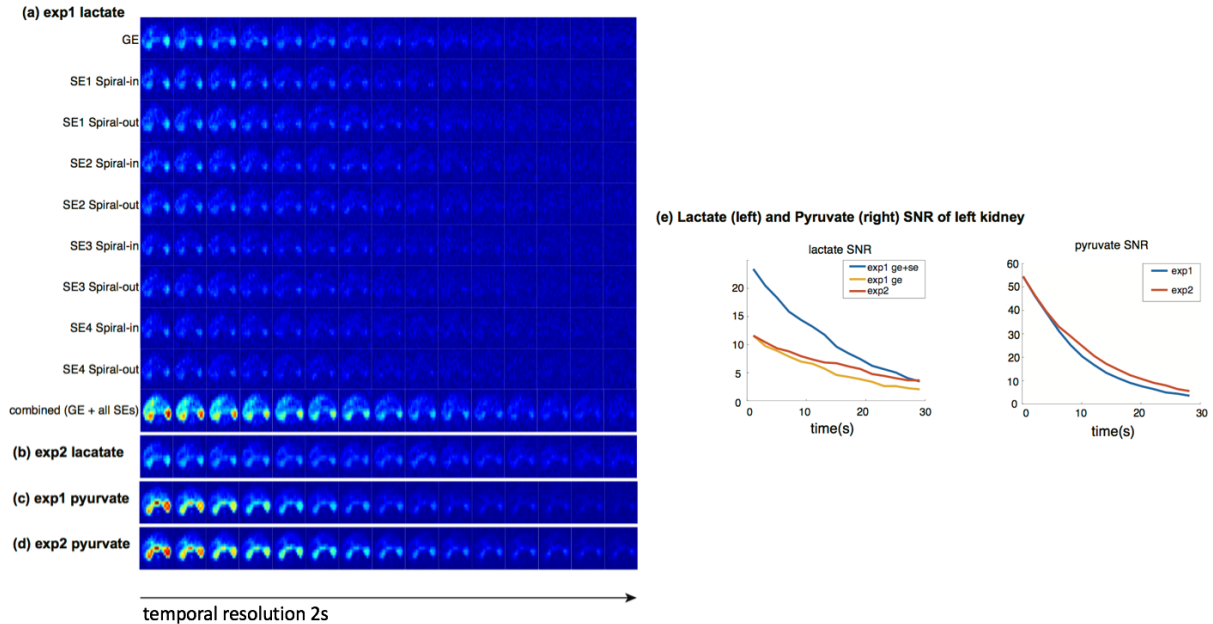
Figure 5.4: Results of two hyperpolarized [1-^{13}C]pyruvate experiments in a normal rat using the sequence scheme shown in Fig. 5.1. (a-d) Pyruvate and lactate images over 15 acquisitions (temporal resolution = 2s). All images were normalized by their noise standard deviation. Images of experiment 2 were also rescaled by equalizing its highest SNR with that of experiment 1 to compensate for polarization difference between the two experiments. Combination of gradient echo and all spin echoes data was performed by summing complex images, after correcting the phase mismatch between the gradient echo, the odd and even spin echoes. (e) Lactate and pyruvate SNR dynamics of left kidney, showing as much as 2-fold increase in lactate SNR when combining the gradient echo and all spin echoes.

A faster apparent decay rate was found in the pyruvate and lactate GE signals (Fig. 5.4e) in experiment 1. This could be possibly attributed to polarization saturation by adiabatic pulses at the coil boundary where the adiabatic condition is not satisfied. Even with this potentially partial saturation of magnetization at the coil boundaries, the proposed SE method was still advantageous for imaging downstream metabolites (e.g. lactate) of pyruvate because it provides greater SNR.

5.2.3 Discussion

This work demonstrates improved SNR for hyperpolarized ^{13}C imaging using a metabolite specific multi spin-echo sequence with data acquisition at each spin echo formed by a single adiabatic pulse. Since the image phases are different between odd echoes and even echoes, such phase differences need to be compensated for before combining images at different echoes. When extending this sequence to 3D acquisitions, phase encoding at odd echoes and even echoes need to be grouped together separately for accurate reconstructions.

Timing is critical for the proposed sequence since power near the coil boundaries will go below the adiabatic threshold and thus saturates inflowing spins in these regions. In this study, the acquisition was prescribed to start at bolus peak to minimize saturating injected bolus while ensuring most of injected bolus arriving at the imaging ROI. Spiral readouts used in this study could be replaced with an echo-planar imaging trajectory which has less spatial coverage but more robust to gradient imperfection.

Because the resulting phase of a single adiabatic pulse is sensitive to RF power and frequency, moving spins that experience spatial B0 or B1 inhomogeneity during the refocusing pulse train will have incomplete spin refocusing at even echoes and result in unwanted phase accrual at later echoes. Therefore, it's more robust to apply the proposed sequence for imaging the static organs such as brain.

Extending the proposed sequence to clinical studies requires an adiabatic pulse with low RF power. We were able to design an adiabatic pulse with maximum B1 of 0.4G (Fig. 5.5), stopband ripples of <1% and a bandwidth of 680Hz which is still able to refocus all metabolites in [1-^{13}C]pyruvate studies. We replaced the spiral in/out readouts with EPI readouts and removed the first gradient echo acquisitions. On the same clinical 3T scanner, the specific absorption rate (SAR) limit was reached when more than 16 adiabatic pulses were used per 3.5s. Therefore, there is a limit for the number of adiabatic pulses being used in a multi spin-echo sequences in clinical studies.

5.2.4 Conclusion

This work demonstrates an approach that incorporates multi spin echo acquisitions with spiral in/out trajectories into dynamic hyperpolarized ^{13}C MRI. The proposed method was
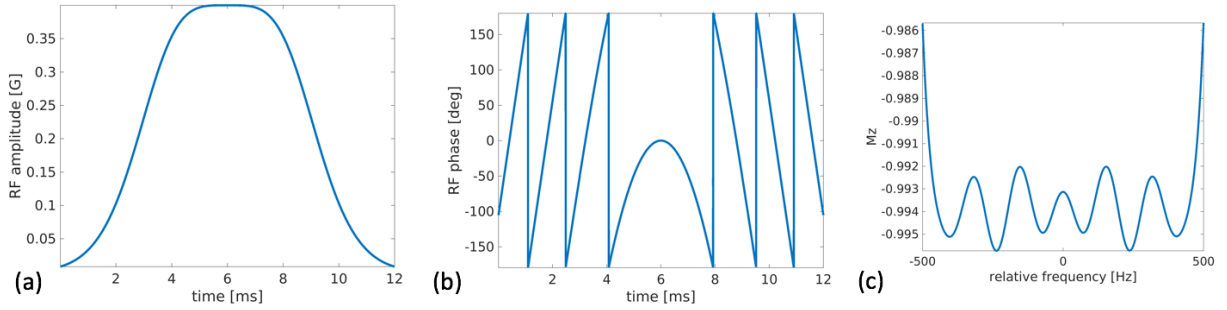
(a) (b) (c)

Figure 5.5: Amplitude (a) and phase (b) of adiabatic pulse proposed for clinical study (12ms, peak B1 0.4G, refocusing bandwidth ∼680Hz, stopband ripple <1%). Inversion profile of this adiabatic pulse is simulated in graph (c).

found to achieve higher SNR over 15 dynamic acquisitions with a 2s temporal resolution. Extending this method for clinical studies is challenging due to SAR limits. Future work will focus on reducing the power of the adiabatic pulse.

5.3 A Metabolite Specific Non-CPMG Multi Spin-Echo Sequence for Hyperpolarized ^{13}C MRI

This work presents a metabolite specific GRASE sequence with Shinnar-Le Roux (SLR) refocusing pulses. Varied crusher gradients were investigated to reduce the loss of longitudinal hyperpolarized ^{13}C magnetization. This sequence met the clinical scanner limits and we demonstrated the feasibility of applying this sequence for a brain hyperpolarized ^{13}C MRI study.

5.3.1 Methods

The proposed GRASE sequence (Fig. 5.6a) was implemented on the RTHawk system (HeartVista, CA). A spectral spatial RF pulse[16] was used for excitation, followed by a train of spectrally selective refocusing pulse (TBW 4.5, pulse duration 14ms) and EPI readouts. The refocusing pulse is designed to minimally perturb pyruvate signal while refocusing
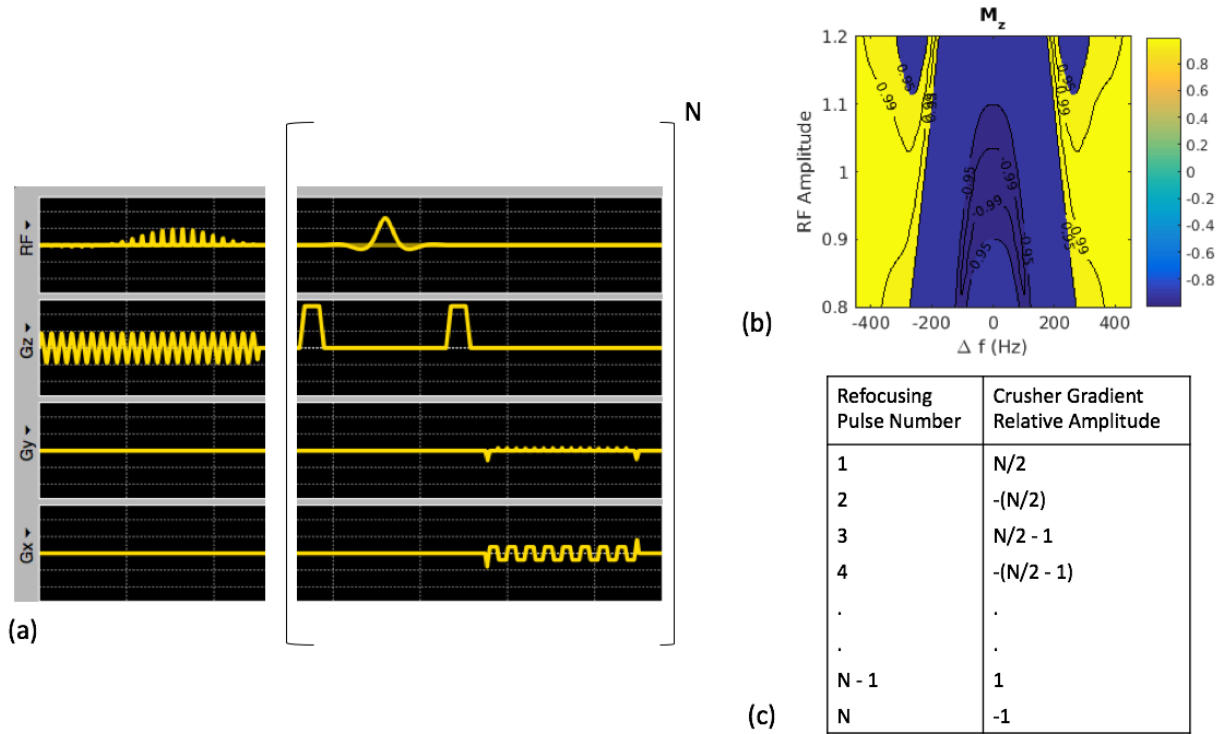
Figure 5.6: Pulse sequence waveforms for the GRASE sequence (a). A spectral spatial pulse[16] was used for excitation, followed by a train of spectrally selective SLR (TBW 4.5, pulse duration 14ms, peak B1 0.3219G) refocusing pulse and symmetric EPI readouts. Graph (b) shows the Mz profile of the refocusing pulse. A pair of crusher gradients was placed before and after each refocusing pulse. Graph (c) demonstrates the varied crusher gradients[42] used in this study.

lactate (Fig. 5.6b). A pair of crusher gradients was placed before and after each refocusing pulse. Fig. 5.6c shows a varied crusher scheme[42], which has been used to eliminate the stimulated echo pathway in the proton FSE sequences to improve the accuracy of T2 quantification. In this study, we explored to eliminate stimulated echoes using this varied crusher gradients to eliminate stimulated echoes in order to preserve the hyperpolarized longitudinal magnetization.

Our studies were performed on a clinical GE 3T scanner. To compare constant crushers with varied crushers, phantom experiments were performed with an enriched $[^{13}C]$ NaHCO3 phantom (T2 $\sim$1s, T1 $\sim$20s). For each crusher scheme, 2D acquisitions were performed using
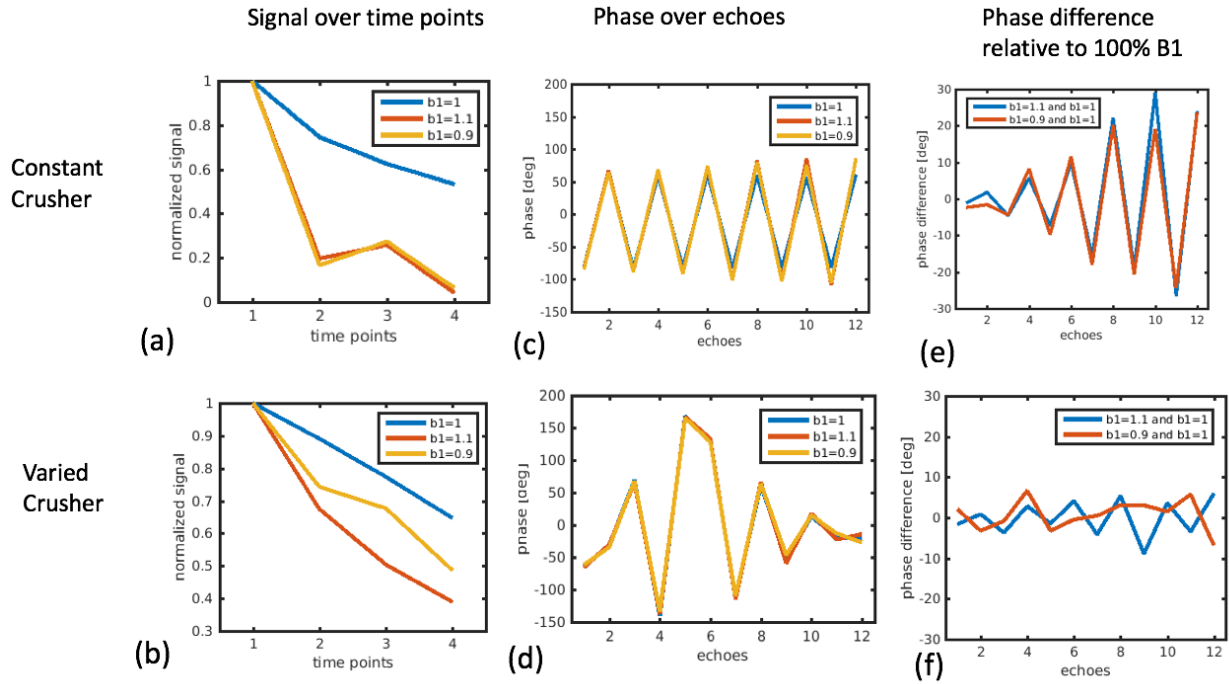
Figure 5.7: Comparison of phantom results between GRASE sequences using constant crusher and varied crusher schemes. For each crusher scheme, 2D GRASE was performed for four time points with a 30° flip angle. The same experiment was repeated at relative RF powers of 90% ("b1=0.9"), 100%("b1=1") and 110%("b1=1.1"), respectively. Phantom magnitudes of the first echo were plotted over time points (a-b). Phantom phases at each echo were plotted in (c-d). The difference of phantom phases between using 100% RF power and other RF powers were plotted for each echo in (e-f).

the proposed GRASE (1s TR, 12 echoes) for four time points with a 30° flip angle. The same experiment was repeated at a relative RF power of 90%, 100% and 110%, respectively.

Two hyperpolarized ^{13}C experiments were performed on a tumor-bearing mouse with the injection of [1-^{13}C]pyruvate pre-polarized in a HyperSense DNP system. Each time point has one 3D stack-of-EPI gradient-echo pyruvate acquisition and one single-shot 3D lactate acquisition using the proposed GRASE (12 echoes). Constant and varied crushers were used in the first and second experiment, respectively. At the end of the second experiment, lactate signals were acquired without z phase encoding to measure the signal phase, which was used for phase correction in 3D reconstruction. Scan parameters were: 3s temporal resolution,
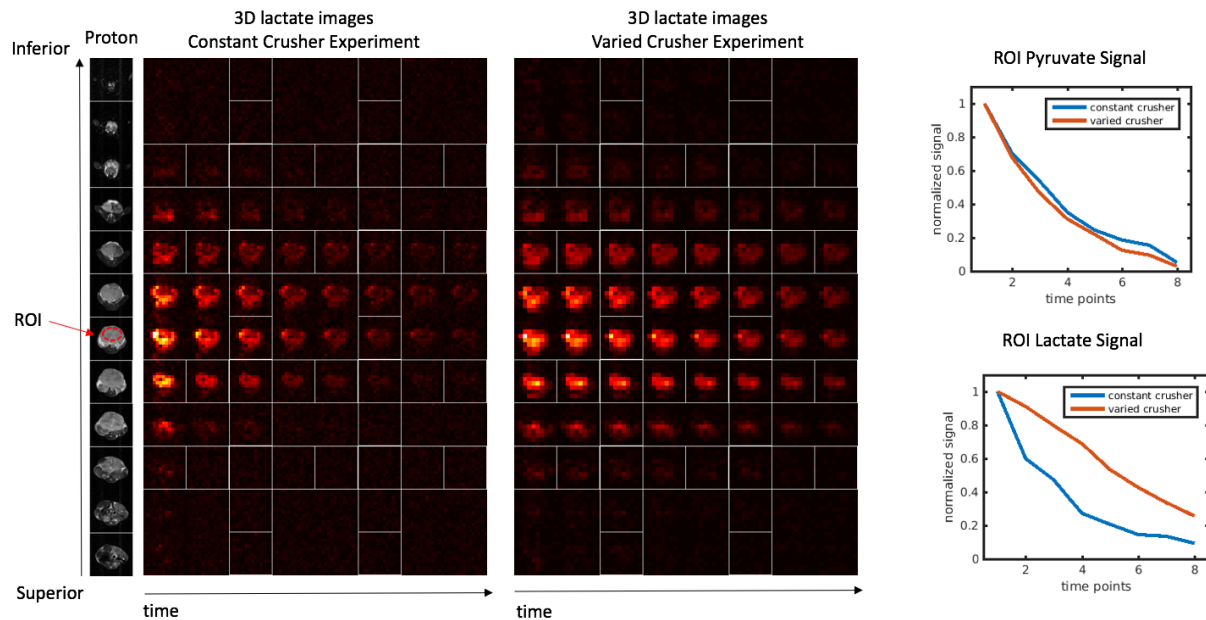
Figure 5.8: Results of 3D lactate images acquired using the proposed GRASE sequence with constant crusher or varied crusher schemes. Pyruvate signals were acquired using a 3D gradient echo sequence. ROI pyruvate signals and ROI lactate signals of the two experiments were plotted over time points, and normalized to the signal at the first timepoint to account for differences in polarization.

$14{\times}14{\times}12$ matrix size, 24mm excitation slab, 6° and 30° flip angle for pyruvate and lactate, respectively, $3{\times}3{\times}4$mm and $4{\times}4{\times}4$mm resolution for the first and second experiment, respectively.

To demonstrate the feasibility of applying the proposed sequence in clinical studies, a human brain study was performed with an injection of hyperpolarized $[1\text{-}^{13}C]$pyruvate prepared using a SPINlab polarized and methods described in a prior study[55]. Each time point had one 2D gradient-echo pyruvate acquisition and one multiecho lactate acquisition using the proposed GRASE (12 echoes) with varied crushers. Scan parameters were: $1.5{\times}1.5{\times}2$cm resolution, $24{\times}24$cm FOV, 3s temporal resolution, 20° and 30° flip angle for pyruvate and lactate, respectively.

All experiments were triggered at bolus peak within the tissue of interest for real-time frequency and B1 calibration[55].

5.3.2 Results

Results of phantom studies are shown in Fig. 5.7. Faster signal decay is observed in experiments using constant crushers (Fig. 5.7a) compared to using varied crushers (Fig. 5.7b), indicating that eliminating stimulated echo path with varied crushers could reduce the loss of the longitudinal magnetization. When RF power changes, varied crushers (Fig. 5.7f) showed more stable phase over echoes than constant crushers (Fig. 5.7e). The robustness of phase over echoes to RF power changes is necessary for applying phase encoding over echoes when imaging inhomogeneous transmit B1 regions.

Results of animal studies using constant or varied crushers are shown in Fig. 5.8. 3D lactate images of both experiments matches with the anatomical details and the 24mm excitation slab which corresponded to 6 slices. As expected, similar decay rates are found between gradient-echo pyruvate signals of the two experiments. A faster decay rate of lactate signals was found in the experiment using a constant crusher gradient, which agrees with phantom results discussed above.

Fig. 5.9 shows the dynamic ^{13}C images of pyruvate, lactate and bicarbonate in the human study. Combining images of echoes shows an improved SNR compared to a single-echo image. Fig 5.10 shows lactate and bicarbonate T2 results in the human study. Bicarbonate T2 values were predominantly about 500ms, while lactate T2 was substantially longer, with half of lactate T2 values greater than 1000ms. The fitting examples in Fig. 5.10 demonstrate the goodness of T2 fitting. Although the duration of the spin-echo train (440ms) of 12 echoes is relatively short compared to the fitted T2 values (500-1500ms), our results still provide a preliminary estimate of ^{13}C lactate and bicarbonate T2 values in the human brain.

5.3.3 Discussion

In this work, we demonstrated using varied crusher gradients in fast spin echo sequences to eliminate stimulated echo pathways and thus preserve nonrecoverable hyperpolarized magnetization. The same purpose could be possibly achieved by varied RF phases [46] over TRs. Compared to varied RF phases, varied gradient amplitudes used in our study are more sensitive to eddy currents and limited by maximum gradient capabilities. However, varied RF phases takes seven echoes [46] for the preparation and thus nonrenewable hyperpolarized
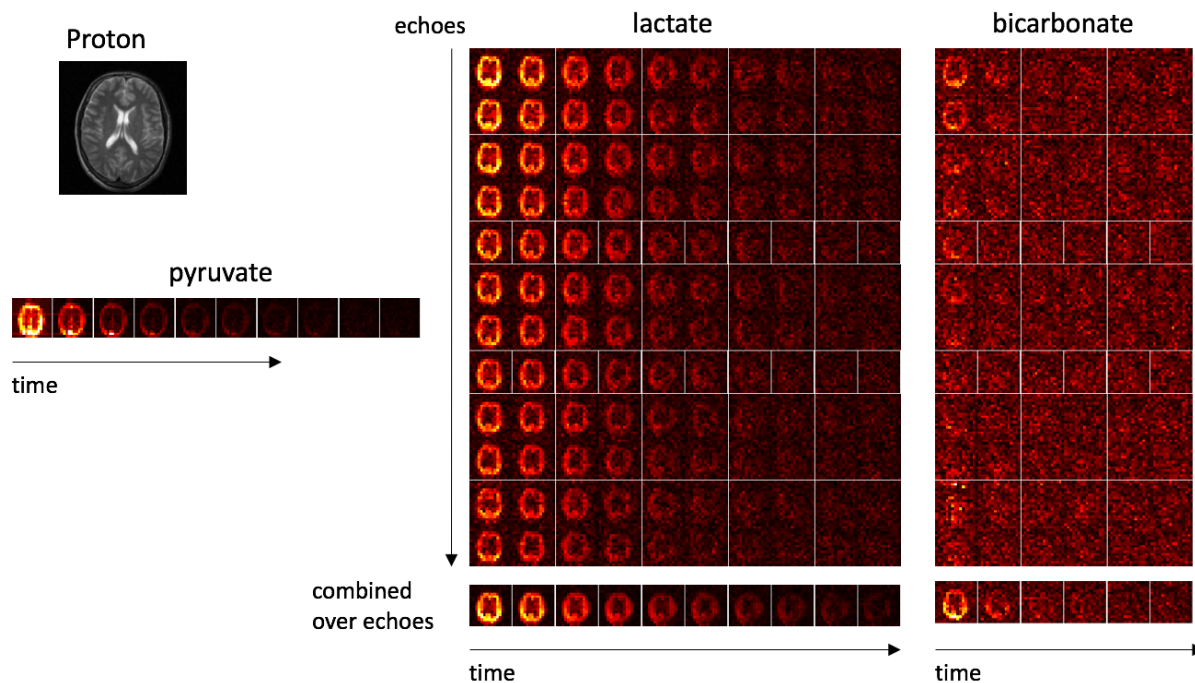
Figure 5.9: Results of 2D lactate and bicarbonate images acquired using the proposed GRASE sequence with varied crusher. Images combined over echoes are also shown. 2D Pyruvate images were acquired with a gradient echo sequence.

signals are lost due to T2 decay over the preparation period.

Although FSE using varied crusher gradients showed better robustness to B1 inhomogeneity compared to constant crusher gradients, there is still about a 25% acceleration in loss of the longitudinal magnetization with B1 errors of 10%. This is due to the nature of SLR refocusing pulses, which are sensitive to B1. Therefore, it is recommended to apply the proposed sequence when the transmit B1 field is homogeneous, e.g., with a birdcage coil. Large excitation flip angles are also recommended for use at the peak dynamic signal of the metabolites to reduce the loss of longitudinal magnetization caused by imperfect B1. Bolus tracking and real-time power calibration [55] can be used to monitor peak signal of metabolites and accurately calibrate power.
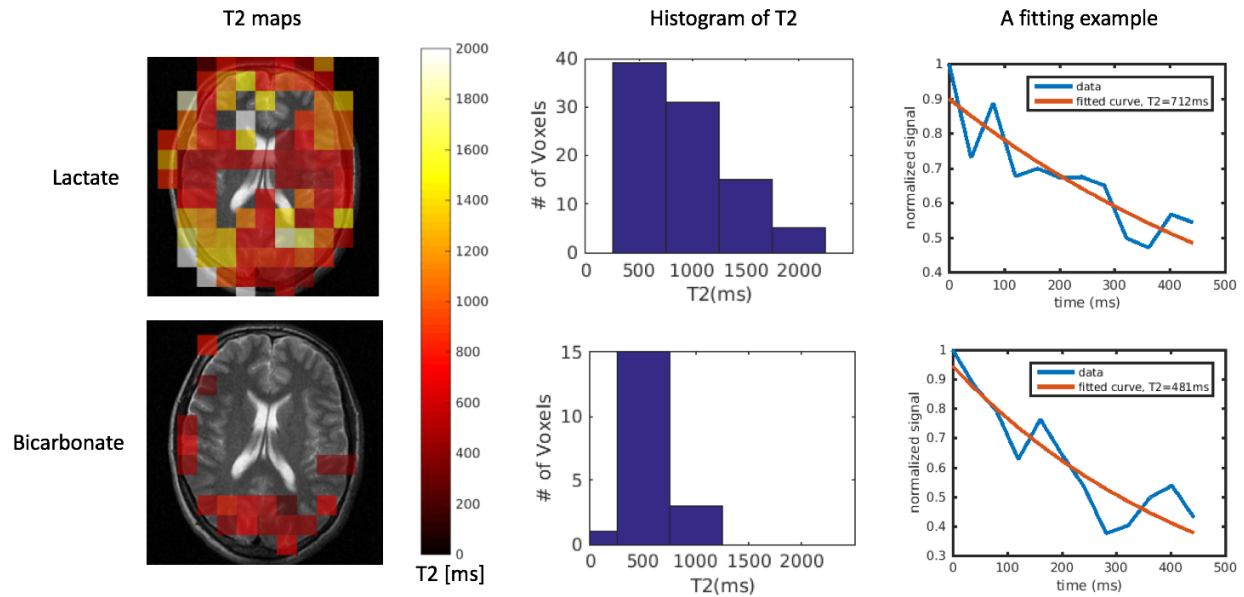
Figure 5.10: Results of lactate and bicarbonate T2 maps which were fitted using images of the first time point shown in Fig. 5.9. Histograms of the measured T2 value are presented. One voxel fitting example is shown for lactate and bicarbonate T2 maps, respectively.

5.3.4 Conclusion

A metabolite specific GRASE sequence using SLR refocusing pulses and varied crusher gradients was developed for dynamic hyperpolarized ^{13}C Imaging and demonstrated the feasibility for use in human brain research. Compared to constant crusher gradients, varied crusher gradients reduced the signal loss of the longitudinal magnetization. Signals of multiple echoes can either be used to encode a 3D volume, or to increase SNR or estimate T2 as a 2D multi-echo approach shown in this work. Future work will focus on optimizing the refocusing pulses and understanding the phase evolution over echoes in the varied crushers scheme.

Bibliography

[1] Jan H Ardenkjaer-Larsen. "Hyperpolarized MR - What's up Doc?" In: *J Magn Reson* 306 (2019), pp. 124–127. DOI: `10.1016/j.jmr.2019.07.017`.

[2] Jan H Ardenkjær-Larsen et al. "Increase of signal-to-noise of more than 10,000 times in liquid state NMR". In: *Discov Med* 3.19 (2003), pp. 37–9.

[3] Matt A Bernstein, Kevin F King, and Xiaohong Joe Zhou. *Handbook of MRI Pulse Sequences*. 2004.

[4] Hsin-Yu Chen et al. "Assessing Prostate Cancer Aggressiveness with Hyperpolarized Dual-Agent 3D Dynamic Imaging of Metabolism and Perfusion". In: *Cancer Res* 77.12 (2017), pp. 3207–16. DOI: `10.1158/0008-5472.CAN-16-2083`.

[5] Steven Conolly, Dwight Nishimura, and Albert Macovski. "A selective adiabatic spin-echo pulse". In: *Journal of Magnetic Resonance (1969)* 83.2 (1989), pp. 324 –334. ISSN: 0022-2364. DOI: `https://doi.org/10.1016/0022-2364(89)90194-7`. URL: `http://www.sciencedirect.com/science/article/pii/0022236489901947`.

[6] Charles H. Cunningham et al. "Double spin-echo sequence for rapid spectroscopic imaging of hyperpolarized 13C". In: *Journal of Magnetic Resonance* 187.2 (2007), pp. 357–362. ISSN: 10907807. DOI: `10.1016/j.jmr.2007.05.014`.

[7] Charles H Cunningham et al. "Pulse sequence for dynamic volumetric imaging of hyperpolarized metabolic products". In: *J Magn Reson* 193.1 (2008), pp. 139–46. DOI: `10.1016/j.jmr.2008.03.012`.

[8] Sam E Day et al. "Detecting tumor response to treatment using hyperpolarized 13C magnetic resonance imaging and spectroscopy". In: *Nat Med* 13.11 (2007), pp. 1382–7. DOI: `10.1038/nm1650`.

[9]   Markus Durst et al. "Bolus tracking for improved metabolic imaging of hyperpolarised compounds". In: *J Magn Reson* 243 (2014), pp. 40–6. DOI: `10.1016/j.jmr.2014.02.011`.

[10]   Markus Durst et al. "Comparison of acquisition schemes for hyperpolarised ^{13}C imaging". In: *NMR Biomed* 28.6 (2015), pp. 715–25. DOI: `10.1002/nbm.3301`.

[11]   T K Foo et al. "Automated detection of bolus arrival and initiation of data acquisition in fast, three-dimensional, gadolinium-enhanced MR angiography". In: *Radiology* 203.1 (1997), pp. 275–80. DOI: `10.1148/radiology.203.1.9122407`.

[12]   R J Gillies et al. "Causes and effects of heterogeneous perfusion in tumors". In: *Neoplasia* 1.3 (1999), pp. 197–207.

[13]   G H Glover and C S Law. "Spiral-in/out BOLD fMRI for increased SNR and reduced susceptibility artifacts". In: *Magn Reson Med* 46.3 (2001), pp. 515–22.

[14]   Klaes Golman, René in 't Zandt, and Mikkel Thaning. "Real-time metabolic imaging". In: *Proc Natl Acad Sci U S A* 103.30 (2006), pp. 11270–5. DOI: `10.1073/pnas.0601319103`.

[15]   Jeremy W. Gordon, Daniel B. Vigneron, and Peder E. Z. Larson. "Development of a symmetric echo planar imaging framework for clinical translation of rapid dynamic hyperpolarized ^{13}C imaging". In: *Magnetic Resonance in Medicine* 00 (2016), n/a–n/a. ISSN: 07403194. DOI: `10.1002/mrm.26123`. URL: `http://doi.wiley.com/10.1002/mrm.26123`.

[16]   Jeremy W Gordon et al. "3D hyperpolarized C-13 EPI with calibrationless parallel imaging". In: *J Magn Reson* 289 (2018), pp. 92–99. DOI: `10.1016/j.jmr.2018.02.011`.

[17]   H Gudbjartsson and S Patz. "The Rician distribution of noisy MRI data". In: *Magn Reson Med* 34.6 (1995), pp. 910–4.

[18]   Caroline Guglielmetti et al. "In vivo metabolic imaging of Traumatic Brain Injury". In: *Sci Rep* 7.1 (Dec. 2017), p. 17525. DOI: `10.1038/s41598-017-17758-4`.

[19]   Crystal Harrison et al. "Comparison of kinetic models for analysis of pyruvate-to-lactate exchange by hyperpolarized ^{13}C NMR". In: *NMR Biomed* 25.11 (2012), pp. 1286–94. ISSN: 09523480. DOI: `10.1002/nbm.2801`.

[20] J I Jackson et al. "Selection of a convolution function for Fourier inversion using gridding [computerised tomography application]". In: *IEEE Trans Med Imaging* 10.3 (1991), pp. 473–8. DOI: 10.1109/42.97598.

[21] John Kurhanewicz et al. "Analysis of cancer metabolism by imaging hyperpolarized nuclei: prospects for translation to clinical research". In: *Neoplasia* 13.2 (2011), pp. 81–97.

[22] John Kurhanewicz et al. "Hyperpolarized 13C MRI: Path to Clinical Translation in Oncology". In: *Neoplasia* 21.1 (Jan. 2019), pp. 1–16. DOI: 10.1016/j.neo.2018.09.006.

[23] Peder E Z Larson et al. "Fast dynamic 3D MR spectroscopic imaging with compressed sensing and multiband excitation pulses for hyperpolarized 13C studies". In: *Magn Reson Med* 65.3 (2011), pp. 610–9. DOI: 10.1002/mrm.22650.

[24] Peder E. Z. Larson et al. "Investigation of tumor hyperpolarized [1- **13** C]-pyruvate dynamics using time-resolved multiband RF excitation echo-planar MRSI". In: *Magnetic Resonance in Medicine* 63.3 (2010), pp. 582–591. ISSN: 07403194. DOI: 10.1002/mrm.22264. URL: http://doi.wiley.com/10.1002/mrm.22264.

[25] Angus Z. Lau, Albert P. Chen, and Charles H. Cunningham. "Integrated Bloch-Siegert B1 mapping and multislice imaging of hyperpolarized ^{13}C pyruvate and bicarbonate in the heart". In: *Magn Reson Med* 67.1 (2012), pp. 62–71. ISSN: 07403194. DOI: 10.1002/mrm.22977.

[26] Angus Z Lau et al. "Spectral-spatial excitation for rapid imaging of DNP compounds". In: *NMR Biomed* 24.8 (2011), pp. 988–96. DOI: 10.1002/nbm.1743.

[27] Christoffer Laustsen et al. "Assessment of early diabetic renal changes with hyperpolarized [1-(13) C]pyruvate". In: *Diabetes Metab Res Rev* 29.2 (2013), pp. 125–9. DOI: 10.1002/dmrr.2370.

[28] Jochen Leupold et al. "Fast multiecho balanced SSFP metabolite mapping of 1H and hyperpolarized 13C compounds". In: *Magnetic Resonance Materials in Physics, Biology and Medicine* 22.4 (2009), pp. 251–256. ISSN: 1352-8661. DOI: 10.1007/s10334-009-0169-z. URL: http://dx.doi.org/10.1007/s10334-009-0169-z.

[29] Dan Ma et al. "Magnetic resonance fingerprinting". In: *Nature* 495.7440 (2013), pp. 187–192. ISSN: 0028-0836. DOI: `10.1038/nature11971`. URL: `http://www.nature.com/nature/journal/v495/n7440/full/nature11971.html$\backslash$nhttp://www.nature.com/nature/journal/v495/n7440/pdf/nature11971.pdf`.

[30] John D MacKenzie et al. "Detection of inflammatory arthritis by using hyperpolarized 13C-pyruvate with MR imaging and spectroscopy". In: *Radiology* 259.2 (2011), pp. 414–20. DOI: `10.1148/radiol.10101921`.

[31] John Maidens et al. "Optimizing flip angles for metabolic rate estimation in hyperpolarized carbon-13 MRI". In: *IEEE Trans Med Imaging* 35.11 (Nov. 2016), pp. 2403–12. DOI: `10.1109/TMI.2016.2574240`.

[32] L C Man, J M Pauly, and A Macovski. "Improved automatic off-resonance correction without a field map in spiral imaging". In: *Magn Reson Med* 37.6 (1997), pp. 906–13.

[33] Azma Mareyam et al. "31-Channel brain array for hyperpolarized ^{13}C imaging at 3T". In: *Proc. Intl. Soc. Mag. Reson. Med. 25* (2017), p. 1225.

[34] Eugene Milshteyn et al. "Development of high resolution 3D hyperpolarized carbon-13 MR molecular imaging techniques". In: *Magn Reson Imaging* 38 (May 2017), pp. 152–162. DOI: `10.1016/j.mri.2017.01.003`.

[35] Eugene Milshteyn et al. "High spatiotemporal resolution bSSFP imaging of hyperpolarized [1-13 C]pyruvate and [1-13 C]lactate with spectral suppression of alanine and pyruvate-hydrate". In: *Magn Reson Med* 80.3 (Sept. 2018), pp. 1048–1060. DOI: `10.1002/mrm.27104`.

[36] Cornelius von Morze et al. "Frequency-specific SSFP for hyperpolarized ^{13}C metabolic imaging at 14.1 T". In: *Magn Reson Imaging* 31.2 (2013), pp. 163–70. DOI: `10.1016/j.mri.2012.06.037`.

[37] Kaz Nagashima. "Optimum pulse flip angles for multi-scan acquisition of hyperpolarized NMR and MRI". In: *J Magn Reson* 190.2 (2008), pp. 183–8. DOI: `10.1016/j.jmr.2007.10.011`.

[38] Sarah J Nelson et al. "Metabolic imaging of patients with prostate cancer using hyper-polarized [1-^{13}C]pyruvate". In: *Sci Transl Med* 5.198 (2013), 198ra108. DOI: `10.1126/scitranslmed.3006070`.

[39] Dwight Nishimura. *Principles of Magnetic Resonance Imaging*. 2010.

[40] D C Noll et al. "Deblurring for non-2D Fourier transform magnetic resonance imaging". In: *Magn Reson Med* 25.2 (1992), pp. 319–33.

[41] Yeshayau Pocker et al. "Reversible hydration of pyruvic acid. I. Equilibrium studies". In: *The Journal of Physical Chemistry* 73.9 (1969), pp. 2879–2882. DOI: `10.1021/j100843a015`. eprint: `https://doi.org/10.1021/j100843a015`. URL: `https://doi.org/10.1021/j100843a015`.

[42] Colin S. Poon and R. Mark Henkelman. "Practical T2 quantitation for clinical applications". In: *Journal of Magnetic Resonance Imaging* 2.5 (1992), pp. 541–553. DOI: `10.1002/jmri.1880020512`. eprint: `https://onlinelibrary.wiley.com/doi/pdf/10.1002/jmri.1880020512`. URL: `https://onlinelibrary.wiley.com/doi/abs/10.1002/jmri.1880020512`.

[43] Galen D Reed et al. "High resolution (13)C MRI with hyperpolarized urea: in vivo T(2) mapping and (15)N labeling effects". In: *IEEE Trans Med Imaging* 33.2 (2014), pp. 362–71. DOI: `10.1109/TMI.2013.2285120`.

[44] Galen D Reed et al. "Imaging Renal Urea Handling in Rats at Millimeter Resolution using Hyperpolarized Magnetic Resonance Relaxometry". In: *Tomography* 2.2 (2016), pp. 125–135. DOI: `10.18383/j.tom.2016.00127`.

[45] Scott B Reeder et al. "Least-squares chemical shift separation for (13)C metabolic imaging". In: *J Magn Reson Imaging* 26.4 (2007), pp. 1145–52. DOI: `10.1002/jmri.21089`.

[46] Patrick Le Roux. "Non-CPMG Fast Spin Echo with Full Signal". In: *Journal of Magnetic Resonance* 155.2 (2002), pp. 278 –292. ISSN: 1090-7807. DOI: `https://doi.org/10.1006/jmre.2002.2523`. URL: `http://www.sciencedirect.com/science/article/pii/S1090780702925231`.

[47] Laura I Sacolick et al. "B1 mapping by Bloch-Siegert shift". In: *Magn Reson Med* 63.5 (2010), pp. 1315–22. DOI: `10.1002/mrm.22357`.

[48] M. A. Schroeder. "In vivo assessment of pyruvate dehydrogenase flux in the heart using hyperpolarized carbon-13 magnetic resonance". In: *Proc Natl Acad Sci U S A* 105 (2008). DOI: `10.1073/pnas.0805953105`. URL: `https://doi.org/10.1073/pnas.0805953105`.

[49] Rolf F Schulte and Florian Wiesinger. "Direct design of 2D RF pulses using matrix inversion." In: *Journal of magnetic resonance (San Diego, Calif. : 1997)* 235 (2013), pp. 115–20. ISSN: 1096-0856. DOI: `10.1016/j.jmr.2013.07.014`. URL: `http://www.ncbi.nlm.nih.gov/pubmed/24013595`.

[50] Rolf F Schulte et al. "Transmit gain calibration for nonproton MR using the Bloch-Siegert shift". In: *NMR Biomed* 24.9 (2011), pp. 1068–72. DOI: `10.1002/nbm.1657`.

[51] Hong Shang et al. "Multiband RF pulses with improved performance via convex optimization". In: *Journal of Magnetic Resonance* 262 (2016), pp. 81 –90. ISSN: 1090-7807. DOI: `https://doi.org/10.1016/j.jmr.2015.11.010`. URL: `http://www.sciencedirect.com/science/article/pii/S1090780715002980`.

[52] Hong Shang et al. "Spectrally selective three-dimensional dynamic balanced steady-state free precession for hyperpolarized C-13 metabolic imaging with spectrally selective radiofrequency pulses". In: *Magn Reson Med* 78.3 (Sept. 2017), pp. 963–975. DOI: `10.1002/mrm.26480`.

[53] Chang-Yu Sun et al. "Influence of parameter accuracy on pharmacokinetic analysis of hyperpolarized pyruvate". In: *Magn Reson Med* 79 (2018), pp. 3239–48. DOI: `10.1002/mrm.26992`.

[54] J. Svensson. "Hyperpolarized 13C MR angiography using trueFISP". In: *Magn Reson Med* 50 (2003). DOI: `10.1002/mrm.10530`. URL: `https://doi.org/10.1002/mrm.10530`.

[55] Shuyu Tang et al. "A regional bolus tracking and real-time B1 calibration method for hyperpolarized 13 C MRI". In: *Magn Reson Med* 81.2 (Feb. 2019), pp. 839–851. DOI: `10.1002/mrm.27391`.

[56] D.P Towers, T.R Judge, and P.J Bryanston-Cross. "Automatic interferogram analysis techniques applied to quasi-heterodyne holography and ESPI". In: *Opt Lasers Eng* 14.4 (1991), pp. 239–81. ISSN: 0143-8166. DOI: https://doi.org/10.1016/0143-8166(91)90052-U. URL: http://www.sciencedirect.com/science/article/pii/014381669190052U.

[57] James Tropp et al. "Multi-channel metabolic imaging, with SENSE reconstruction, of hyperpolarized [1-(13)C] pyruvate in a live rat at 3.0 tesla on a clinical MR scanner". In: *J Magn Reson* 208.1 (2011), pp. 171–7. DOI: 10.1016/j.jmr.2010.10.007.

[58] Jiazheng Wang et al. "Single shot three-dimensional pulse sequence for hyperpolarized 13 C MRI". In: *Magn Reson Med* 77.2 (Feb. 2017), pp. 740–752. DOI: 10.1002/mrm.26168.

[59] Florian Wiesinger et al. "IDEAL spiral CSI for dynamic metabolic MR imaging of hyperpolarized [1- 13C]pyruvate". In: *Magnetic Resonance in Medicine* 68.1 (2012), pp. 8–16. ISSN: 07403194. DOI: 10.1002/mrm.23212.

[60] David M Wilson et al. "Multi-compound polarization by DNP allows simultaneous assessment of multiple enzymatic activities in vivo". In: *J Magn Reson* 205.1 (2010), pp. 141–7. DOI: 10.1016/j.jmr.2010.04.012.

[61] Yan Xing et al. "Optimal variable flip angle schemes for dynamic acquisition of exchanging hyperpolarized substrates". In: *J Magn Reson* 234 (2013), pp. 75–81. DOI: 10.1016/j.jmr.2013.06.003.

[62] Y-F Yen et al. "Imaging considerations for in vivo ^{13}C metabolic mapping using hyperpolarized ^{13}C-pyruvate". In: *Magn Reson Med* 62.1 (2009), pp. 1–10. DOI: 10.1002/mrm.21987.

[63] Yi-Fen Yen et al. "T2 relaxation times of ^{13}C metabolites in a rat hepatocellular carcinoma model measured in vivo using ^{13}C-MRS of hyperpolarized [1-^{13}C]pyruvate". In: *NMR Biomed* 23.4 (2010), pp. 414–23. DOI: 10.1002/nbm.1481.

[64] L Zhao et al. "Gradient-echo imaging considerations for hyperpolarized ^{129}Xe MR". In: *J Magn Reson B* 113 (1996), pp. 179–83.

[65] Zihan Zhu et al. "Coil combination methods for multi-channel hyperpolarized 13C imaging data from human studies". In: *J Magn Reson* 301 (2019), pp. 73–79. DOI: 10.1016/j.jmr.2019.01.015.

Publishing Agreement

It is the policy of the University to encourage the distribution of all theses, dissertations, and manuscripts. Copies of all UCSF theses, dissertations, and manuscripts will be routed to the library via the Graduate Division. The library will make all theses, dissertations, and manuscripts accessible to the public and will preserve these to the best of their abilities, in perpetuity.

Please sign the following statement:

I hereby grant permission to the Graduate Division of the University of California, San Francisco to release copies of my thesis, dissertation, or manuscript to the Campus Library to provide access and preservation, in whole or in part, in perpetuity.

Shuyu Tang
Author Signature

_09/04/2019_
Date

93